

2017

Optimized Endpoint Delivery Via Unmanned Aerial Vehicles

Fuad Gazal

Minnesota State University, Mankato

Follow this and additional works at: <http://cornerstone.lib.mnsu.edu/etds>

 Part of the [Electro-Mechanical Systems Commons](#), [Other Electrical and Computer Engineering Commons](#), and the [Other Engineering Commons](#)

Recommended Citation

Gazal, Fuad, "Optimized Endpoint Delivery Via Unmanned Aerial Vehicles" (2017). *All Theses, Dissertations, and Other Capstone Projects*. 710.

<http://cornerstone.lib.mnsu.edu/etds/710>

This Thesis is brought to you for free and open access by the Theses, Dissertations, and Other Capstone Projects at Cornerstone: A Collection of Scholarly and Creative Works for Minnesota State University, Mankato. It has been accepted for inclusion in All Theses, Dissertations, and Other Capstone Projects by an authorized administrator of Cornerstone: A Collection of Scholarly and Creative Works for Minnesota State University, Mankato.

MINNESOTA STATE UNIVERSITY MANKATO
COLLEGE OF SCIENCE ENGINEERING AND TECHNOLOGY

**OPTMIZED ENDPOINT DELIVERY VIA
UNMANNED AERIAL VEHICLES**

A Thesis Presented

by

FUAD GAZAL

Submitted to the Graduate School of
Minnesota State University Mankato in partial fulfillment
of the requirements for the degree of
MASTER OF SCIENCE IN ELECTRICAL AND COMPUTER ENGINEERING

December 2016

Department of Electrical and Computer Engineering

© 2016 Copyright by Fuad Gazal
All Rights Reserved

OPTMIZED ENDPOINT DELIVERY VIA UNMANNED AERIAL VEHICLES

A Thesis Presented

by

FUAD GAZAL

Approved as to style and content by:

Vincent Winstead, PhD

Advisor

Han-Way Huang, PhD

Professor & Graduate Coordinator of Electrical and Computer Engineering and Technology

Nannan He, PhD

Assistant Professor of Electrical and Computer Engineering and Technology

DEDICATION

I dedicate this thesis to my family, especially Emmanuel and Cynthia. Without their unwavering support, resolute patience, and steadfast enthusiasm, the completion of this work would not have been possible.

ACKNOWLEDGMENTS

Prof. Winstead, despite my many deficiencies as a scholar, from inception you have always been willing to give me a chance to prove and improve myself. Thank you so much for your support as a course lecturer, academic advisor, and on this work. I would like to express my gratitude to Prof. Nannan and Prof. Huang for their time and for accepting to be on my thesis committee. I am also grateful for Prof. Wu and Prof Zhang for their support and encouragement at various times throughout this work.

Support from friends and colleagues at Itron Inc. in Waseca also played an important role in the success of this work. I would like to thank the entire CAD team for properly introducing me to the exciting world of 3D printing. A particular circuit conundrum once caused me a great amount of frustration. Written on a napkin over dinner with friends, Ryan Jenson kindly solved the puzzling circuit. Ryan, I thank you for your genius. Mr. Adam Moyer, thank you so much for guiding me through the details of PLC control via LabVIEW HMI. Mathew Lynch, thanks for your persistent enthusiasm and encouraging suggestions.

Last but not least, to my friends, sister, mother and father I am forever grateful.

-Fuad (Aki) Gazal

OPTMIZED ENDPOINT DELIVERY VIA UNMANNED AERIAL VEHICLES

December 2016

FUAD GAZAL

B.S. E.E., MINNESOTA STATE UNIVERSITY MANKATO

M.S. E., MINNESOTA STATE UNIVERSITY MANKATO

Advisor: Professor Vincent Winstead

ABSTRACT

Unmanned Aerial Vehicles (UAVs) are remotely piloted aircraft with a range of varying applications. Though early adoption of UAVs focused on military applications, surveillance, photography, and agricultural applications are presently on the rise. This work aims to ascertain how UAVs may be employed to elicit decreased transportation times, increased power efficiency, and improved safety. Resulting in optimized end point delivery. A combination of tools and techniques, involving a mathematical model, UAV simulations, redundant control systems, and custom designed electrical and mechanical components were used towards reaching the goal of a 10-kilogram maximum payload delivered 10 miles under 30 minutes. Two UAV prototypes were developed, the second of which (V2) showed promising results. Velocities achieved in V2, in combination with a versatile payload connector and proper networking, allowed for 5-10 mile deliveries of goods less than 8-kilograms to be achieved within a metropolis faster than the 30-minute benchmark.

Keywords: Unmanned Aerial Vehicle (UAV), Supply Chain, Power Efficiency, Proportional Integral Derivative (PID),

TABLE OF CONTENTS

ACKNOWLEDGMENTS	iv
ABSTRACT.....	v
LIST OF TABLES & FIGURES	viii
CHAPTER 1: INTRODUCTION	1
1.1 Need for optimized endpoint delivery.....	1
1.2 Industries possibly disrupted by UAVs.....	4
1.3 Parcel Delivery	5
1.4 Barriers, Challenges and Risks.....	8
1.5 Objective	8
1.6 Document Organization	9
CHAPTER 2: BACKGROUND	10
2.1 Early Pioneers	10
2.2 Modern Research.....	12
2.3 Key Projects	15
CHAPTER 3: MATHEMATICAL MODEL.....	17
3.1 Generalizations and assumptions	17
3.3 Advanced Kinematic Relations.....	18
3.4 Rotor Forces and Moments	19
3.5 Dynamic Equations	20
3.6 Ground Effect.....	20
3.7 Simplified Mathematical Model.....	21
CHAPTER 4: MATLAB-SIMULINK CONTROL MODELING & SIMULATION	28
4.1 PID Controller Theory	28
4.2 Tuning PID.....	29
4.3 Simulink Control Model.....	31
4.4 Simulink Simulation.....	32
4.5 Conclusion.....	37
CHAPTER 5: SYSTEM PROTOTYPE IMPLIMENTATION.....	38
5.1 Simulink Modeling.....	38
5.2 Version 1	41
5.3 Version 2	62

5.4 Payload Deposit and Acquisition	71
5.5 Docking Station.....	73
CHAPTER 6: CHALLENGES, RESULTS, AND ANALYSIS	75
6.1 Key Challenges	75
6.2 Version 1 Results and Analysis.....	78
6.3 Version 2 Results and Analysis.....	80
CHAPTER 7: CONCLUSION	86
7.1 Conclusion.....	86
7.2 Future Work	86
CHAPTER 8: BIBLIOGRAPHY	87
CHAPTER 9: APPENDICES.....	94

LIST OF TABLES & FIGURES

Figure 1.1: Actual and hypothetical energy consumption in IEA-18 [1]	1
Figure 1.2: Freight TFC in IEA-18 decomposed by factor, 2002-12 [1].....	2
Figure 1.3: Energy intensity of freight transport (MJ/tkm), 2002 and 2012 [1].....	2
Figure 1.4: Technological Innovations leading up to present day UAVs [3]	3
Figure 1.5: Current players within delivery UAV market	6
Figure 1.6: Various commercial and private UAVs	7
Figure 2.1: Zahm’s VTOL design & Tesla’s preceding VTOL Design	10
Figure 2.2: Early Quadrotor Designs [20]	11
Table 2.1: UAV Research Projects [20]	12
Figure 2.3: Virginia Tech’s IARC team simulation via Autodesk Inventor and prototype [52].	16
Figure 2.4: Equivalent motor assumption.....	17
Figure 3.1: Earth fixed and body fixed reference frames used throughout our model [51]	18
Figure 3.2: forces and moments acting on a rotor [62].....	19
Figure 3.3: Moment calculation 1	22
Figure 3.4: Moment calculation 2.....	22
Figure 3.0.5: Moment calculation 3.....	23
Figure 3.0.6: Moment calculation 5.....	23
Figure 4.1: General PID Control Structure	28
Table 4.1: The effects of increasing each of the controller parameters	29
Figure 4.2: Example of typical response to a unit step input of a system.....	29
Figure 4.3: Different performances for different parameters in response to the same impulse [66]	30
Figure 4.4: Example Elevation PID controller	31
Figure 4.5: Complete Attitude Controller.....	32
Figure 4.6: Quad UAV execution of Roll, Pitch, Yaw and Hover [69].....	33
Figure 4.7: Control mixing of correction commands to UAV motors.....	34
Figure 4.8: Simulation position controller block	34
Figure 4.9: Path command error signal generation.....	35
Figure 4.10: PD Control setup for Theta and Phi command control	35
Figure 4.11: Complete simulation setup	36
Table 4.2: Example Moment of Inertia Data	36
Table 4.3: Example Test Data.....	36
Table 5.1: Simulation Input Data.....	38
Figure 5.1: Simulation attitude and position 3D views.....	39
Figure 5.2: Top and side views of simulated flight path.....	39
Figure 5.3: Motor simulation results from Table 5.1 simulation.....	40
Figure 5.4: UAV kinematic simulation results for PQR (X,Y,Z).....	40
Figure 5.5: Turnigy G60 motor testing apparatus.....	41
Figure 5.6: Post combustion initial motor testing.....	42
Figure 5.7: On the left: Turnigy G60 Motor On the Right: T-Motor 5008 340KV	43
Figure 5.8: Tarot 5008KV motor test data as provided by the manufacturer	44
Figure 5.9: T-Motor Current vs. Static Thrust.....	44

Figure 5.10: T-Motor Static Thrust vs. Throttle %	45
Figure 5.11: T-Motor Thrust vs. RPM^2	45
Figure 5.12: Transition from one brand of ECS to another	46
Figure 5.13: Chain of Nano-Tech LiPo Batteries being charged.....	47
Figure 5.14: Discharge curves for various battery technologies [70].....	48
Figure 5.15: Turnigy Nano-Tech LiPo battery discharge tests at various discharge rates [71]....	49
Figure 5.16: Depiction of Design Method	50
Figure 5.17: KK 2.1 Flight Controller	51
Figure 5.18: Adafruit Inc. GPS Breakout Board.....	51
Figure 5.19: Digit International XBee-Pro 2.4GHz modules	52
Figure 5.20: Texas Instruments Stellaris Launchpad.....	53
Figure 5.21: Visualization of UAV ownership protocol.....	54
Figure 5.22: Texas Instruments Boost XL SensHub for Stellaris Launchpad.....	55
Figure 6.23: Motherboard Circuit design via National instruments Multisim & Ultiboard Suits	55
Figure 5.24: V1, fully populated Motherboard.....	56
Figure 5.25: Typical 5 Channel UAV Transmitter	57
Figure 5.26: Thrustmaster Flight Hotas X Joystick	58
Figure 5.27: Ground Station settings page.....	59
Figure 5.28: Ground Station Diagnostics and Control Page.....	59
Figure 5.29: UAV Prototype V1	60
Figure 5.30: Cross sectional side and top views of UAV prototype V1	60
Figure 5.31: Stratasys® Dimensions 1200es (left) and Fortus 250mc (Right).....	61
Figure 5.32: Left: Freshly printed part Right: Heated chemical bath to remove soluble support structures	61
Figure 5.33: UAV Porotype V1 in the field and on display	62
Figure 5.34: ArduPilotMega 2.8 Flight Controller [68]	63
Figure 5.35: Left: XBee PRO 900HP S3B RPSMA 250mW, Right: 3DR’s RFD 900+MHz 1MW Ultra Long Range Radio.....	64
Figure 5.36: ESC’s used in V2	64
Figure 5.37: Texas instruments DK-TM4C123G	65
Figure 5.38: Tarot X4 Frame	67
Figure 5.39: Left: plastic Tarot motor mounts Right: Generic aluminum motor mount	67
Figure 5.40: V2 modules separated by function	68
Figure 5.41: Power Hub Simulation (left) and photograph (right)	69
Figure 5.42: Electronics Hub Simulation (left) and photograph (right)	69
Figure 5.43: Interior of Electronics Hub Simulation (left) and photograph (right)	70
Figure 5.44: UAV Prototype V2 in lab.....	70
Figure 5.45: General setup for conducting test flights.....	71
Figure 5.46: V1 payload connectors 3D model	71
Figure 5.47: V2 Payload connector 3D Model	72
Figure 5.48: 3D model of V2 payload connector within the Payload Hub.....	72
Figure 5.49: Images of the field testing payload compartment connection scheme	73
Figure 5.50: Docking Station 3D Model.....	73

Figure 5.51: Assisted landing concept simulation	74
Figure 6.1: Congested cavity for V2.....	75
Figure 6.2: Attempt at generating a high current manual switch.....	75
Figure 6.3: Creo 2.0 Simulation showing dynamic displacement (in mm) attributable to load created by motor force on the first version. Maximum displacement was 0.97844 mm	76
Figure 6.4: MCU powering circuitry	78
Figure 6.5: V1 Test flight 1.....	79
Figure 6.6: Sequential images of test flight 2	79
Figure 6.7: Sequential images of test flight 3	79
Figure 6.8: Testing ground and flight path of V2	80
Figure 6.9: V2 first flight, throttle vs. time.....	81
Figure 6.10: V2 Second flight, throttle & ground velocity vs time	82
Figure 6.11: V2 Flyaway flight path.....	82
Figure 6.12: V2 Graph of maximum achieved velocity	83
Figure 6.13: V2 Flight 6 Altitude and Climb vs Time.....	83
Figure 6.14: V2 battery consumption data.....	84
Figure 6.15: V2 Magnet interference during flyaway	85
Figure 6.16: V2 Flyaway, distance from ground station & RSSI vs time	85

CHAPTER 1: INTRODUCTION

1.1 Need for optimized endpoint delivery

The word “need” is too often employed when the word “want” would be more appropriate, as the latter is simply a desire while the former implies necessity. Indeed, with such convenient options as next day delivery readily available to many living in developed nations, at first glance the need to further optimize endpoint delivery beyond present day technology appears easily dismissible. However, energy efficiency improvements since 1990 drove savings of 2,200 terawatt hours (TWh) in 2014 among International Energy Agency (IEA) member countries, equaling about 24% of total electricity demand [1]. In our global search for innovative ways to increase and improve both clean power generation and low power design solutions, the world grows ever more energy conscience. With this in mind, the necessity to optimize how efficiently we transport everyday goods is now certainly unquestionable.

Further evidence for the global push towards greater energy efficiency can be observed from Figure 1.1, which approximately depicts the clear difference between actual total energy consumption (TFC) measured in millions of tons of oil equivalent (Mtoe), against hypothetical levels of energy usage without global IEA efforts towards efficiency. TFC depicted in Figure 1.1 is impacted by several performance improving sectors including: residential space [heating/water/lighting], appliances and consumer electronics, passenger transport, freight transport, and improvements within industrial manufacturing. The passenger and freight transport sectors relate most directly with our subject matter. The energy intensity of a passenger kilometer (pkm), i.e. the energy used to move one passenger a distance of one kilometer, has improved globally, but most notably in countries like the United Kingdom, Japan, and Italy, where rail and bus transportation have been heavily promoted. Similarly, Figure 1.2 depicts the positive impact of many nations replacing cars with more efficient rail and bus transportation for freight delivery.

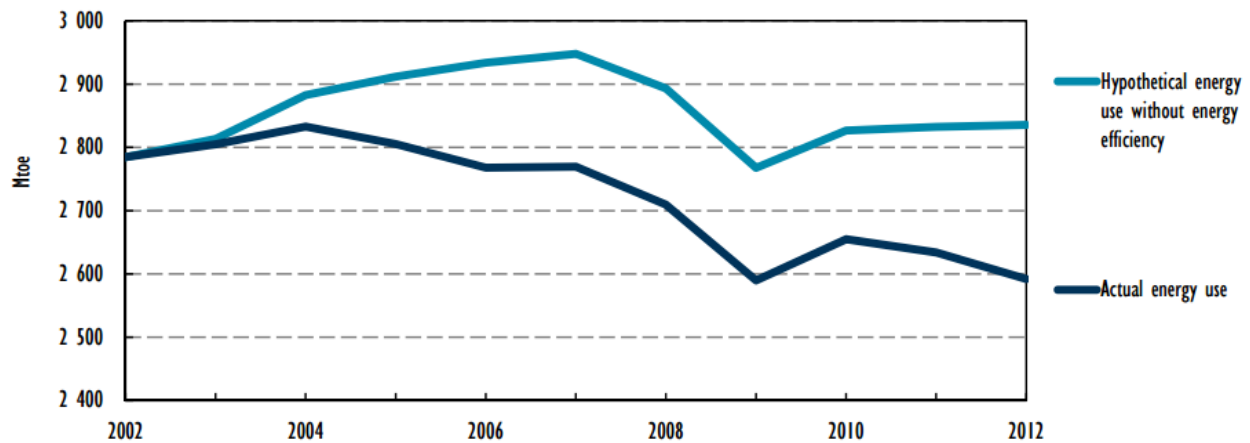
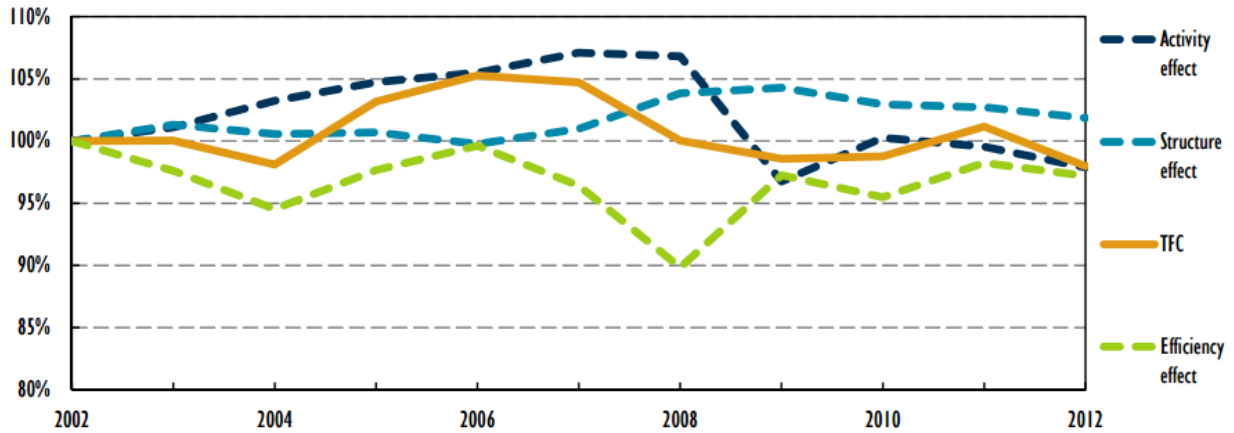


Figure 1.1: Actual and hypothetical energy consumption in IEA-18 [1]



Notes: Values are indexed to 2002 levels. Decomposition results are multiplicative rather than additive.

Figure 1.2: Freight TFC in IEA-18 decomposed by factor, 2002-12 [1]

Greece’s 2007 financial meltdown had ripple effects worldwide and was caused by numerous factors. One of which was Greece’s energy intensity, defined as units of energy consumed per units of GDP (MJ/tkm), which serves to indicate the cost of converting energy into GDP (The lower the better). The apparent inevitability of Greece’s infamous 2007 economic downturn is further bolstered by evidence in figure 1.3 showing a sharp increase in Greece’s energy intensity from 2002-2012. Nations have learned from this historic lesson, avoiding mimicking the Greek calamity and advancing their efforts to decrease energy intensity by optimizing efficiency in all sectors, including endpoint delivery.

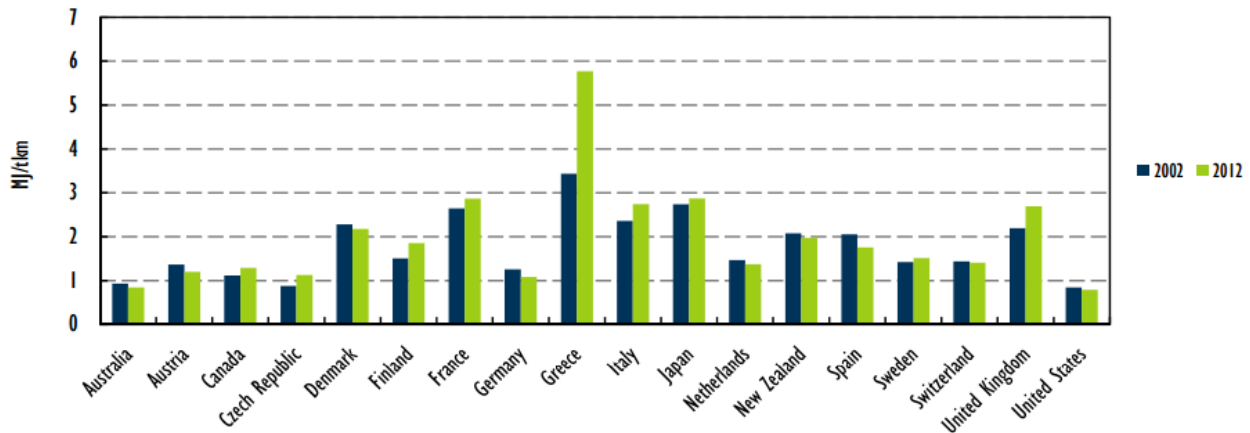


Figure 1.3: Energy intensity of freight transport (MJ/tkm), 2002 and 2012 [1]

1.1 Why Unmanned Aerial Vehicles (UAVs)

The future ubiquity of drones in our skies becomes less of a prophesy and more a fact of life by each passing day. The industry of supply chain management may yet to have been disrupted by such technology, however, within this field new technology is continually being adopted. These innovations serve as catalysts which support the process of improving supply chain efficiency [2]. Perhaps nowhere is this truer than in the case of unmanned aerial vehicles. The

majority of the public may envision something akin to the GA MQ-1 Predator whenever they think of UAVs, however technological innovations from the early 1900's up to present times has brought us a wide array of drones, with different topologies and characteristics. The timeline in figure 1.4 indicates a strong military interest in the design, development and use of UAVs. Indeed, for most of history, UAVs have been employed for military exercise. Yet the brand of commercial drones which threaten the disruption of multiple markets are not the heavy duty, combat ready, high speed, lethal weapons of war many envision, but instead are light weight (<10kg) [3], move at automobile speeds and carry no artillery.

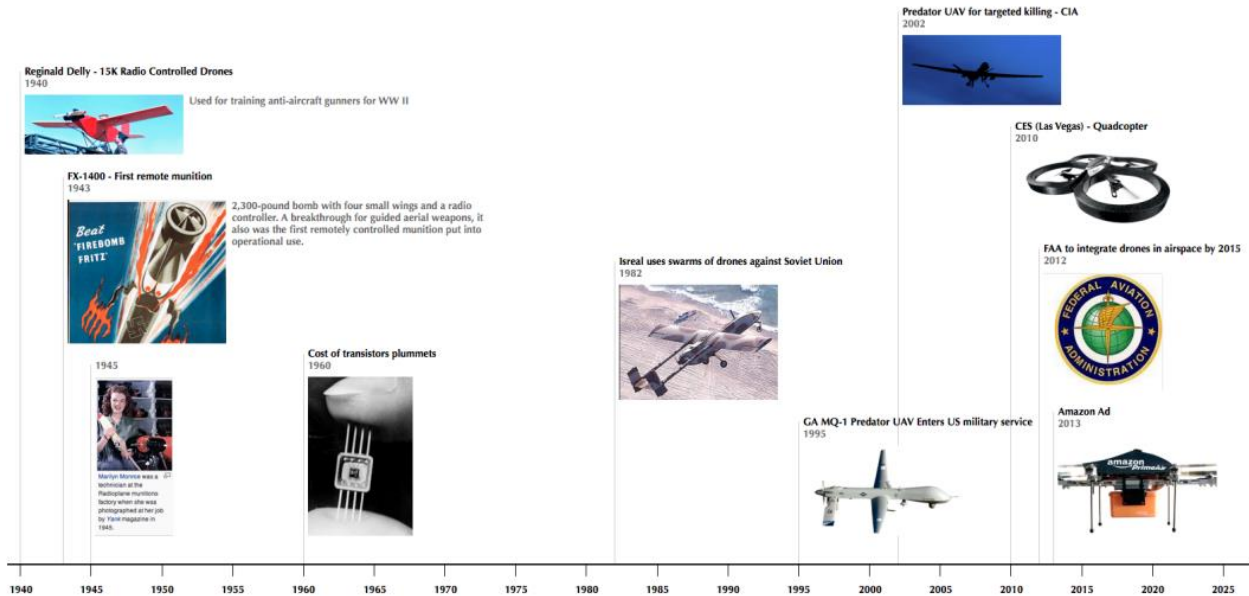


Figure 1.4: Technological Innovations leading up to present day UAVs [3]

When attempting to piece together which characteristics of UAVs permit them to benefit such a wide range of fields, we note 4 key characteristics which, when combined, stand out uniquely from other technologies: A renewable power supply, autonomous performance, agility, and payload options.

First, the vast majority of non-military UAVs are driven via high power density rechargeable lithium polymer (LiPo) batteries. This feature alone accounts for much of the gains in efficiency reaped by various industries. LiPo batteries with specific energies ranging as high as 0.95 MJ/kg, a fifth the specific energy of dynamite, are also only improving with time. Researchers are continually testing different substances, such as graphite oxide, to use as electrodes and electrolytes in an effort to create more robust and energy dense devices for storage of electrical potential energy [4]. Advancements in this field have a multiplying beneficial impact on UAVs as much of their functionality is tied to clean power.

Secondly, when artificial intelligence (AI) is used on popular websites such as Google, Facebook, and YouTube to help users streamline their online queries, find lost friends or recommend a video they might like, a certain degree of convenience is positively achieved. When that same AI extends out of the virtual realm into autonomous UAVs acting within the

physical realm, that convenience is multiplied tenfold. Furthermore, advanced UAVs today do not often use recommender system AI like the aforementioned websites, but instead employ arguably more advanced unsupervised learning and reinforcement learning AIs [5]. In essence, UAVs with their armada of selectable tools for sensory feedback, superior to simple user recommendation style feedback, approach human-like awareness in some regards and surpass human sensory capability in other particular cases (i.e. location positioning, speed, vision).

Next, the agility in motion and distance UAVs can travel are advantageous characteristics. In a July 2013 famous presentation at TEDGlobal, Raffaello D'Andrea demonstrated his fleet of UAVs (quadcopters) that he stated "Think like athletes, solving physical problems with algorithms that help them learn" [6]. D'Andrea employed a self-designed indoor positioning system in accordance with the internal sensors within each of his four UAVs to conduct impressive feats. Working both individually and collectively, D'Andrea's quadcopters were able to: balance water, throw and catch objects, simulate gravity on distance planets, assemble in varying flight formations, fly in predefined geometric and non-geometric formations, observe and follow cues from select objects, accommodate their flight algorithm to adjust for a broken/dysfunctional arm, and so much more. UAVs may yet to have reached the level of AI self-consciousness of George Lucas's C-3PO and R2-D2 astromech droids, but most would agree that today's UAVs have certainly caught up in terms of technical capability.

It's worth noting that R2-D2 never carried much more than a Lightsaber™. Bringing us to our final important UAV characteristic, a vast range of payload options. This characteristic is doubly advantageous in respect to both what UAVs may carry as part of their design and how much (kg) of a payload they can deliver. The most obvious payload employed by hobbyist abound are digital cameras. Hobbyists represent the early adopters of this technology, and as the technology matures this market will see further growth but is expected to be outpaced by other upcoming applications discussed later [3]. Aside from cameras, UAVs may easily sport a wide range of sensors including, sonar, IR, thermal and others. U.K. based Aerial Power Ltd. is already attaching wipers and cleaning solution onto UAVs in order to cut down maintenance cost of cleaning solar panels on large solar farms by 70%, whilst simultaneously increasing energy yield by 30% per month [7]. With ever increasing max payloads (10-20kg) [3] the possibilities are truly endless. When the previously mentioned characteristics are paired with the notion that UAVs can be adjusted for both indoor and outdoor use, and can indeed fly long distances at roughly 30-60 mph top speeds, we finally begin to grasp an understanding of the truly innovative technology now at our disposal.

1.2 Industries possibly disrupted by UAVs

As previously stated, the range of applications for UAVs is limited only by our collective imaginations, yet there are some sectors for which progress looks vividly bright and just beyond the horizon. The reader should keep in mind that a common theme within each of these sectors is that the UAVs are still being utilized at a fraction of their potential. Additionally, some sectors are newly emergent because prior to the rise of UAV technology they simply were not possible. These new junctions highlighted in [3] are sure to bring about new winners and losers as

individuals and businesses alike adapt to novel dynamic realities brought about by UAV technology.

- Entertainment, Media and Mapping – Likely no industry has been given more exemptions by the Federal Aviation Administration (FAA) than Hollywood. Drone mounted cameras are used from the professional level down to the personal level. For millennials, taking selfies has never been so easy. Real estate companies are benefiting not only from improved mapping quality provided by UAVs but have also discovered how much home buyers appreciate an aerial view of properties they are interested in. It's becoming increasingly common for property listings to be accompanied by a UAV tour [8].
- Service Sector – Companies such as EasyJet and Bristol Robotics Lab are partnering to bring to market UAVs intended to perform manual service inspections on bridges and other infrastructures, including aircraft. Sporting sensors far more capable than the human eyes, ears, or nose, and needing no sleep, these devices might pave new avenues for achieving unprecedented levels of civil monitoring.
- Networking for remote areas – Both Facebook, with “Internet.org”, and Google’s “Project Loon” strive to make internet access a global element of life. Solar powered high altitude UAVs designed by Titan Aerospace, are sought to aid in this goal.
- Disaster Management - Natural disasters such as the tsunami’s earthquakes and hurricanes leave mass destruction and panic in their wake. UAVs can provide a safe means of reaching dangerous zones to either visually scan areas or provide individuals with items and support.
- Law Enforcement – UAVs are found to be just as useful in domestic affairs as they are in foreign ones. Although typically armed with far less lethal or no artillery, law enforcement agencies across the united states have found this technology useful in dealing with hostage situations and surveillance. Over 40 law enforcement agencies have received authorization certificates from the FAA as of fall 2016.
- Agriculture Monitoring & Treatment – Instead of spraying pesticide on an entire farm, UAVs can be fitted with robotics, sensors and algorithms which allow them to identify regions that require weeding and apply the pesticide at that location. Apart from crop health, UAVs can monitor harvests, livestock, irrigation and much more within a farm.
- Oil & Gas – Similar to farms, monitoring of pipelines can be efficiently streamlined. Many of the labor-intensive tasks pose a high degree of danger to the laborers. This would be entirely alleviated by employing the use of UAVs working together in the same fashion as Raffaello D’Andrea has shown can be achieved.

1.3 Parcel Delivery

This work may have application to the above industries, however our focus for the remainder of this document will be on the industry of delivery UAVs, and for good reason. Radiant Insights predicts the “Commercial drones (UAVs) market to reach \$4.8 Billion from 2015 to 2021” [9], with a significant bulk coming from parcel delivery UAV sales. This will result from a transition

mirroring the switch from automotive transport of freights to rail and bus. By virtue of a similar switch from delivery trucks to UAVs, parcel delivery might turnout as the largest benefactor of decreased energy intensity via UAV technology. With a simple 5 lbs. (2.27kg) payload capable UAV, items such as clothing, merchandise, nourishing food, lifesaving medicine and everything in-between can be affordably transported across varying distances. Figure 1.5 [10] shows how a few drone startups are teaming up with large logistics companies and even larger retailers to make the dream of UAV endpoint (home) delivery a reality.



Figure 1.5: Current players within delivery UAV market

The dogma and general strategies for implementation of UAV delivery differ amongst the retailers (Amazon, Google, Walmart, and Pizza Hut) greatly in terms of target customer scope, however in terms of system design they appear somewhat identical. The general strategy of these players, to be later expanded on, is very important to this work as it provides a platform for comparing and contrasting differing novel systems and strategies.

The first and clearly the most ubiquitous generalizable retailer system element lies in their collective projected cost savings. Aside from the electronic benefits previously mentioned by employing renewable power via LiPo batteries, there exist additional cost reducing factors. Matternet co-founders Paola Santana and Andreas Raptopoulos suggest UAV delivery employed in 3rd world (underdeveloped) countries could connect billions of people who today do not have access to all-season-roads, while saving millions in public infrastructure development projects. Keep in mind that The American Road and Transportation Builders Association estimates the cost of a “new 2-lane undivided road” at \$2 million to \$5 million per mile [11], Making the construction of western-like roads a costly affair for developing debt ridden nations. Even worse, dealing with underdeveloped countries the per mileage cost quoted may prove to be a gross underestimation, as government corruption must sadly be factored in. This leaves developing a network of privatized delivery UAVs as a significantly more affordable option (~<\$1M). The projected flat out cost per delivery, 24 cents for Matternet, and 88 cents for Amazon [12] appear impossibly low. However, an Ark Invest analysis on Amazon posited that with 6,000 operators making \$50,000 in annual salary, and collectively managing 40,000 drones each delivering 30 times daily, Amazon could charge \$1 per UAV home delivery and recoup their initial investment

in less than a year [13]. This again is without factoring in any additional cost savings acquired by forgoing more expensive ground transport options.

The second set of system characteristics uniting present key players in this field are the method and scale of delivery. Amazon, Walmart, Pizza Hut and the startups they are associated with each intend on landing their UAVs atop their target customers' private property. In the case of Google's Wing, the UAV does not land but instead descends the package to earth via a cable. Whereas in all other cases the UAV itself must land on earth to release and obtain packages. For these UAVs, landing is ultimately achieved via a pattern on the ground which the UAV uses internal sensors to identify and slowly approach [14]. Despite the diversity in physical design, each UAV in Figure 1.6 below executes its objective in a relatively similar fashion to the rest, and each one is designed for a similar maximum payload of roughly 2.5kg (~5.5 lbs.).



Figure 1.6: Various commercial and private use UAVs

Walmart spokesman Dan Toporek has been quoted saying “There is a Walmart within five miles of 70% of the U.S. population, which creates some unique and interesting possibilities for serving customers with drones.” [15], leading us into our last generalized retailer system element, proximity. Similarly to Walmart, Amazon exclaims individuals who live within 7.5 miles from an Amazon warehouse can expect to “get packages in 30 minutes or less” [12]. What’s key to understand from this emphasis on proximity is that in all cases the direction of transportation is always from the retailer to the customer and never vice versa. It’s worth noting that this aspect of all the above proposed UAV delivery solutions does nothing to address customer returns (i.e. transportation from the customer to the retailer), which is assumed to be carried out via slower conventional methods (mail). Indeed, beyond the glittering promise of Jetsonian skies filled with miraculous flying machines, are several challenges suppressing

UAVs and the corporations who design them which need to be addressed before releasing this technology for public consumption.

1.4 Barriers, Challenges and Risks

Several critical social, environmental, and engineering challenges remain persistent in keeping the delivery UAV market dormant. Considering the status quo of recent efforts to make advancements in this field, these hurdles should come as no surprise.

- Privacy – Today a camera fitted quadcopter can be purchased for as low as \$100-\$200, much to the delight of hobbyist everywhere yet the bane of others. Many fear skies filled with drones carrying high resolution imaging systems would pose a significant danger to individual privacy. When media outlets report an unknown DJI Phantom series quadcopter flying outside the Whitehouse grounds, the perception of privacy and security breaches is publicly exacerbated [16].
- Safety – The risk of personal injury due to a crashed UAV is a reality. In the case of delivery UAVs, the package would certainly also be at risk of damage. The use of GPS blockers/jammers, and targeted Wi-Fi commands by hackers is a less prevalent but equally troublesome safety threat.
- Power Management – Although sufficient, present powering systems and technology for delivery UAVs leave much to be desired. As depicted earlier, present retailers have no solution for allowing customers to return packages via UAV. A large challenge in adding this feature is the lack of sufficient power for the return journey as well as systems that simply are not designed for such functionality.

Eclipsing all challenges mentioned above is the strict regulatory blockade posed by the U.S. FAA, who have dashed the hopes of corporations eager to employ UAVs for delivery. Many companies lobbied, Amazon most notably [17] led the push to relax FAA regulations since late 2015, but seemingly to no avail. Including a 55-pound maximum all up weight, 87 knots maximum speeds and 400 feet maximum altitude, the list of regulatory restrictions from the FAA latest ruling flatly pronounce the industry of UAV delivery an illegal venture within United States skies [18]. Regarding the present restriction, FAA administrator Michael Huerta stated to reporters “What we need is to ensure that it can be safely done”. He continued “If they [corporations] can demonstrate capability and safety, we would consider waiving that [restriction]” [19]. Huerta’s words accent the pivotal significance of optimizing the “capability and safety” of delivery via UAV, the theme of this work.

1.5 Objective

In this thesis, we strive to optimize delivery via UAV by finding solutions to some of the challenges persistent in the field. A design project at heart, the bulk of this work will be aimed towards the development of a UAV with optimized characteristics for delivery. In doing so we will employ a mathematical model to simulate desired outcomes. Additionally, physical UAV models will undergo test flights to compare and contrast with our simulation results. For reasons later elaborated in Chapter 5, an X8 octa quad (8 motor quadcopter)

UAV layout has been selected serving as the basis of all subsequent mathematical models, simulations and designs. Despite a heavy emphasis on UAV design, the definitive goal of this work is towards recommending an overall system level design in an effort to better meet commercial, societal and regulatory requirements. Our progress measuring metric is three-fold. First, the system should decrease delivery times below the proclaimed 30-minute benchmark of set by industry leaders. Secondly, the system should support payloads larger than 2.26 kg. Lastly, the system should employ justifiably safer delivery methods capable of customer-to-retailer return traffic.

1.6 Document Organization

Following this chapter:

- Chapter 2: Provides information on previous works
- Chapter 3: Offers a simplified mathematical model
- Chapter 4: Reviews simulation options
- Chapter 5: Documents the prototyping and simulation of system components
- Chapter 6: Reviews results from field testing
- Chapter 7: Provides conclusions and suggestions on future work
- Chapter 8: Cites all references worked

This work relies heavily on previous work for content in Chapters 3 and 4, and makes some contributes as well. In chapter 3 a comparison between mathematical models for an octa-quad and quadrotor are made, providing insight into how one may be generalized into the other and the consequences of doing so. Additionally, weaknesses of the simulations methods of chapter 4 are taken into account prior to being used in our design process. Chapters 5, 6, and 7 use the earlier chapters as a foundation but are largely novel in nature.

CHAPTER 2: BACKGROUND

2.1 Early Pioneers

The genesis of modern UAVs owes much of its success to the pioneers of the early 20th century who took on the challenge of manned flight. Following the historic first manned flights by Orville and Wilbur Wright in 1903, the first quadrotors were built by the Breguet Brothers in 1907. The flights of the Gyroplane No. 1 are considered to be the first manned flight of a helicopter, however the aircraft in these flights were tethered to the ground. A lack of stability and proper control mechanism made it such that the Gyroplane could never fly completely free. Untethered free flight would require an optimization in design.

Enter the father of modern power generation and distribution, Nikola Tesla, who initially was not fond of airplanes and once predicted that airplanes would "never fly as fast as a dirigible balloon". Ironically Tesla would later criticize airplanes for being too fast to take off and land, requiring an "indispensable high velocity, imperiling life and property." By 1908 the "helicopter" had already been proposed in theory. Tesla, calculating that a helicopter would prove "incapable of proceeding horizontally along a straight line" paradoxically took on a helicopter optimization project of his own resulting in a US Patent (1,655,113).

Tesla's vertical takeoff and landing (VTOL) design is shown in figure 2.1. His design is that of a machine that would take off with the propeller pointed upwards, like a helicopter, and then transition to horizontal winged flight, resolving his aforementioned grunts concerning high speed landing. Unfortunately, by the time Tesla conceded that airplanes might be useful, he was uncharacteristically behind the times. Four years prior, Albert Zahm, a versatile inventor with the Curtiss Aeroplane and Motor Corp., had come up with essentially the same idea. With the only distinguishable difference being a hinged seat allowing the pilot to always sit normal to the ground in Tesla's design, a considerably minor innovation.

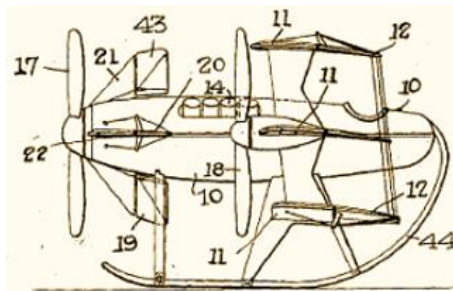
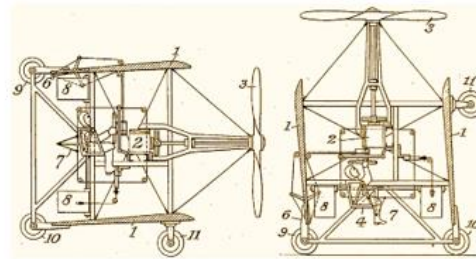


Figure 2.1: Zahm's VTOL design

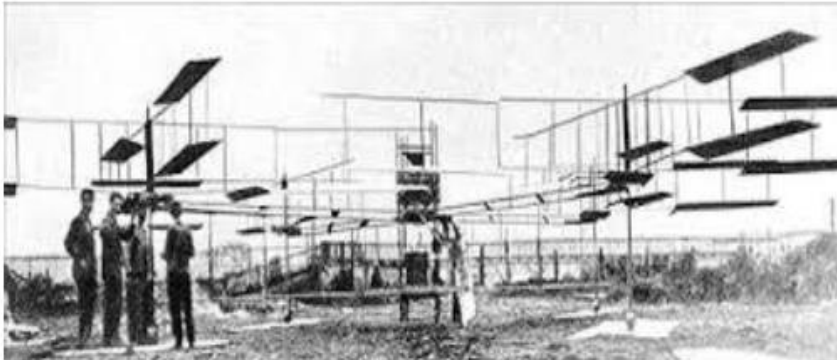


Tesla's preceding VTOL Design

Following Gyroplane No. 1, other attempts were made on manned quadrotors, such as Georges de Bothezat's Flying Octopus in 1922, and Etienne Oemichen's Oemichen No.2 that same year. Later, designs such as Convert Wings Model A in 1922 by Oemichen and de Bothezat, the Curtiss X-19 in 1963 by Curtiss-Wright corporation, the Bell X-22A in 1966 by Bell Aircraft corporation, and the Fly Vehicles of the Moller company [30] pushed the envelope even further (Figure 2.2).

Convert Wings Model A effectively revived concepts attempted in 1922 by Oemichen and de Bothezat, only with more modern technology. A first prototype flew in 1956. Despite successful testing and development, military support for the quadrotor ceased after cutbacks in defense

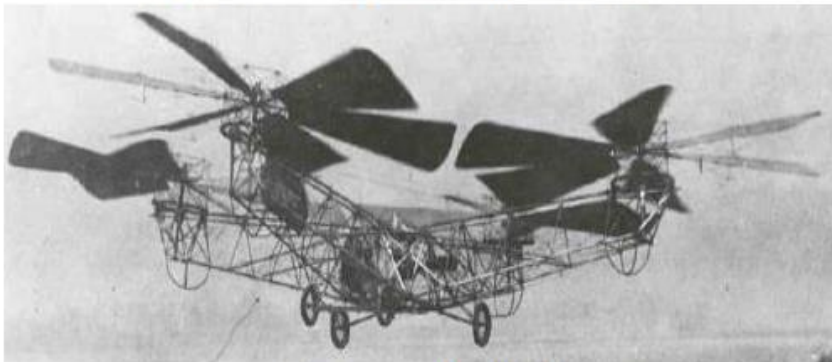
spending. However, the design, particularly its control system, was a precursor of current UAVs and experimental vertical-rising aircraft designs that incorporate tandem wings or a square configuration of four fans, ducts, or jets.



Bréguet Richet Gyroplane No. 1



Oehmichen No.2



Georges de Bothezat








Curtiss-Wright










Figure 2.2: Early Quadrotor Designs [20]











2.2 Modern Research

The early pioneers laid the foundation for the rise of modern UAVs, however removing the “manned” and ” piloted” portion would not occur for several more decades. Continued advancements in this field would be closely tied to advancements in modern control systems and the microprocessors which powered them. After initially manned attempts, advancements in the knowledge of control theory and technology allowed the development of unmanned quadrotors. Following those improvements, several research laboratories, universities and private enterprises began projects involving quadrotors. Though the development of full autonomous flight in varying environmental conditions and tasks is still a challenge today, Table 2.1 shows how far the technology has come.

Table 2.1: UAV Research Projects [20]

	University/ Organization/	Project	Year	Early studies	Recent studies
	Dragan flyer	V Ti [21]	1998	Commercial product	Commercial product
	Stanford	Mesicopter-I., Kroo [22]	2000-2012	-Feasibility and capability of the vehicle -Design and Manufacturing Techniques [22]	Control of Multiple UAVs for Persistent Surveillance [23]
	ANU	P. Pounds's thesis [24]	2002-2014	Dynamic modelling based on Newton-Euler Method Control attempt [24]	-Triangular Quadrotor [25] - Output tracking for quadrotor-based aerial manipulators [26]
	FEIT, ANU	X-4 Flyer, P., Pounds [24]			
	Uni. Pennsylvania	E. Altug [27]	2002-2012	Yaw and height control using Visual feedback control techniques [27]	-Improving disturbance rejection and robustness of the vehicle using Fuzzy logic controller [28] -Obstacle avoidance using Catadioptric cameras [29]
					Precise measurement and prediction of position and orientation of the vehicle in the presence of external

	Uni. Compiègne	P. Castillo's thesis, A. Dzul [30]	2003- 015	-Dynamic modelling using Lagrange approach -Linear trajectory tracking [30]	perturbation (out- door control of the quadrotor) [30], [31] -Quaternion control scheme [32] -Velocity regulation of the quadrotor [33]
	Uni. Aalborg	X 3D [34]	2004	---	---
	Stanford	Starmac I [35]	2004-2011	Altitude and attitudes control in presence of wind [35]	Collision avoidance and control of the vehicle in aggressive maneuver utilizing combination of hybrid decomposition and reachable set theory [36]
	Stanford	Starmac II [35]			
	EPFL	Bouabdallah & Siegwart [37]	2004-2011	Autonomous control of the vehicle in indoor environment [37]	Robust control of quadrotor in presence of model uncertainties and external disturbances [38]
	Cornell University	Eryk Brian Nice's thesis and R. D'Andrea, [39]	2004-2015	Nonlinear dynamic modelling and hover control [39]	-Iterative learning controller for improving the performance of the vehicle in highly dynamic open-loop maneuver [40]
	Middle East Technical University, Turkey	F.B. Çamlica's thesis, C Özgen [41]	2004-2014	Hover control [41]	Trajectory tracking in presence of disturbance [39]
	Technology university of Malaysia	Weng and Shukri [42]	2006	---	---
	Uni. Oldenburg	M. Kemper's thesis [43]	2006-2009	Robust control of quadrotor respect to variable center of gravities [43]	Way point navigation and trajectory optimization [44], [45]
--	Cranfield university	I.D. Cowling and J.F. Whidborne	2007-2010	Optimal trajectory generation around obstacle [46]	Trajectory generation and tracking in presence of gust and control of the vehicle in chimney mission [47]

	MIT	P. Tournier and J.P. How [48]	2007-2015	Autonomous control of quadrotor by using visual servo-ing method [48]	Maneuver learning from demonstration (communication with human) [49] -Control of variable-pitch quadrotor [50]
	Uni. TUDelft	Menno Wierema and Ir. C. de Wagter [51]	2007	Autonomous indoor navigation	----
	IARC Team - Virginia Tech. Uni.	IARC Team Quadrotor [52]	2009	Autonomous mission execution	-----
	Univ. Maryland	AVL's Micro Quad (J. Sean Humbert) [53]	2009-2015	Robust visual navigation [53]	Robust stabilization and command tracking behavior in obstacle-laden environments [54]
	Azad University of Ghazvin	Farshid Jafari Harandi [55]	2010	Outdoor navigation	-----
	CrazyFlie	CrazyFlie [56]	2011	Commercial product	Commercial product
	Commercial product	Ascending Technologies Hummingbird [65]	-----	Commercial product	Commercial product
	Silverlit	X-UFO [57]	-----	Commercial product	Commercial product
	microDrones GmbH	MD4-200® [58]	-----	Commercial product	Commercial product
	DJI	Phantom Series	2013-2016	Commercial product	Commercial product

2.3 Key Projects

At Stanford University, the Mesicopter project was conducted between 1999 and 2001 [22], and focused on the feasibility of a centimeter scaled quadrotor to use in massive quantities to investigate large areas or possibly even distant planets. The aerodynamics effects of quadrotors were studied extensively. Eventually, the Stanford Testbed of Autonomous Rotorcraft for Multi-Agent Control (STARMAC) became a multi-vehicle test bench used to demonstrate new concepts in multi agent control on a real-world platform. STARMAC consisted of multiple quadrotor vehicles that autonomously tracked a given waypoint trajectory. To begin, the vehicles and test bench required a design for proof-of-concept flights. This design was completed in the fall of 2004 with the development of STARMAC I. Later STARMAC II would require a complete vehicle and testbed redesign to create a fully functioning test bench allowing for multi agent control to be demonstrated.

Interestingly, an off-the-shelf Draganflyer III acted as the base vehicle for STARMAC I. Draganflyer III had a total of 1 kg of thrust and could sustain hover for about ten minutes. STARMAC I replaced the onboard electronics with customized printed circuit boards and components so as to obtain complete control over motor commands, power supply and sensor measurements. Employing larger lithium-polymer batteries than those that came standard on the Draganflyer III also increased both payload and flight duration, enhancing the abilities of the system. The Microstrain 3DM-G motion sensor was used for attitude measurements, this module included accelerometer, magnetometer, and 3-axis gyro data which could be polled in real time. Trimble Lassen Low Power GPS receiver provided position and velocity measurement while the Devantech SRFO8 sonic detection and ranging (SONAR) module was used to optimize the resolution of low altitude data acquisition for more critical tasks like take-off and landing. Dual Microchip 40 MHz microcontrollers coordinate all of the onboard sensors. STARMAC I performed position estimation via an Extended Kalman Filter to update the position and velocity estimates at 10 Hz. Attitude stabilization is performed on board at 50 Hz. Communication for each unit was relayed to a central base station on the ground via a 150 ft. range Bluetooth class II devices. This work's final design borrows from STARMAC I's base stations differential GPS and waypoint tracking. The ground station tracks tasks for all air units, transmitting attitude values to the air units for position control. Manual flight and waypoint control is performed via the ground station laptop using LabVIEW, another testing setup style which this work builds on. Note that for STARMAC I, a Linear-Quadratic Regulator (LQR) closed loop control technique determine attitude. This method has its own strengths in correction of pitch roll and yaw, but was weak in other respects such as angle deviation and resolution. Integral sliding mode, reinforcement learning, and other control systems would be tested within STARMAC I platform as well, paving the way for comparative advantages and disadvantages to be discerned between them.

Stanford University's second generation of experimental quadrotors, STARMAC II, would see improvements in thrust capability, on-board computation resources, communication reliability bandwidth, and position measurement accuracy. More powerful brushless motors, rigid plastic propellers, an improved Atmega 128 processor, advanced digital logic ADL855 PC104, and a transition from Bluetooth to a 2.4 GHz Wi-Fi network are components of the improved second generation design. Among these upgrades, a major improvement in the

STARMAC II's design employed a Proportional-Integral-Derivative (PID) controller for altitude, attitude and position control. This controller's performance was found to be superior to the LQR, data supported by the widespread use of PID controllers in multirotors today.

At the Ecole Polytechnique Fédérale de Lausanne, Samir Bouabdallah executed an extensive PhD. quadrotor UAV project. Bouabdallah utilized a quadrotor-like test bench with off-board data processing and power supply to safely and easily test control strategies. For practical testing the Omnidirectional Stationary Flying Outstretched Robot (OS4) was designed. OS4 had all the necessary sensors for autonomous operation with a unique method of determining position using an on-board down-looking CCD camera and a simple pattern on the ground. The camera provided an image of 320x240 at up to 25 fps fed into an algorithm which detects the pattern, estimates the pose and provides the camera position and yaw angle relative to the ground. Most pertinent to this work, Bouabdallah's project tested several control theories, including Lyapunov theory for applied for attitude control, back stepping, sliding-mode concepts, PID, and LQR techniques for attitude control [37]. Bouabdallah developed dynamic models to simulate the quadrotor evolving from a simple set of equations, valid only for hovering, to a complex mathematical model with more realistic aerodynamic coefficients and sensor and actuator models.

In 2009 Virginia Tech arranged a team of mechanical and aerospace engineering students to submit an entry for the International Aerial Robotics Competition (IARC). IARC charged competitors with navigating a UAV of their own throughout an indoor competition area with specific mission objectives and restrictions broadly elaborated in [52]. In brief, the mission would include navigating the UAV through obstacles from point A to point B, collecting data once at point B, and returning it to point A where the mission began. Use of GPS, GLONASS, Galileo, or other satellite navigation systems was also strictly prohibited. Another critical rule of the competition was an all up mass limitation of 1.5 kg for all competing vehicles. This posed a challenge to Virginia Tech's IARC team's design since a critical sensor module weighing 536.1 grams assumed an overwhelming portion of their legalized mass. A solution was found in implementing lightweight yet strong carbon fiber with basswood frame in a quadrotor layout. Additionally, the team discovered benefits in placing the bulk mass right under the geometric center of the quadrotor as seen in Figure 2.3. Namely, improved flight stability along with a 360° sensor range of view were achieved. Further supporting this research, many subsequent image capture centered UAV platforms (DJI Series, Yuneec Q500) would go on to adopt layouts of this fashion.



Figure 2.3: Virginia Tech's IARC team simulation via Autodesk Inventor and prototype [52]

CHAPTER 3: MATHEMATICAL MODEL

A mathematical model of our intended quadcopter design is required in order to fully equip ourselves with the tool necessary for analysis. Menno Wierema’s 2008 study on indoor navigation control of UAVs [51] provides an excellent organization of dynamic equations on attitude and positions of a quadrotor. This summation draws heavily on researched conducted by [59], [60], [61], and others, to be reviewed in brief. Since our selected UAV design is an octa-quad and not a typical quadcopter, we begin by making some required assumptions which allow us to assimilate the proposed model for our X8 design.

3.1 Generalizations and assumptions

- The X8 structure is rigid
- The X8 structure is symmetrical
- The X8 propellers are considered rigid
- The dual coaxial counter-torqued motors on each arm of the X8’s 4 arms have additive Thrusts, mass, and torques which can be summed into an equivalent motor representation for a 4-motor quadcopter:

$$\begin{aligned}
 Mass_{Quadcopter\ Motor} &= Mass_{X8\ Motor\ 1CW} + Mass_{X8\ Motor\ 2CCW} \dots \dots \\
 Thrust_{Quadcopter\ Motor} &= Thrust_{X8\ Motor\ 1CW} + Thrust_{X8\ Motor\ 2CCW} \\
 Torque_{Quadcopter\ Motor} &= Torque_{X8\ Motor\ 1CW} - Torque_{X8\ Motor\ 2CCW}
 \end{aligned}$$

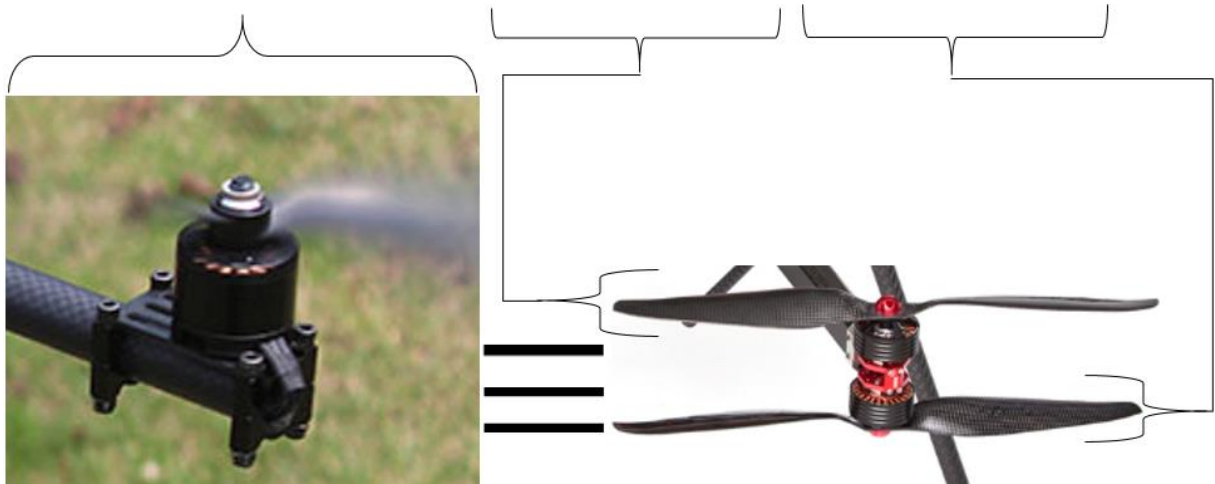


Figure 2.4: Equivalent motor assumption

3.2 Reference Frames

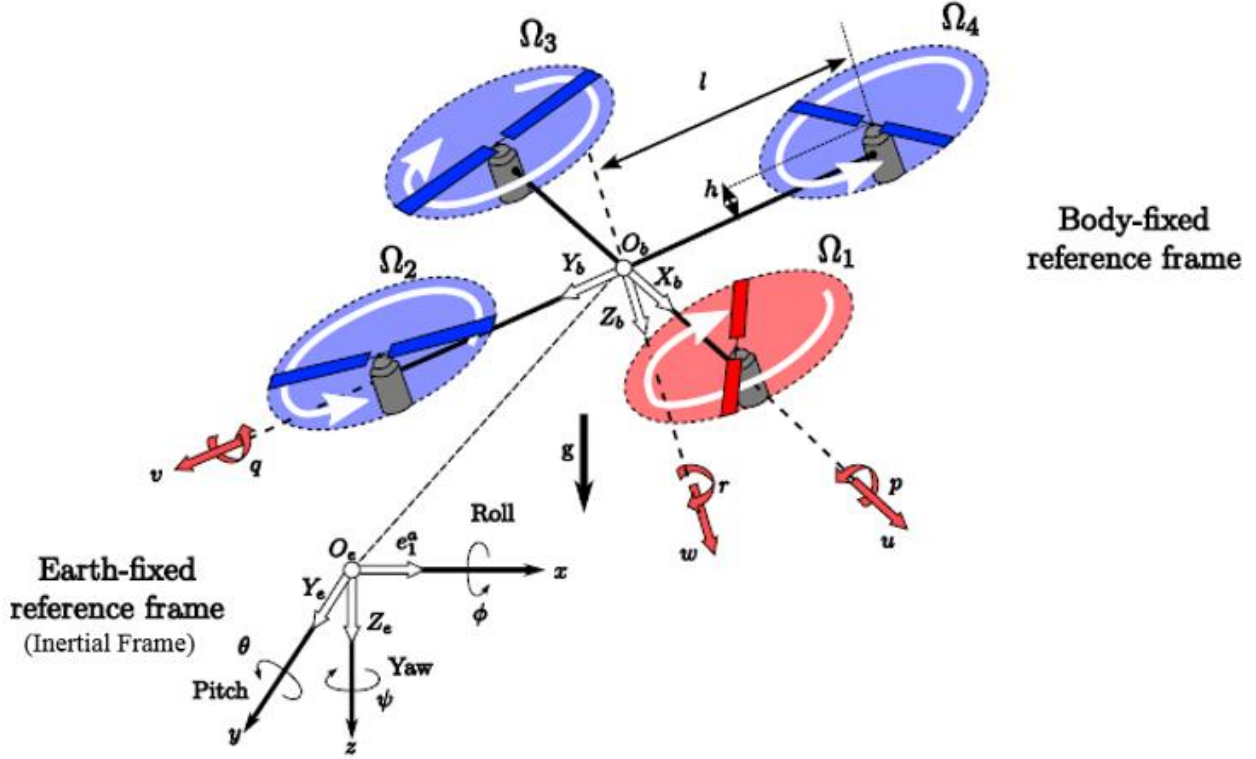


Figure 3.1: Earth fixed and body fixed reference frames used throughout our model [51]

With respect to the earth reference frame, the absolute position of the quadrotor is described by the three coordinates (x, y, z) of the center of mass.

Absolute attitude is described by the three Euler's angles (ψ, θ, ϕ) . We refer to these three angles as yaw, pitch, and roll respectively. For general stable operation, we expect the following to hold:

$$\begin{aligned} -\pi &\leq \psi < \pi \\ -\frac{\pi}{2} &< \phi < \frac{\pi}{2} \\ -\frac{\pi}{2} &< \theta < \frac{\pi}{2} \end{aligned}$$

3.3 Advanced Kinematic Relations

$$\left[\frac{d\psi}{dt}, \frac{d\theta}{dt}, \frac{d\phi}{dt} \right]^T = N(\psi, \theta, \phi)\omega$$

The derivatives of (ψ, θ, ϕ) can be expressed by the above equation which the angular velocities, $\omega = [p \ q \ r]^T$, are expressed with respect to the body frame of reference. Then, $N(\psi, \theta, \phi)$ results in a 3x3 matrix:

$$N(\psi, \theta, \phi) = \begin{bmatrix} 0 & \sin\phi \sec\theta & \cos\phi \sec\theta \\ 0 & \cos\phi & -\sin\theta \\ 1 & \sin\phi \tan\theta & \cos\phi \tan\theta \end{bmatrix}$$

Let $V = [u \ v \ w]^T$ be the absolute velocity of a quadcopter expressed in a body-fixed reference frame. The rate of change in positions (x, y, z) is then given by:

$$\left[\frac{dx}{dt}, \frac{dy}{dt}, \frac{dz}{dt} \right]^T = R(\psi, \theta, \phi)V$$

where $R(\psi, \theta, \phi)$ is the rotation matrix given by:

$$R(\psi, \theta, \phi) = \begin{bmatrix} \cos\theta \cos\psi & (\sin\theta \cos\psi - \cos\phi \sin\psi) & (\cos\phi \sin\theta \cos\psi + \sin\phi \sin\psi) \\ \cos\theta \sin\psi & (\sin\theta \sin\psi + \cos\phi \cos\psi) & (\cos\phi \sin\theta \sin\psi - \sin\phi \cos\psi) \\ -\sin\theta & \sin\phi \cos\theta & \cos\phi \cos\theta \end{bmatrix}$$

3.4 Rotor Forces and Moments

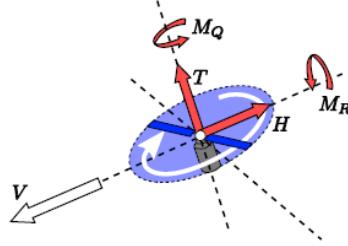


Figure 3.2: forces and moments acting on a rotor [62]

The resultant of all forces acting on all blade elements perpendicular to the rotor shaft, thrust force is represented as:

$$T = C_T \rho A (\Omega R)^2$$

The thrust coefficient C_T is directly related to the aerodynamic efficiency, indirectly shows how much the energy extraction device (the propeller) affects air flow and thrust by extension. Similarly, the hub coefficient C_H can be replaced with C_T in the equation above to yield the hub force:

$$H = C_H \rho A (\Omega R)^2$$

The resultant moment of all horizontal forces acting about the center of the rotor is the torque that determines power required from the motor to keep the rotor spinning, and is represented by

the drag moment M_Q . It's important to note that the rolling moment, M_R , which occurs in a quadcopter due to differing forces within the rotors advancing and retracting blades should be more negligible in an X8 design due to a countering rolling moment which occurs on the mirroring motor for each arm. We add it to the model for consistency.

$$M_Q = C_{M_Q} \rho A (\Omega R)^2 R$$

$$M_R = C_{M_R} \rho A (\Omega R)^2 R$$

3.5 Dynamic Equations

Using general equations of motion from [62]:

$$F_x = -W \sin \theta + X = m \left(\frac{du}{dt} + qw - rv \right)$$

$$F_y = W \cos \theta \cos \psi + Y = m \left(\frac{dv}{dt} + qu - rw \right)$$

$$F_z = W \cos \theta \sin \psi + Z = m \left(\frac{dw}{dt} + qv - ru \right)$$

Complete dynamic equations of a quadrotor accounting for all external forces in body fixed frame (Hub forces, friction, and thrust) and internal forces in body fixed frame (propeller gyro effect, pitch actuators action, hub forces due to sideward and forward flight, pitch moments, Inertial counter-torque, and counter-torque unbalance) both along each axis (u, v, w) can be written as:

$$m \frac{du}{dt} = -m(g \sin \theta - qw + rv) - \sum_1^4 H_{u_i} - \frac{1}{2} C_u A_u \rho_u |u|$$

$$m \frac{dv}{dt} = m(g \cos \theta \sin \phi - ru + pw) - \sum_1^4 H_{v_i} - \frac{1}{2} C_v A_v \rho_v |v|$$

$$m \frac{dw}{dt} = m(g \cos \theta \cos \phi - pw + qu) - \sum_1^4 T_i - \frac{1}{2} C_w A_w \rho_w |w|$$

3.6 Ground Effect

When the quadcopter is within heights about 0.5 to 1.0 times the diameter of a rotor [63] a ground effect occurs. To the time while the UAV is within this distance to ground it will experience heightened rotor efficiency due to the rotors airflow impacting with the ground and causing a buildup of air pressure below the UAV. The result is that less power is required for the UAV to maintain a constant altitude in the air when close to ground than when out of ground effect zone. Additional equations are available which would use a ground effect thrust coefficient

$C_{T_{ground}}$ to factor into our mathematical model, however, the time spent by the UAV in this zone is negligible and thus $C_{T_{ground}}$ is omitted.

3.7 Simplified Mathematical Model

The above model framework is important to review in understanding the range of variables involved in modeling a UAV. Continuing with this framework may provide precision in calculations, but accounting for every variable when attempting to simulate becomes a difficult task with diminishing marginal reward. This is further highlighted by the scope of this work, for which the UAV shall perform no flips or advanced maneuvers and requires only general “a to b” style flight simulations. For this reason, with minor parameter adjustments, Drexel University’s MEM design Team 37’s excellent open source quadcopter dynamic modeling and simulation tool will more than suffice [64]. This method of simulation via MATLAB-Simulink employs a slightly simplified mathematical model.

The following simplifying assumptions will be made in addition to those previous mentioned in section 3.1:

- The ground effect is to be neglected
- UAV center of mass is located at its geometric center, allowing for the cross product of the inertia matrix to be neglected
- Blade flapping effects are accounted for within lumped parameters
- frame aerodynamic drag is accounted for within lumped parameters

$$J^b = \begin{bmatrix} J_x & 0 & 0 \\ 0 & J_y & 0 \\ 0 & 0 & J_z \end{bmatrix}$$

Akin to the importance of the UAVs mass in describing translational motion, parameters for the UAVs rotational motion require us to mathematically describe its mass moment of inertia, J^b . However, unlike the property of mass, J^b is a kind of mass made relative to the objects center of mass and not simply attained by weighing the UAV. This requires a piecewise analysis of the UAVs design. It’s worth noting that due to our assumption of symmetry we take it that $J_y = J_x$. The approach prescribed by [64] breaks apart components of J^b in each case (J_x, J_y, J_z) into smaller additive sections. These simplified sections are to be measured and weighed, and Huygens–Steiner’s parallel axis theorem will be utilized to determine the moment of inertia contribution of each component about the x, y, and z axes of the UAV. The UAV is thus decomposed into 4 segments.

Motors:

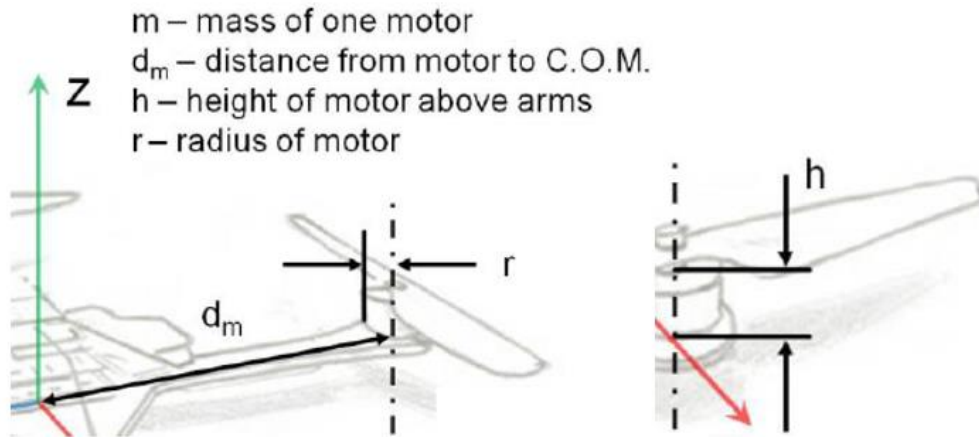


Figure 3.3: Moment calculation 1

$$J_{x,M} = J_{y,M} = 2 \left[\frac{1}{4} m r^2 + \frac{1}{3} m h^2 \right] + 2 \left[\frac{1}{4} m r^2 + \frac{1}{3} m h^2 + m d_m^2 \right]$$

$$J_{z,M} = 4 \left[\frac{1}{2} m r^2 + m d_m^2 \right]$$

Electronic Speed Controllers (ESC):

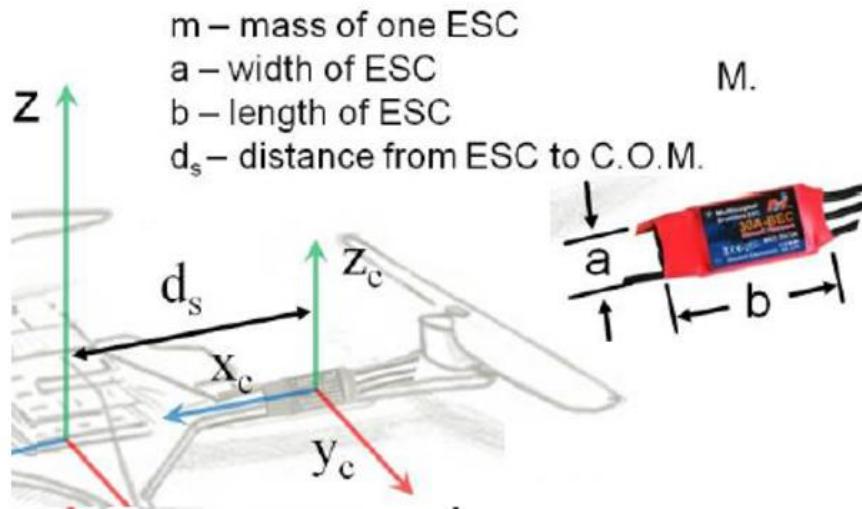


Figure 3.4 Moment calculation 2

$$J_{x,S} = J_{y,S} = 2 \left[\frac{1}{12} m a^2 \right] + 2 \left[\frac{1}{12} m b^2 + m d_s^2 \right]$$

$$J_{z,S} = 4 \left[\frac{1}{12} m (a^2 + b^2) + m d_s^2 \right]$$

Central HUB:

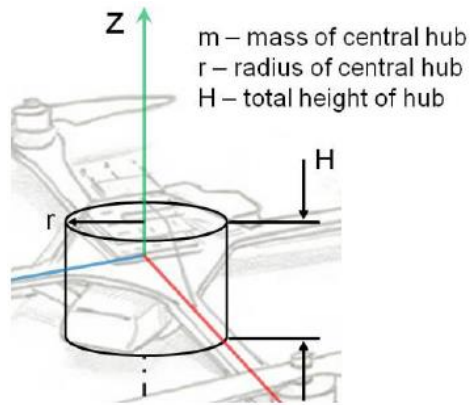


Figure 3.0.5: Moment calculation 3

$$J_{x,H} = J_{y,H} = \left[\frac{1}{4} m r^2 + \frac{1}{12} m H^2 \right]$$

$$J_{z,H} = \left[\frac{1}{2} m r^2 \right]$$

Arms:

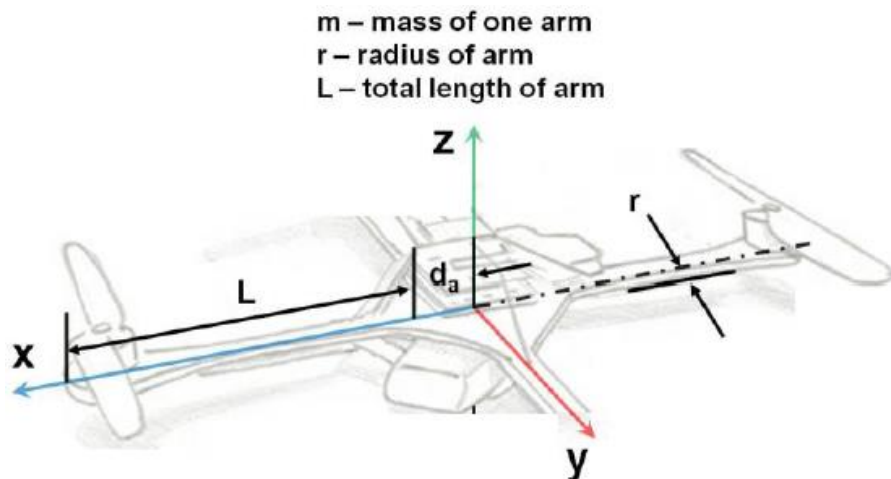


Figure 3.0.6: Moment calculation 5

$$J_{x,A} = J_{y,A} = 2 \left[\frac{1}{2} m r^2 \right] + 2 \left[\frac{1}{4} m r^2 + \frac{1}{3} m L^2 + m d_A^2 \right]$$

$$J_{z,A} = 4 \left[\frac{1}{4} m r^2 + \frac{1}{3} m L^2 + m d_A^2 \right]$$

$$\therefore J_i = J_{i,M} + J_{i,S} + J_{i,H} + J_{i,A} \text{ for } i = x, y, z$$

The sole internal driving force behind our UAVs movement lies within the thrusts generated by the motors and propellers perpendicular to the X^b - Y^b plane of the body frame of reference ($+Z^b$ direction). The thrust T , provided by a single motor/propeller setup is defined by:

$$T = C_T \rho A_r r^2 \bar{\omega}^2$$

Here C_T is the thrust coefficient for a specific rotor, ρ is the density of air, A_r is the cross-sectional area of the propeller's rotation, r is the radius of the rotor, and $\bar{\omega}$ is the angular velocity of the rotor. In order to further simplify the characterization process, we lump $\rho A_r r^2$ parameters into C_T to obtain the thrust coefficient relation:

$$T = C_T \bar{\omega}^2$$

The torque force of the motor/prop system can be determined in a similar fashion to that of the thrust tests. The torque Coefficient relations is:

$$Q = C_q \bar{\omega}^2$$

In this case, Q is the torque created by the motor and C_q is the torque coefficient for the motor/prop system.

We can now create a matrix which describes the thrusts and torques on the system:

$$d_+ = \text{Arm Length from quadcopter hub center to motor center}$$

$$d_x = d_+ \sin(45^\circ)$$

$$\begin{bmatrix} \sum T \\ \tau_\phi \\ \tau_\theta \\ \tau_\psi \end{bmatrix} = \begin{bmatrix} C_T & C_T & C_T & C_T \\ -d_x C_T & d_x C_T & d_x C_T & -d_x C_T \\ -d_x C_T & -d_x C_T & d_x C_T & d_x C_T \\ -C_q & C_q & -C_q & C_q \end{bmatrix} \begin{bmatrix} \bar{\omega}_1^2 \\ \bar{\omega}_2^2 \\ \bar{\omega}_3^2 \\ \bar{\omega}_4^2 \end{bmatrix}$$

For control purposes a linear regression is needed that will translate throttle command values (as percent throttle) to RPM values.

$$\bar{\omega}_{ss} = (\text{Throttle}\% * C_r) + b$$

Here $\bar{\omega}_{ss}$ is the expected steady-state motor RPM, $Throttle\%$ is the throttle percentage command, C_r is the throttle % to RPM conversion coefficient, and b is the y-intercept of the linear regression relationship.

The phenomenon of gyroscopic precession occurs when the axis of rotation of a rotating body is changed, and must be accounted for in our model. The gyroscopic forces resulting on the body are governed by the inertia of each motor's rotating components (J_m), the rolling and pitching rates (P,Q), as well as the speed of each motor/prop system ($\bar{\omega}_i$). The gyroscopic torques for pitch and roll action are:

$$\tau_{\phi gyro} = J_m Q \left(\frac{\pi}{30} \right) (\bar{\omega}_1 - \bar{\omega}_2 + \bar{\omega}_3 - \bar{\omega}_4)$$

$$\tau_{\theta gyro} = J_m P \left(\frac{\pi}{30} \right) (-\bar{\omega}_1 + \bar{\omega}_2 - \bar{\omega}_3 + \bar{\omega}_4)$$

(Note: The $\frac{\pi}{30}$ term corresponds to the transition from RPM to radians)

Our new resulting matrix will account for the mentioned gyroscopic, and thrust moments created by the motor/prop systems on our UAV:

$$M_{A,T}^b = \begin{bmatrix} d_+ C_T \bar{\omega}_2^2 - d_+ C_T \bar{\omega}_4^2 + J_m Q \left(\frac{\pi}{30} \right) (\bar{\omega}_1 - \bar{\omega}_2 + \bar{\omega}_3 - \bar{\omega}_4) \\ -d_+ C_T \bar{\omega}_1^2 + d_+ C_T \bar{\omega}_3^2 + J_m P \left(\frac{\pi}{30} \right) (-\bar{\omega}_1 + \bar{\omega}_2 - \bar{\omega}_3 + \bar{\omega}_4) \\ -C_q \bar{\omega}_1 + C_q \bar{\omega}_2 - C_q \bar{\omega}_3 + C_q \bar{\omega}_4 \end{bmatrix}$$

$M_{A,T}^b$ refers to the moments present in the body frame resulting from the thrusts, and torques on the system. The lift force can be expressed:

$$F_{A,T}^b = \begin{bmatrix} 0 \\ 0 \\ C_T (\bar{\omega}_1 + \bar{\omega}_2 + \bar{\omega}_3 + \bar{\omega}_4) \end{bmatrix}$$

$F_{A,T}^b$ refers to the forces acting in the body frame on the quadcopter due to thrust.

State equations that define this simplified dynamic model need to be defined. The first is the Angular Velocity state equation:

$${}^b \dot{\omega}_{b|i} = (J^b)^{-1} [M_{A,T}^b - \Omega_{b|i}^b J^b \omega_{b|i}^b] = \begin{bmatrix} \dot{P} \\ \dot{Q} \\ \dot{R} \end{bmatrix}$$

This equation describes the change in roll (P), pitch (Q), and yaw (R) rates of the quadcopter by taking into account the inertia, angular velocity, and the moments applied by the motor/prop systems. ${}^b\dot{\omega}_{b|i}$ is the angular acceleration across each axis in the body frame with respect to the inertial frame, and is simplified to:

$${}^b\dot{\omega}_{b|i} = \begin{bmatrix} \dot{P} \\ \dot{Q} \\ \dot{R} \end{bmatrix}$$

The cross-product matrix for rotational velocity, $\Omega_{b|i}^b$, and the rotational velocity of the quadcopter body within the body frame with respect to inertial frame (earth frame), $\omega_{b|i}^b$, are defined as:

$$\Omega_{b|i}^b = \begin{bmatrix} 0 & -R & Q \\ R & 0 & -P \\ -Q & P & 0 \end{bmatrix}$$

$$\omega_{b|i}^b = \begin{bmatrix} P \\ Q \\ R \end{bmatrix}$$

The Euler Kinematic Equation, which allows us to determine the rate of change of the Euler angles in the inertial frame is:

$$\dot{\Phi} = H(\Phi)\omega_{b|i}^b = \begin{bmatrix} \dot{\phi} \\ \dot{\theta} \\ \dot{\psi} \end{bmatrix}$$

Using yaw, pitch, and roll rotations a composite rotation matrix can be created which can transform the motion of the UAV from the body frame to a new reference frame. The resulting rotation matrix transforms rotations from the body frame with respect to the inertial frame and can be found using matrix multiplication.

$$u^b = \begin{bmatrix} 1 & 0 & 0 \\ 0 & \cos(\phi) & \sin(\phi) \\ 0 & -\sin(\phi) & \cos(\phi) \end{bmatrix} \begin{bmatrix} \cos(\theta) & 0 & -\sin(\theta) \\ 0 & 1 & 0 \\ \sin(\theta) & 0 & \cos(\theta) \end{bmatrix} \begin{bmatrix} \cos(\psi) & \sin(\psi) & 0 \\ -\sin(\psi) & \cos(\psi) & 0 \\ 0 & 0 & 1 \end{bmatrix} u^i$$

The resulting matrix multiplication yields the rotation matrix from the inertial to the body frame using the rotation sequence:

$$C_{b|i} = \begin{bmatrix} \cos(\theta)\cos(\psi) & \cos(\theta)\sin(\psi) & -\sin(\theta) \\ (-\cos(\phi)\sin(\psi) + \sin(\phi)\sin(\theta)\cos(\psi)) & (\cos(\phi)\sin(\psi) + \sin(\phi)\sin(\theta)\sin(\psi)) & \sin(\phi)\cos(\theta) \\ (\sin(\phi)\sin(\psi) + \cos(\phi)\sin(\theta)\cos(\psi)) & (-\sin(\phi)\cos(\psi) + \cos(\phi)\sin(\theta)\sin(\psi)) & \cos(\phi)\cos(\theta) \end{bmatrix}$$

This rotation matrix is integral to solving the velocity and position state equations, however that derivation is beyond the scope of this work. Continuing, the angular velocity of the aircraft in the body frame can be related to the changes in angle rotation as shown below, where the C matrices of ϕ and θ are those from u^b .

$$\omega_{b|i}^b = \begin{bmatrix} \dot{\phi} \\ 0 \\ 0 \end{bmatrix} + C_\phi \left(\begin{bmatrix} 0 \\ \dot{\theta} \\ 0 \end{bmatrix} + C_\theta \begin{bmatrix} 0 \\ 0 \\ \dot{\psi} \end{bmatrix} \right)$$

The resulting Euler Kinematic Equation is [61]:

$$\dot{\Phi} = \begin{bmatrix} \dot{\phi} \\ \dot{\theta} \\ \dot{\psi} \end{bmatrix} = \begin{bmatrix} 1 & \tan(\theta) \sin(\phi) & \tan(\theta) \cos(\phi) \\ 0 & \cos(\phi) & -\sin(\phi) \\ 0 & \sin(\phi)/\cos(\theta) & \cos(\phi)/\cos(\theta) \end{bmatrix} \begin{bmatrix} P \\ Q \\ R \end{bmatrix} = H(\Phi) \omega_{b|i}^b$$

The velocity state equation describes the acceleration of the center of mass of the rigid body UAV model based on the forces and accelerations acting on the body.

$${}^b \dot{v}_{CM|i}^b = \left(\frac{1}{m} \right) F_{A,T}^b + g^b - \Omega_{b|i}^b \omega_{CM|i}^b = \begin{bmatrix} \dot{U} \\ \dot{V} \\ \dot{W} \end{bmatrix}$$

${}^b \dot{v}_{CM|i}^b$ is the linear acceleration of the center of mass in the body frame with respect to the inertial frame. Here m is the total mass of the UAV, and g^b is the acceleration of gravity translated to act in the body frame by the rotation matrix $C_{b|i}$.

$$g^b = C_{b|i} g^i$$

The position state equation, describes the linear velocity of the center of mass of the UAV in the inertial frame.

$${}^i \dot{P}_{CM|i}^i = C_{i|b} v_{CM|i}^b = \begin{bmatrix} \dot{X} \\ \dot{Y} \\ \dot{Z} \end{bmatrix}$$

$$C_{i|b} = [C_{b|i}]^T$$

Here $[C_{b|i}]^T$ represents the transpose of $[C_{b|i}]$. ${}^i \dot{P}_{CM|i}^i$ is the velocity of the UAV in the body frame that is rotated into the inertial frame. This equation is crucial, and allows us to determine the velocity of the quadcopter in the X, Y, and Z directions of the inertial frame (earth frame of reference) within our mathematical model and further simulations. Armed with both velocity and position state equations we can continue on to make use of powerful tools like MATLAB and Simulink, which enable us to seamlessly introduce a virtual PID control similar to that of a flight controller, further maturing our overall model.

CHAPTER 4: MATLAB-SIMULINK CONTROL MODELING & SIMULATION

4.1 PID Controller Theory

Our proposed X8 octa-quad UAV design is inherently unstable, naturally trending towards unstable values of torque in $\omega_{b|i}^b$, and requiring continuous motor thrust control to function properly. All destabilizing external or internal inputs can be represented as a step input disturbance which our control system must counteract to achieve steady state stability (steady flight). Fortunately, this sort of control problem is so universal that PID control has become a commonplace and heavily utilized technique. Basic PID control structure in its complete form consists of Proportional, Integral and Derivative parts (PID). In this section the separate parts are described with their respective characteristics, beginning with proportional control, (K_p), which acts to reduce the rise time of the system. Observe that with pure proportional control, it is typical for UAV plant model steady state errors occur in response to a step input.

If an integral controller (K_I) is added, then the steady state error can be reduced, as the error over time will be summed and taken into consideration. Note that integral action, while removing the offset or steady-state error, may lead to oscillatory response of slowly decreasing or increasing amplitude, both of which are usually undesirable. Additionally, when control saturation occurs integrator windup may occur. This should be avoided as overshooting in the plant response creates a progressively unstable system.

When we finally add derivative control (K_D) to the mix, we provide a means of obtaining a controller with high sensitivity, in other words, it improves the transient response. For a step input, this means that the overshoot is reduced. An advantage if using derivative control is that it responds to the rate of change of the actuating error and can produce a significant correction before the magnitude of the actuating error becomes too large, thus improving the overall stability of the system. Although derivative control does not affect the steady-state error directly, it adds damping to the system and permits the use of a larger value of the proportional gain with lowered risk of oscillation, which will result in an improvement in the steady-state accuracy. Table 4.1 below summarizes the impact of combining the Proportional Integral and Derivative control. This can be applied to concurrently reduce rise time, reduce maximum overshoot and remove the steady state error in many systems. The continuous time PID control law as described by the transfer function:

$$K(s) = K_p + \frac{K_I}{s} + K_D s$$

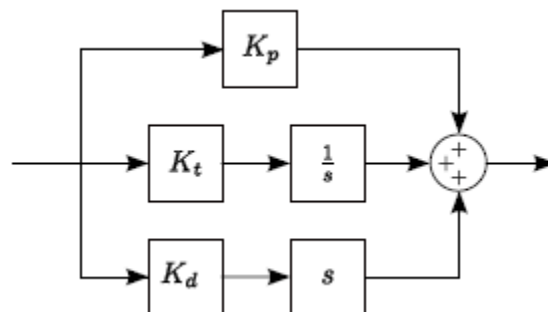


Figure 4.1: General PID Control Structure

Table 4.1: The effects of increasing each of the controller parameters

PID Parameter	Δ	Rise Time	Overshoot	Settling Time	Steady State Error
K_P	\uparrow	Decrease	Increase	Non-Definitive	Decrease
K_I	\uparrow	Decrease	Increase	Increase	Eliminates
K_D	\uparrow	Non-Definitive	Decrease	Decrease	Non-Definitive

4.2 Tuning PID

Figure 4.2 below depicts different open loop responses for a system which was introduced to step impulse similar to the impulse that would throw a UAV out of balance if uncorrected over time. Here, 1 is the desired steady state value representing level UAV attitude, and we judge the performance of a system by how quickly it converges to that value ($e_{SS} = 0$), without further oscillation (t_{SS}). In some cases, the maximum overshoot (M_P) and rise time (t_r) are viewed as critical parameters. For this work these parameters are observed but not optimized, as stability problems were adequately resolved once t_{SS} was sufficiently minimized.

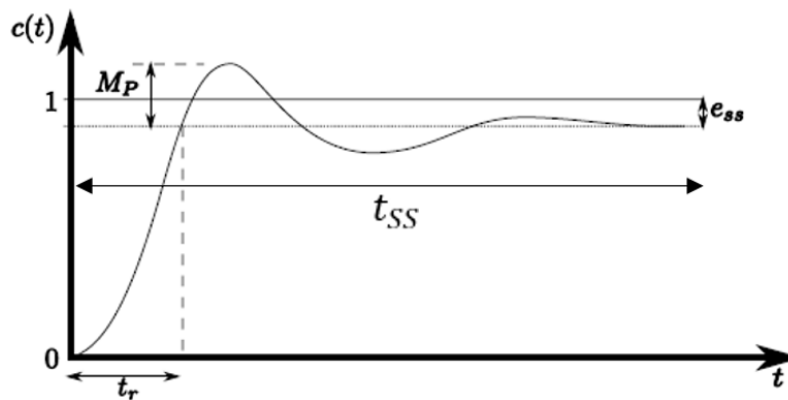


Figure 4.2: Example of typical response to a unit step input of a system

Achieving the optimum values for each control parameter is a field of study on its own, and beyond the scope of this work. However, using modern optimization techniques, it is possible to tune PID control parameters K_P , K_I , and K_D if the transfer function of the plant is known, to optimize the closed-loop performance. For example, The Ziegler-Nichols tuning rule is often used as a basis for which iterative increasing or decreasing of control parameters is dependent on error based performance indices. It's worth remarking that different control performance indices (methods) certainly generate different control parameters which each are superior to Ziegler-Nichols at different degrees. This further accents the breath of this study, since one method of "optimization" gives superior step responses than another.

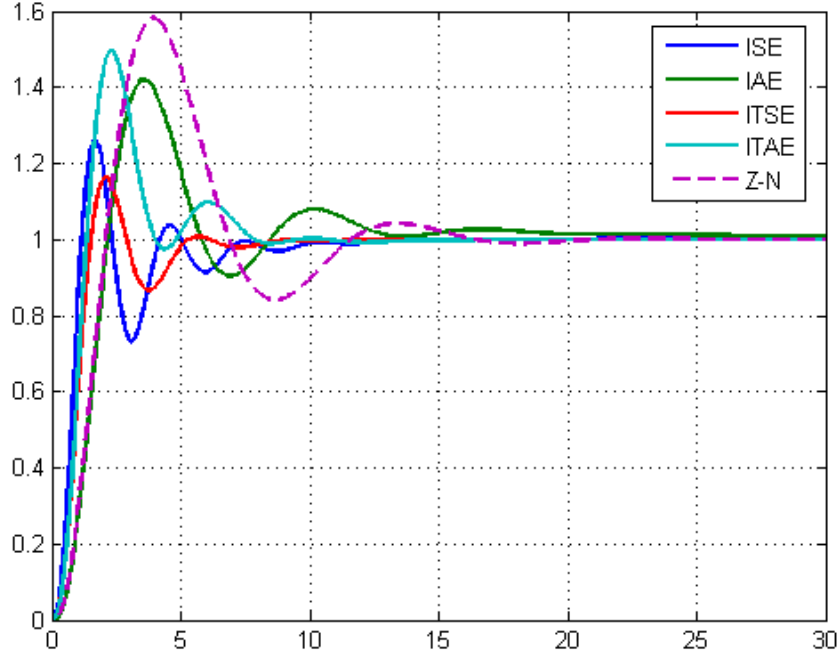


Figure 4.3: Different performances for different parameters in response to the same impulse [66]

Each of the trails were run under different integral control performance indices [65].

The Integral of Squared Error (ISE):

$$I_1 = \int_0^{\infty} e^2(t)dt$$

The Integral of Absolute Error (IAE)

$$I_2 = \int_0^{\infty} |e(t)|dt$$

The Integral of Time Multiply Squared Error (ITSE)

$$I_3 = \int_0^{\infty} te^2(t)dt$$

The Integral of Time multiply Absolute Error (ITAE)

$$I_4 = \int_0^{\infty} te^2(t)dt$$

Though all methods improve on the Ziegler-Nichols tuning rule, ITSE method performed the best. This again highlights how different values of K_P , K_I , and K_D may result in different combinations of t_{SS} , M_P , and t_r . Several tuning algorithms have been developed for tuning PID controllers. Ziegler-Nichols and Lambda tuning may be most famous but, as seen above, can certainly be improved upon. Many previous projects ([66]), have successfully made use of an

iterative tuning method employing elements from Table 4.1 above with the following progressive algorithm, employed in this work:

1. Investigate step response
2. If rise time t_r needs to be reduced, increase the value of K_P
3. If maximum overshoot M_P needs to be reduced, increase the value of K_D
4. If steady state error e_{SS} is persistent, increase the value of K_I
5. Repeat gains adjustment until desired response time (t_{SS}) is obtained

A drawback of this method is that it lacks the ability to determine when the initially selected conditions for gain parameters K_P , K_I , and K_D might be too large, a problem seen later to plague the first prototype described in later chapters. For example, elongated oscillations just prior to achieving steady state can be caused by excessive integral gain (K_I). This can be remedied by either decreasing K_I or increasing K_D , whereas the above approach gives sole preferences to always increasing K_D , possibly resulting in increased t_{SS} .

4.3 Simulink Control Model

The UAVs attitude is at all times determined by the values of Roll (ϕ), Pitch (θ) and Yaw (ψ) with respect to earth (inertial frame). In order to maintain balance and achieve useful flight, these parameters must be continuously adjusted. Both our Simulink model and physical microcontrollers employ the aforementioned PID control method to steer these variables as desired. Figure 4.4 shows is a Simulink object oriented example of PID. First, note that the feedback element is derived from the desired Z state variable (generated elsewhere), and that the case of altitude is unique as it requires a +Z gravity offset to account for the constant force of gravity in the -Z direction. Such an offset is not required for the Roll, Pitch and Yaw PID controllers, which are otherwise identical in structure.

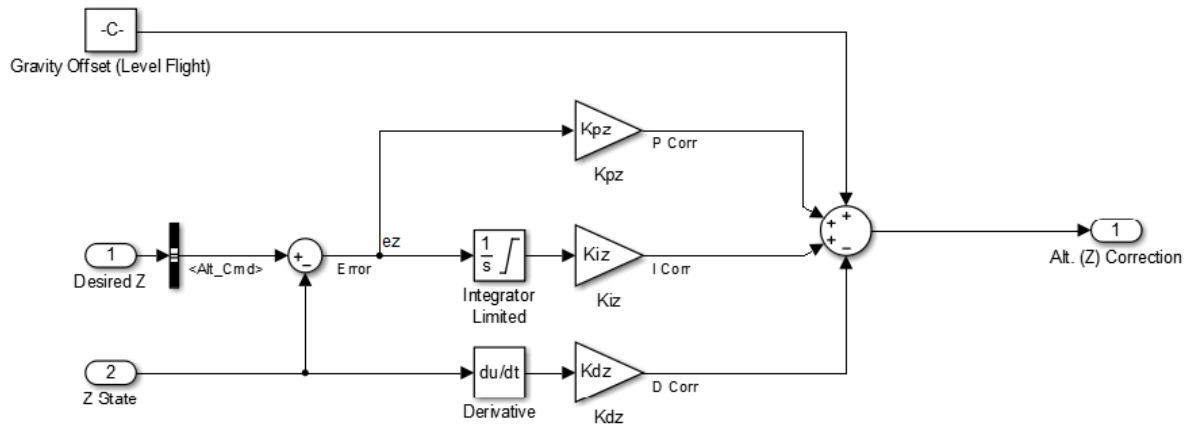


Figure 4.4: Example Elevation PID controller

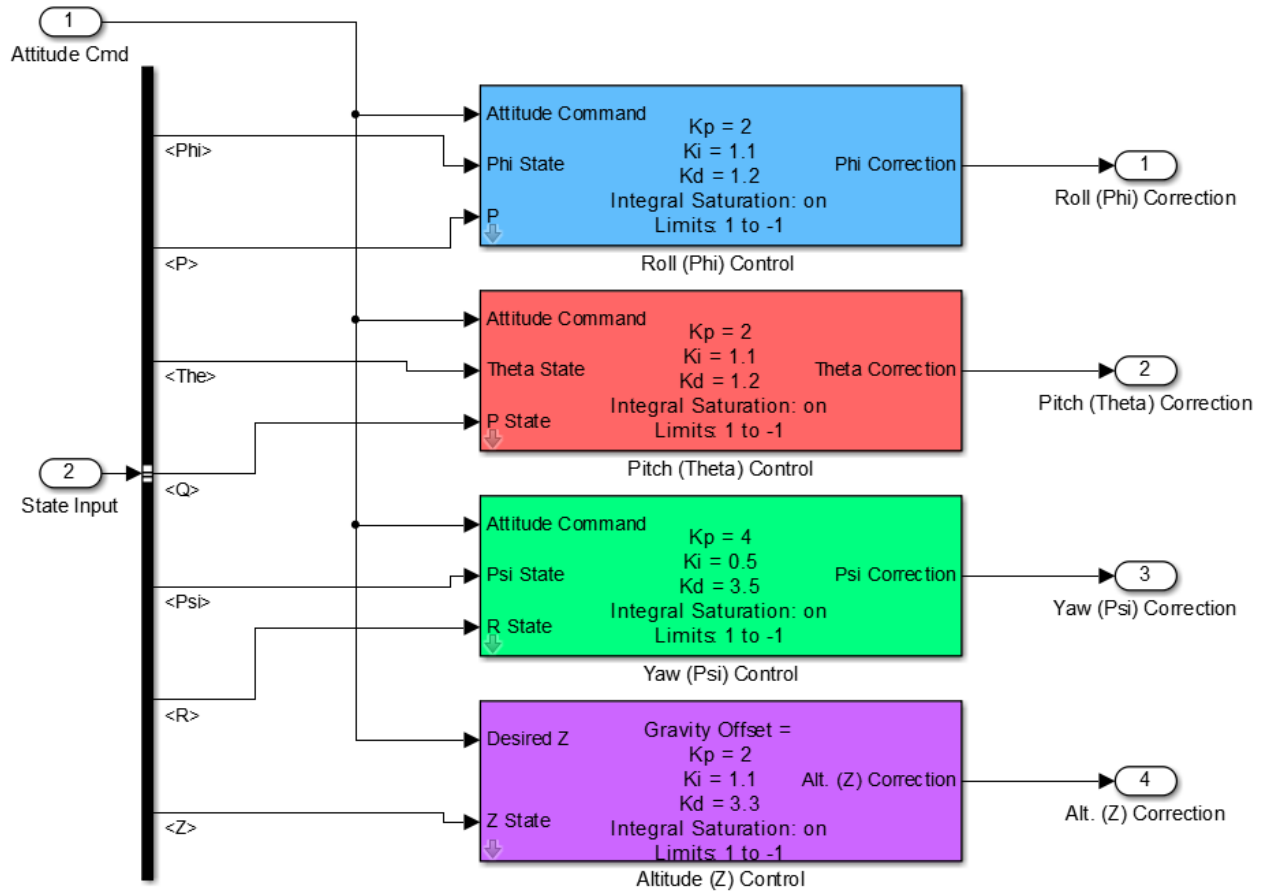


Figure 4.5: Complete Attitude Controller

We obtain a complete attitude controller as shown in figure 4.5 above by replicating the PID control for altitude (Z) across ϕ , θ , and ψ as well. In this manner, we have acquired correction parameters scaled to match the degree of error within each desired value of ϕ , θ , ψ , and Z . If we now translate these correction parameters into specific motor torques for each motor, we can achieve stabilized controlled flight in both virtual and physical realms.

4.4 Simulink Simulation

Figure 4.6 below depicts how specific motions are achieved by a Quadcopter UAV. We must again invoke the assumption equalant motor attributes transferable from an arm on our X8 Octaquad to an arm on a Quadcopter UAV. If we again assume symmetry and that the center of gravity of the UAV is also the geometric center, stable (hover) flight is achieved when all four motors have exactly the same RPM and generate equal thrusts and torques. In this situation, the torques created by each of the motors will cancel out, holding the direction of the aircraft fixed. If the downward thrust generated is enough to counteract the force of gravity acting on the UAV

it may hover or increase in elevation, otherwise it will descend at a rate relative to the difference in gravitational force and the total thrust downward. For forwards/backwards, or left/right flight in the inertial frame (Roll and Pitch), the relative RPM (and proportionally relative thrust) of two motors normal to each other on the XY plane (Body frame) must be greater than the RPM of the other opposing motors. This temporarily creates an imbalance in the thrust which begins to rotate the UAV about the ϕ -axis or θ -axis as desired. Similarly turning (yawing) in the inertial frame is achieved by having two motors on opposing arms sustain higher relative RPM than the motors they are normal to in the X-Y plane of the body frame of reference. The direction the UAV turns in depends on which set of motors has the relative boost in RPM.

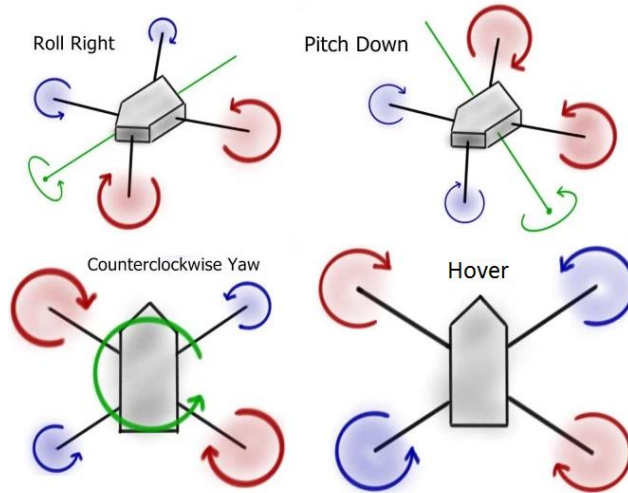


Figure 4.6: Quad UAV execution of Roll, Pitch, Yaw and Hover [69]

Combining the control systems generated by the attitude control block is imperative to our simulation. This must be done in a fashion shown in Figure 4.7, such that when the previously mentioned relative RPM scenarios occur for a given input command into the attitude controller. The mixing terms for motor controllers 1-4, M_{c1} , M_{c2} , M_{c3} , and M_{c4} are used within our model to set the RPM for each motor. It may not be entirely intuitive, but each M_{c-i}^{th} summation of correction variables does indeed produce the desired effect. A simple check on this can be reached by analysing the altitude correction term. Note that this term is added to and is directly proportional to the overall value of each motor. As we would expect, when the desired altitude is lower than requested from the Desired Z variable in our PID control, the Altitude correction term will be positive. This in turn will equally increase the values for all M_{c-i}^{th} , resulting in a net increase in RPM and downward thrust produced by all motors, bringing the UAV closer to the desired height. A similar check can be performed on the effects of increase or decreasing ϕ -correction, θ -correction, or ψ -correction terms.

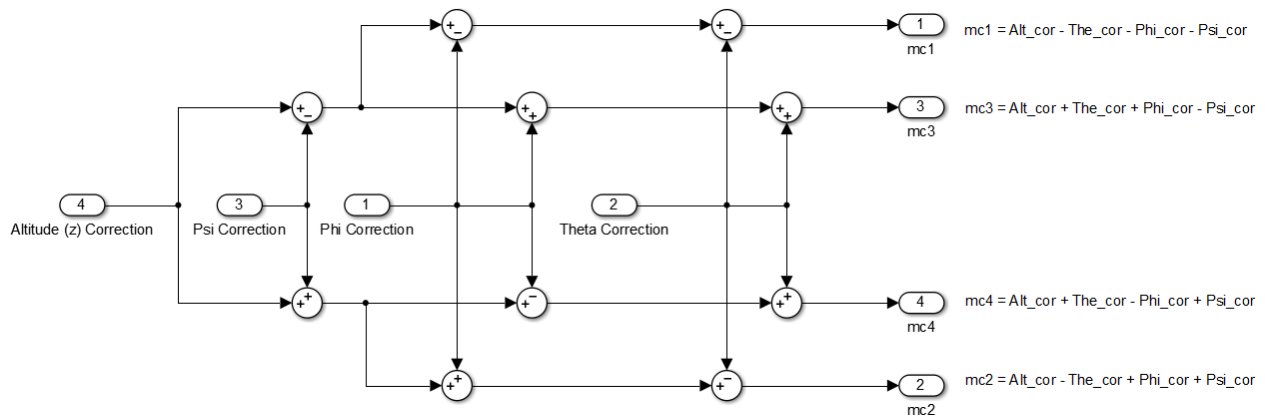


Figure 4.7: Control mixing of correction commands to UAV motors

In order to properly simulate how the UAV will respond to attitude commands, a position controller block which generates attitude commands is required. Figures 4.8, 4.9 and 4.10 depict the block level, component level and PID structures of the position controller respectively. Note that this block is given inputs of typical inputs of heading (ψ), altitude (Z), and speed in component terms of X-velocity and Y-velocity in the earth frame of reference. ϕ and θ are derived trigonometry and are combined with the ψ and Z to serve as inputs into the attitude controller block. Note that the path commands themselves exist in a pre-generated MATLAB file containing all command values for each instance of a clock iteration within our simulation (.: for each cycle).

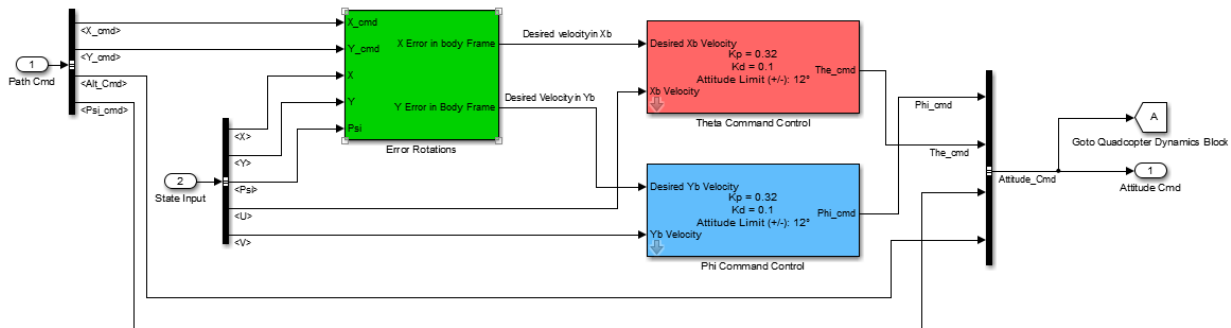


Figure 4.8: Simulation position controller block

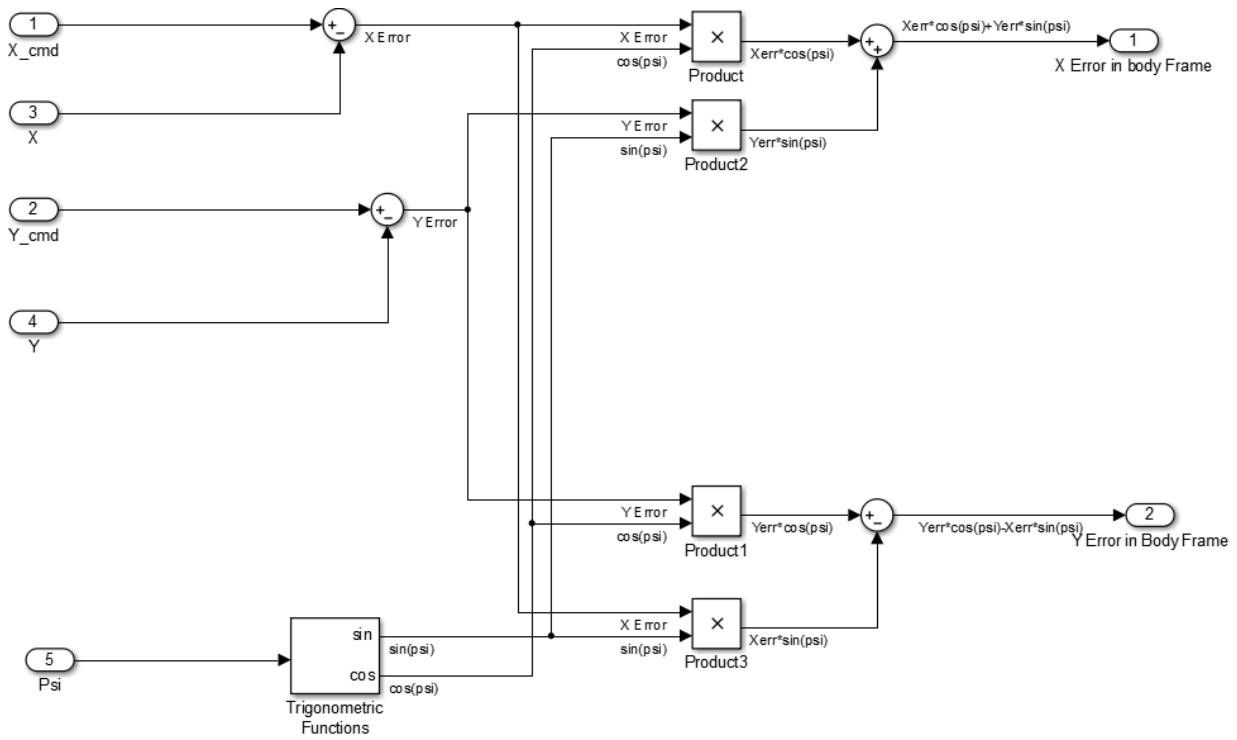


Figure 4.9: Path command error signal generation

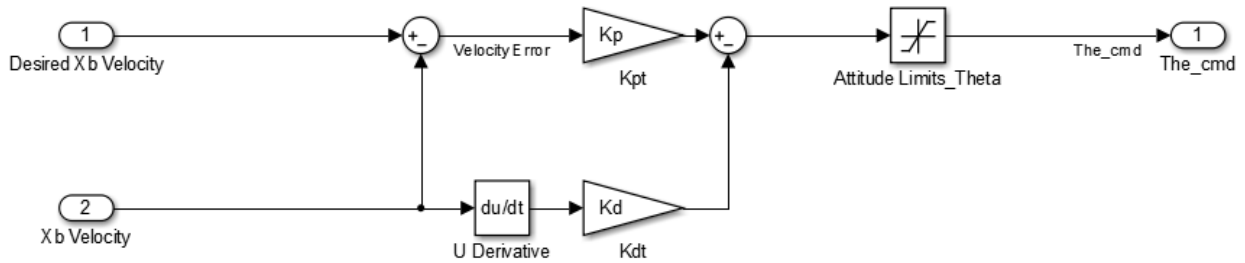


Figure 4.10: PD Control setup for Theta and Phi command control

The state space equations which describe the dynamic behavior of the UAV generated in chapter 3 are simulated in a level 2 S-Function written in the MATLAB language. The code for this block is found in the appendix. In addition, the simulating of earth ground, variables such as the UAV velocity, altitude and position are tracked, held, and refreshed within this block for both earth and body frames of reference. The Quadcopter Dynamics block outputs this data back into the position and attitude controller blocks, which generates the feedback required for PID control. Below, the complete simulation setup at the block level is shown.

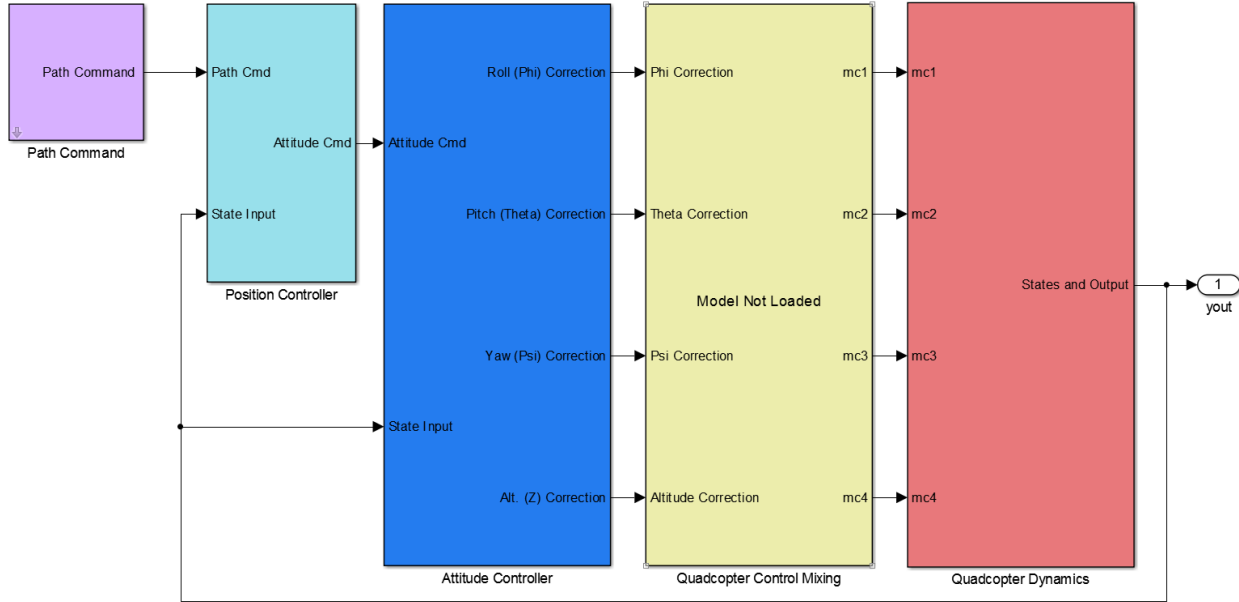


Figure 4.11: Complete simulation setup

However, this simulation still requires information describing the UAVs mass, and moment of inertia to plug into our mathematical model. The gross weight of the UAV (M), components of moment of inertia (J_x, J_y, J_z), are calculated using data from table 4.2 and further used to generate J^b as depicted in the previous chapter.

Table 4.2: Example Moment of Inertia Data

Motors	ESC's	Central Hub	Arms
Mass = 75 g	Mass = 31 g	Mass = 431 g	Mass = 45 g
dm = 21.225 cm	a = 2.54 cm	r = 5.6388 cm	r = 3.25374
H = 3.175 cm	b = 5.715 cm	H = 4.28625 cm	L = 18.5738
r = 1.40335 cm	ds = 8.255 cm		da = 5.08

Additionally, motor test values are also key to simulating Thrusts (T), Torques (Q), and motor angular velocities ($\bar{\omega}_{SS}$) and must be entered into the simulation with parameters shown in table 4.3. These values can be generated via a test bench as described in [64], however this work used data from the supplier of our motors and propellers to attain the required constants. In some cases, a regression was needed to acquire greater precision, as will be shown later.

Table 4.3: Example Test Data

Thrust coefficient: C_t	1.4865e-07 N/RPM ²
Torque coefficient: C_q	2.925e-09 n*m/RPM ²
Throttle % to RPM: C_r	80.584
Anglur Velocity RPM Offset: b	976.2
Simulation Time Constant: τ	.076
Minimum Throttle %	5%

4.5 Conclusion

Simulation challenges and accuracy rest in the ability to adequately tune PID control parameters, as well as accurately measuring the attributes of our physical design. That being said, the great advantage from this simulation format is its flexibility in analyzing many different quadcopter setups. By simply modifying variable values in the above tables, we can transition from one type of theoretical UAV to another, without incurring any additional cost. This feature is critical to our quadcopter design and by the extension critical to the overall optimized system design which this work proposes.

CHAPTER 5: SYSTEM PROTOTYPE IMPLIMENTATION

5.1 Simulink Modeling

Before dedicating time and resources towards a specific design, we must first make use of available modeling and simulation tools. By doing so, we can narrow in on desired design parameters and characteristics that may otherwise remain nebulous. Throughout the simulation test trails, we strived to obtain a reasonable goal for the UAVs mass, as well as to generate a simulation variable set that would achieve stable flight below 50% throttle. This throttle percent objective takes into consideration that a payload will need to be added, requiring the UAV to increase its stable flight throttle by an additional 20-30%. Initially, parameters such as those in Table 5.1 were selected superfluously or at random. As motor testing and parts research was conducted, more realistic and precise simulation variables were acquired. Table 5.1 depicts the set of parameters used as a standard bearer for version 1 (V1) of our UAV prototype, totaling 8 kg in mass.

Table 5.1: Simulation Input Data

Motors	ESC's	Central Hub	Arms
Mass = 150 g	Mass = 250 g	Mass = 6000 g	Mass = 100 g
dm = 50 cm	a = 2.54 cm	r = 10.0 cm	r = 1.27 cm
H = 5.0 cm	b = 5.0 cm	H = 30.0 cm	L = 42 cm
r = 2.5 cm	ds = 5.0 cm		da = 10 cm
Thrust coefficient: C_t		2.0e-06 N/RPM ²	
Torque coefficient: C_q		2.2e-07 Nm/RPM ²	
Throttle % to RPM: C_r		46.48	
Anglur Velocity RPM Offset: b		1000	
Simulation Time Constant: τ		.076	
Minimum Throttle %		5%	

Flight simulation with a payload was not accurately simulated beyond increasing the mass of the central hub. This is because the physical makeup of how the payload would be attached to the UAV was far from inception at the beginning on this work, when much of our initial simulation took place. Though modifying the central hub's mass assumes the payload is rigid, centered about the geometric center of the UAV, and evenly distributed. Without a specific physical design, arbitrarily modeling the eventual payload as a block of mass under then UAV can't be guaranteed to be significantly more accurate than increasing the mass of the central hub, thus such modeling was evaded.

It's at this point that an X8 octa-quad design was determined to be best suited for our UAV prototype. First, the addition of four downward facing motors will allow for double the total thrust of a quadrotor design, making it possible to maneuver a heavier UAV and carry heavier payloads. Secondly, the counteracting torques at each motor mount will be able to balance out, or at least be reduced relative to quadrotors, likely improving the UAVs stability. Lastly, the use of advanced CPU algorithms and circuit designs could be employed to use the upper and lower sets of motors independently. This could prove useful in the event of motor failure.

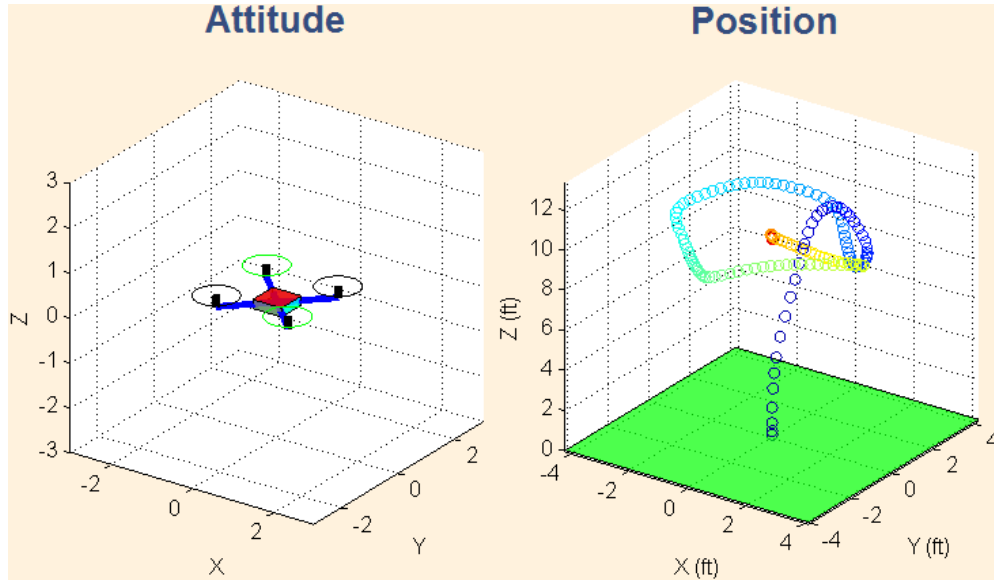


Figure 5.1: Simulation attitude and position 3D views

Figures 5.1 and 5.2 depict the dynamic diamond flight path selected for all simulations, and is specific to data from Table 5.1. This path was chosen for its inclusion of takeoff, midair decent, 90-degree angle turns in the top view plane, straight line, and hover actions. All of these actions are expected to also be testing on the prototype in the field. The flight path initiates at the base where the circles are dark blue, and terminates in the air where the circles are dark red. Each simulation was executed over a 45 second interval, logging all relevant variables (graphed in Figure 5.4) at each sampling node, with the number of samples dependent on the simulation time constant τ . Figure 5.3 shows the desired motor throttle command % and RPM for an 8kg UAV, which is fairly identical for all motors. We see that the initial takeoff required 52% throttle (4100 RPM), and stable flight at a 10ft altitude was manageable around 46% throttle (3600 RPM). The low velocities are not a concern as attitude angles no larger than 3% were used for lateral motion, and the desired liftoff velocity is more or less user defined.

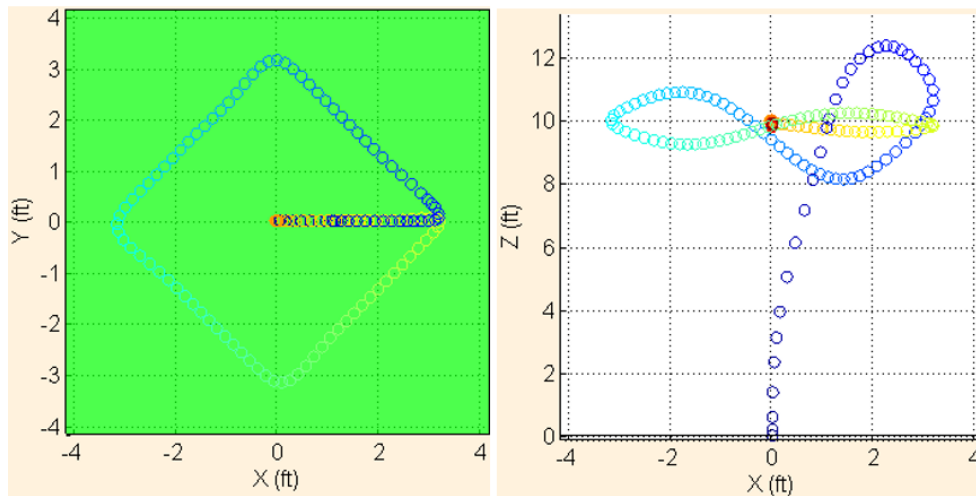


Figure 5.2: Top and side views of simulated flight path

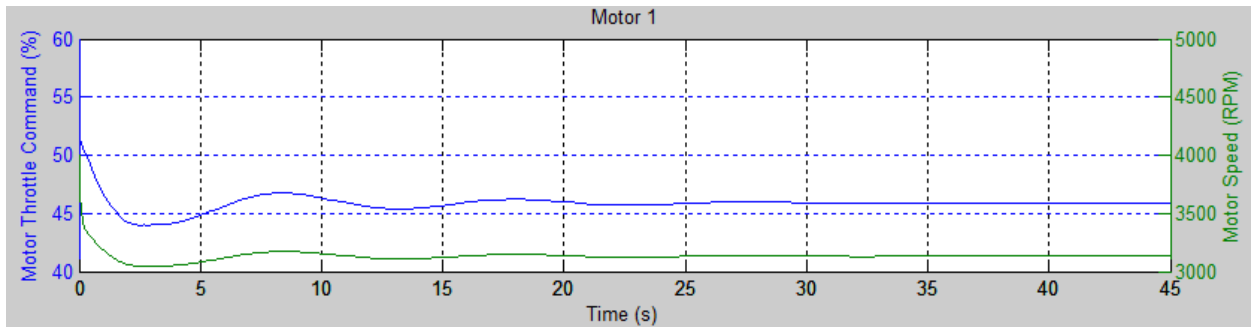


Figure 5.3: Motor simulation results from Table 5.1 simulation

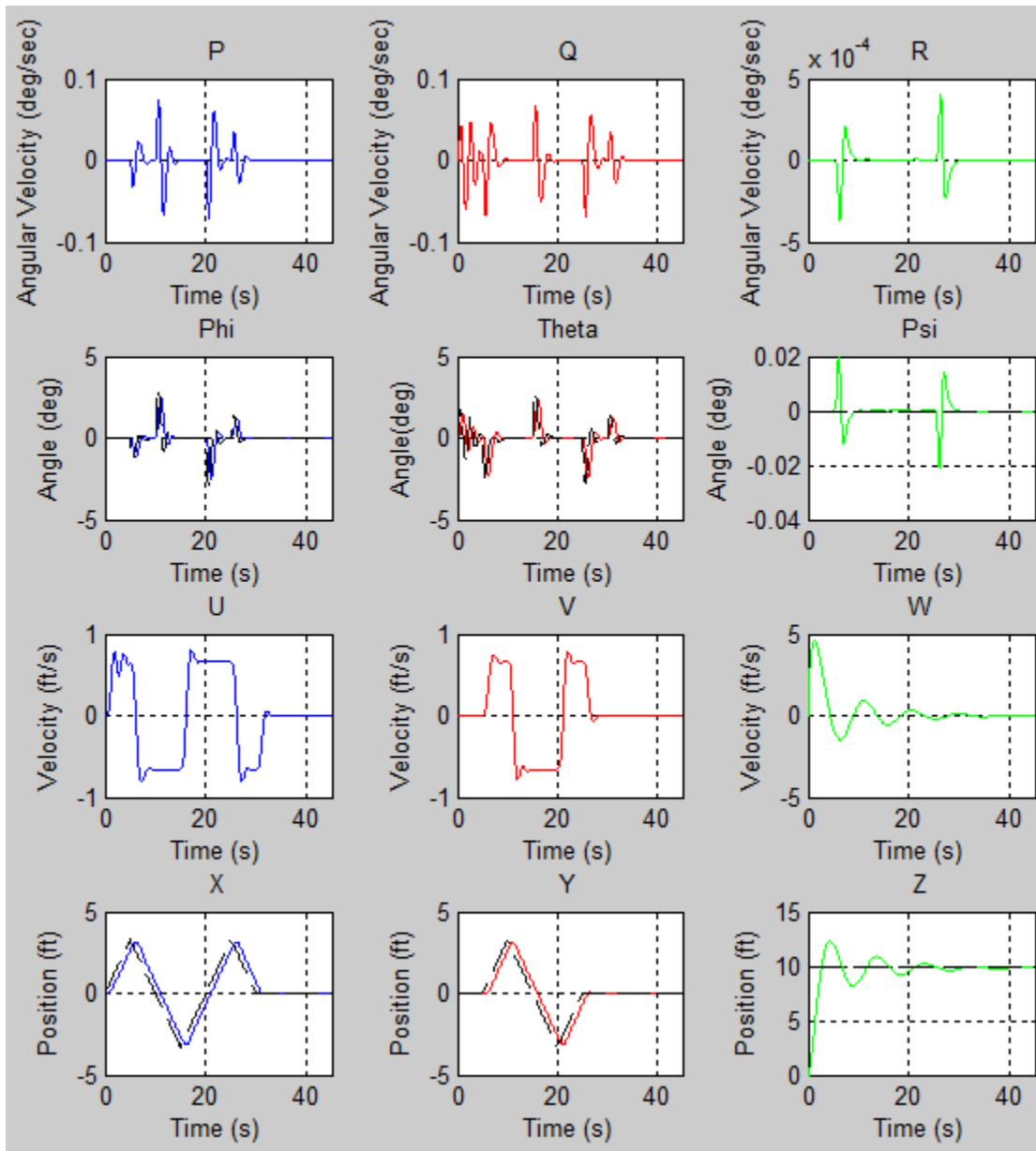


Figure 5.4: UAV kinematic simulation results for $PQR(X,Y,Z)$

5.2 Version 1

-Motor selection

Selecting an appropriate motor is key to any multirotor design. Since manufacturing of this component required resources that were not readily available (metal CNC machine), commercial brushless DC motors were purchased and tested. The onset of this project sought the acquisition of a quick response, efficient, thrust maximizing motor. The requirements highlighted in the previous chapter required that the sum of thrusts produced by all motors be able to support a UAV with an 8kg all up weight, which can simultaneously manage an 8kg payload. From this we conclude that the desired UAV requires the ability to generate a minimum of 157 Newtons of downward thrust to simply hover. When this research began, few suppliers provided motor test data for their brushless DC motors, making it initially difficult to select appropriate motors for testing. Additionally, the public UAV market was at this point (and even still today) very unaccustomed to multirotors handling such payloads, indeed the search was an anomalous endeavor. The best results were found while researching a competition held by Hobby King, a U.S. based complete 3rd party supplier of commercial/hobby UAV products. The Hobby King Dead Lift competition challenged people across the country to use products they sold to design a UAV which could lift the heaviest payload for a set period of time. The competitors with the best results, including the winners of the competition, utilized the Turnigy G60 brushless DC motor within their respective designs. Unfortunately true to form, sufficient motor test data was nowhere to be found on the retailers website. Thus, this motor was selected, and immediately needed to undergo testing.



Figure 5.5: Turnigy G60 motor testing apparatus

The G60 motor testing apparatus can be seen in Figure 5.5. The setup was designed to acquire data on motor current consumption at various throttle levels to be followed with thrust data acquisition. The system was powered by a Turnigy Nanotech 5000mAh 25-50C battery, with a nominal charge of 22 volts, and capable of safely deliver 125-250 Amperes. Unseen in figure 5.5 is the Mystery Fire Dragon brand 100-amp electronic speed controller (ESC), along with internal electronics which allowed for control of the throttle level via an external potentiometer controlled pulse width modulated (PWM) signal fed into the Mystery Fire Dragon ESC. This 100-amp rated ESC was chosen because the motor manufacturer specified a maximum current of 65A, although this appears to have been a steady state calculation which may have disregarded transient pulses and peaks. Evidence of this was found during the first test runs for the motor. At the onset of testing the G60, no propeller was mounted primary for safety. During this period, only the slightest changes in throttle were made from one output level to another (5-10% throttle deviations), and the G60 responded with the kind of rapid changes in RPM we would expect from a motor rated at 500KV. Next, we added a hefty and rigid 16x2 APC propeller (Model LP16012) in attempt to begin measuring thrust output levels. The combination of increasing the rotational moment by adding the propeller, while also testing motor response to more drastic throttle deviations (30-40% throttle deviations) somehow resulted in the overheating and eventual combustion of the electronic speed controller. This was the first of what would undoubtedly be many setbacks, disasters, and testing failures throughout the tenure of this work, to be elaborated in the following chapter. The ESC's heat sync shown in Figure 5.6 was a hefty one and functioned suitably in earlier test trials. The meltdown occurred during a rapid transition from a throttle of roughly 60% to over 90% as well. Though the exact current was not being measured at the time, the available data points to a high transient current as the culprit.

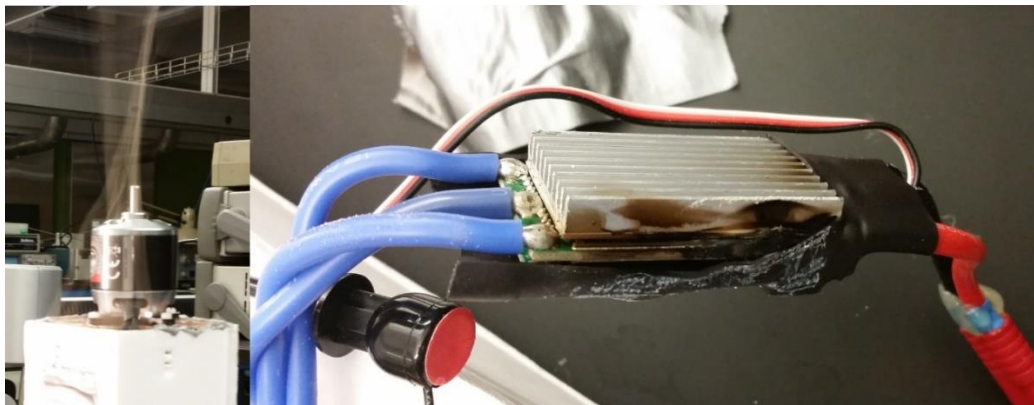


Figure 5.6: Post combustion initial motor testing

Though undesired, the results from testing of the G60 foreshadowed possible dangers of working with such high current loading motors, giving rise to much needed additional research into an alternative brushless DC motor. Indeed, when the X8 octa-quad design of our desired UAV is taken into consideration, we arrive at the frightening conclusion that by virtue of a single G60 pulling 65-100 amps of instantaneous current, our 8-motor design would in turn require a power supply capable of safely delivering 520-800 amps at full speed! A daunting requirement. Though

certainly attainable, for magnetic field suppression and security reasons later expanded on, this was simply unacceptable. The motor explorative research period concluded with a transition from the Turnigy G60 to the premium built, and more expensive T-Motor 5008 340KV.

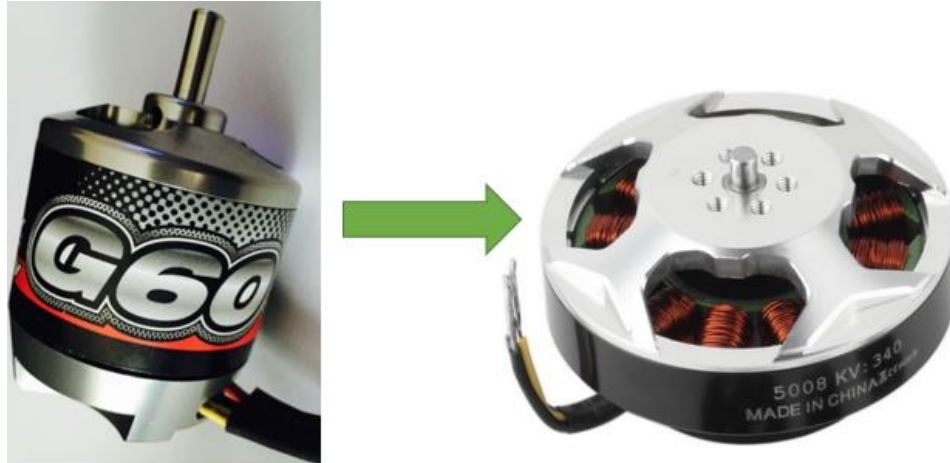


Figure 5.7: On the left: Turnigy G60 Motor | On the Right: T-Motor 5008 340KV

Improved electrical efficiency summarizes the primary reason for this verdict. The flatter profile of the T-motor distributes a greater ratio of motors mass towards its external perimeter than the G60 does. Intuitively, this increases the motors rotational moment and acts to retain more rotational kinetic energy while in operation. The T-Motors maximum current draw is rated at < 22 amps at 3 kg of static thrust. Not only does this mean that our octa-quad design will have a maximum static lifting thrust of 24kg (well above what we desired), but also that the maximum current draw from all 8 motors at full speed is down from 800 amps to 176 amps. In addition to improved efficiency, The T-Motor's manufacturer surprisingly provided detailed motor test results (Figure 5.9), allowing for the streamline derivation of thrust and torque coefficients covered in Chapter 4 (C_T and C_q) seen in figures 5.10 and-5.11 below, which further allowed for subsequent simulations to be more accurate. It's worth noting that we forfeit the freedom to select a propeller, and are forced to employ the same Falcon 1855CF carbon fiber prop which Tarot acquired their motor test data with, in order for this data to directly correlate with our motor setup. With an 85% throttle efficiency of 6.48 grams/watt, the T-Motor 5008 and Falcon 1855CF setup surpasses the G60's, however this motor-propeller setup is far from the most efficient. Many other motor-propeller combinations (also from T-Motor) have max 85% throttle efficiency ratings as high 11.19 grams/watt (T-Motor U12 100KV), while even delivering greater thrust (4kg). However, the 5008 340KV model price point was the best available for the budget of this project, since unit motor cost increased exponentially with a matched increase in efficiency and thrust.

Motor	Propeller	6S	22.2V	Throttle(%)	0	17	34	51	68	85	100
Tator 5008 kv340	Falcon 1855CF			AMP(A)	0	0.7	3.5	10.8	18.7	21	21.3
				Thrust(KG)	0	0.282	0.930	1.990	2.800	3.023	3.066
				Efficiency(G/W)	0.00	18.15	11.97	8.30	6.74	6.48	6.48

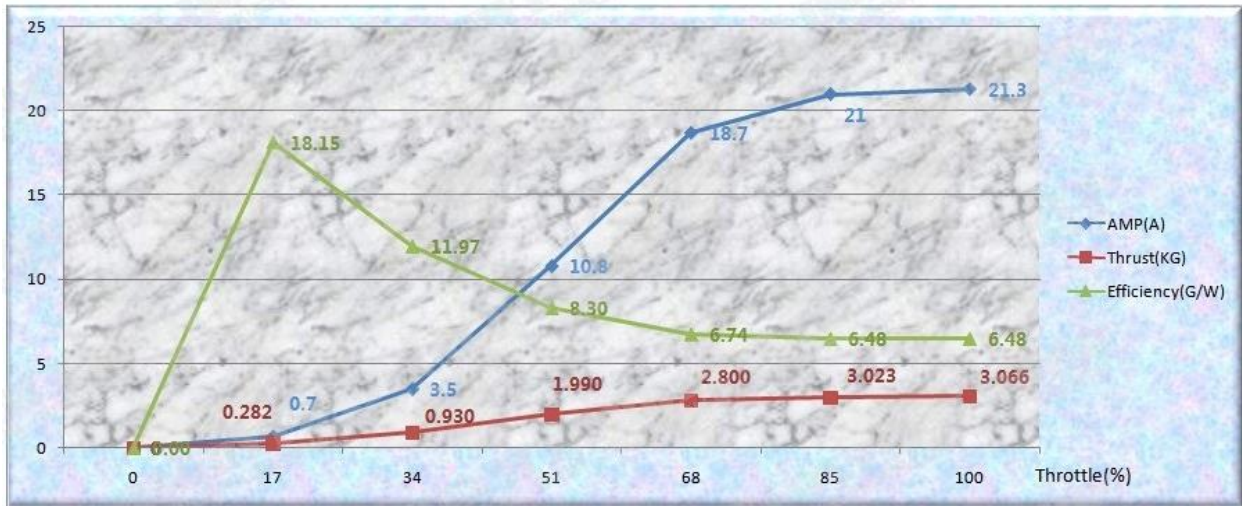


Figure 5.8: Tator 5008KV motor test data as provided by the manufacturer

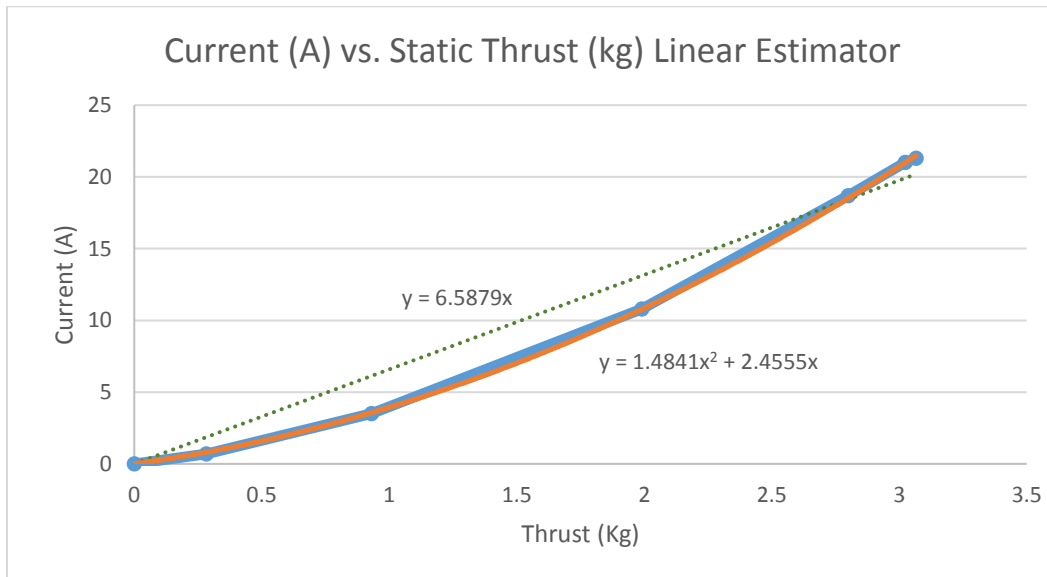


Figure 5.9: T-Motor Current vs. Static Thrust

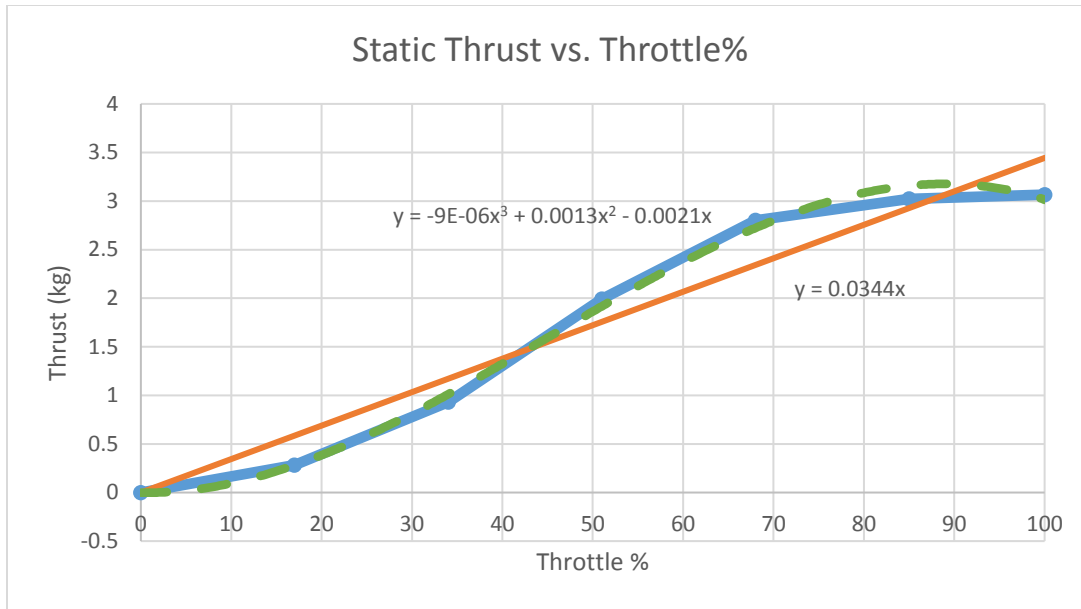


Figure 5.10: T-Motor Static Thrust vs. Throttle %

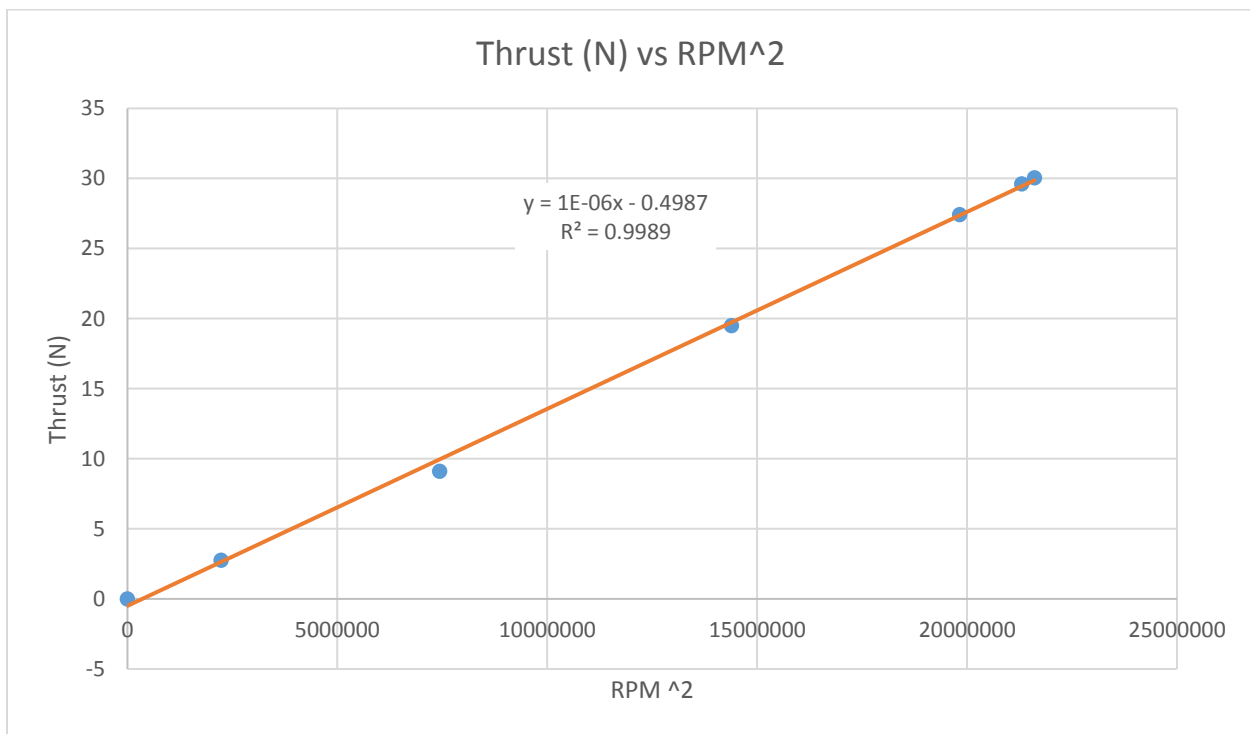


Figure 5.11: T-Motor Thrust vs. RPM²

The above graph gives us a thrust coefficient $C_t = 1.0 \times 10^{-6} \frac{N}{RPM^2}$, given that the propellers has a radius of 0.2286 meters (9 inches), the torque coefficient is now $C_q = 2.28 \times \frac{10^{-7} Nm}{RPM^2}$. Note that since the Simulink simulation is a quadrotor layout, we must double our C_t value in order to

account for the additional motor per arm. With the motor rotating at 4648 RPM while receiving a throttle signal of 100%, throttle the coefficient of rotation $C_r = 46.46\%$.

-Electronic speed controller (ESC)

The combustion of the Mystery Fire Dragon brand ESC prompted the search for an ESC with less mysterious fire, and better performance. In conducting this search the issue of mass also became a critical variable, as we now recognize the inverse relationship between the total (all up) mass of the UAV and its eventual payload capacity. HobbyKing's "red brick" brand of ESC's was eventually settled on due to a 100-amp steady state rating, a 140-amp burst current rating, and their ubiquity within the UAV community. Additionally, these ESC's included a convenient battery eliminator circuit (BEC) capable of supplying 5.5 volts at a maximum of 4 amps. The sizable heatsink on this brand in combination with the reduced current requirements of the T-motor, resulted with infrequent inflammation throughout this work. Indeed, of the multiple Hobbyking ESC's purchased, only one failed due to human error in the lab.

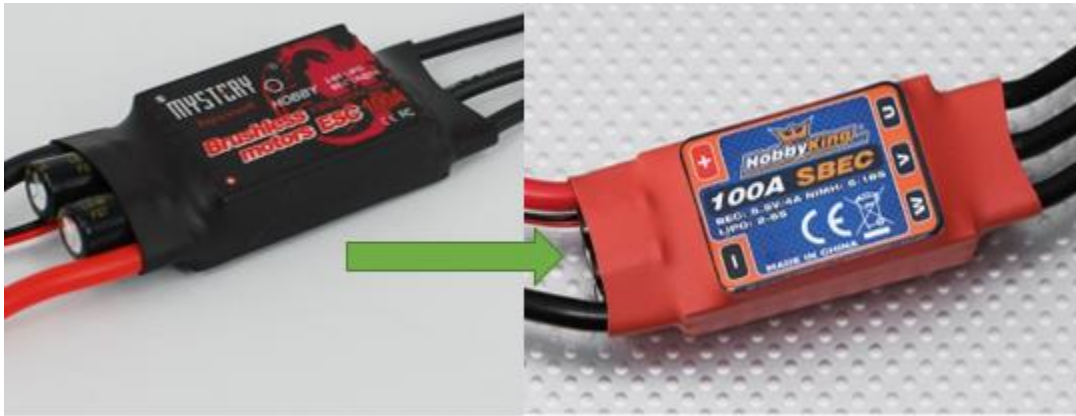


Figure 5.12: Transition from one brand of ESC to another

There are three undesirable aspects found with the HobyKing brand, the first two being it's geomotry and mass. This ESC is bulky to say the least, and is typically used in single motor Hilicopters or 4-motor quadcopter designs. Fitting 8 of them within our X8 octa-quad UAV would prove to be difficult, yet not as difficult as spreading their mass evenly about the UAVs center of gravity. With a unit mass of 99-gram the ESC's would already consume 10% of our 8kg goal. Lastly, the PWM signal required by this ESC wasn't the standard 50-60 Hz, but was instead rated at 8khz or 16khz. Though this does not directly appear to be of concern, it impacts the signal resoltion of the PWM generating microcontroller (discussed later). In general, ESC's controlled by lower frequencies allow a microprocessor to have greater percision of PWM duty cycle, which in turn allows for greater prcision in controlling the individual motor speeds on each arm of the UAV. This last setback would eventually be circumvented by employing powerful microcontrollers.

-Power Supply



Figure 5.13: Chain of Nano-Tech LiPo Batteries being charged

The significant drop in current requirements gained from using the T-Motors instead of the G60's could have been a basis for similarly reducing design requirements for our power supplies current capacity, yet early experiences took this work in the opposite direction. This design feature was one of the earliest to be specified, and thus future planning was considered. At the onset, it was difficult to determine what sort of additional components would be needed to complete our system, and what sort of current demands those components would require. Thus, a maximalist approach was taken to designing the power supply, striving to design one capable of supplying as much current as possible. Figure 5.13 above shows the Turnigy Nano-tech lithium polymer batteries selected. These batteries each holds 5000 mA-Hours of charge, and are capable of safely delivering 125 amps of steady state current and (350 amps of impulse current).

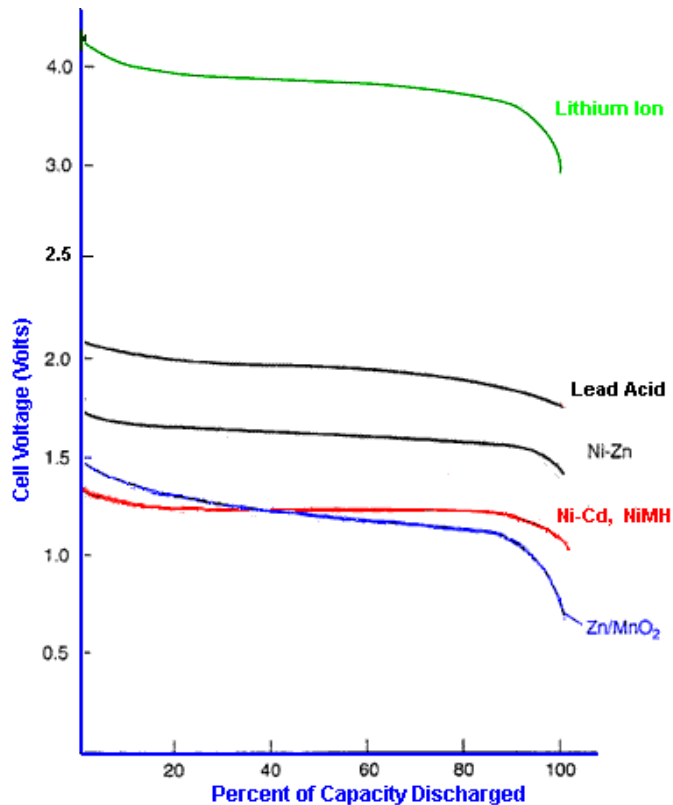


Figure 5.14: Discharge curves for various battery technologies [70]

As previously eluded to, the power density found in lithium ion batteries surpasses that of lead acid and others. Additionally, as seen in figure 5.14, LiPo batteries share the common characteristic of maintaining fairly constant voltage between 20% and 85% discharge levels. However, an unavoidable drawback found in each lithium ion battery reviewed for purchase was their significant mass, with the final selected brand adding 450 grams per six-celled block (totaling ~2kg). A heavily debated design characteristic was the issue of series verses parallel configuration. Most of the alternative work presented in chapter 2 used either a single battery (similar to our Turnigy Nano-tech brand), or paired two batteries in series. This likely resulted from the relatively short flight times (<12 minutes for DJI) and low current demands of their respective designs.

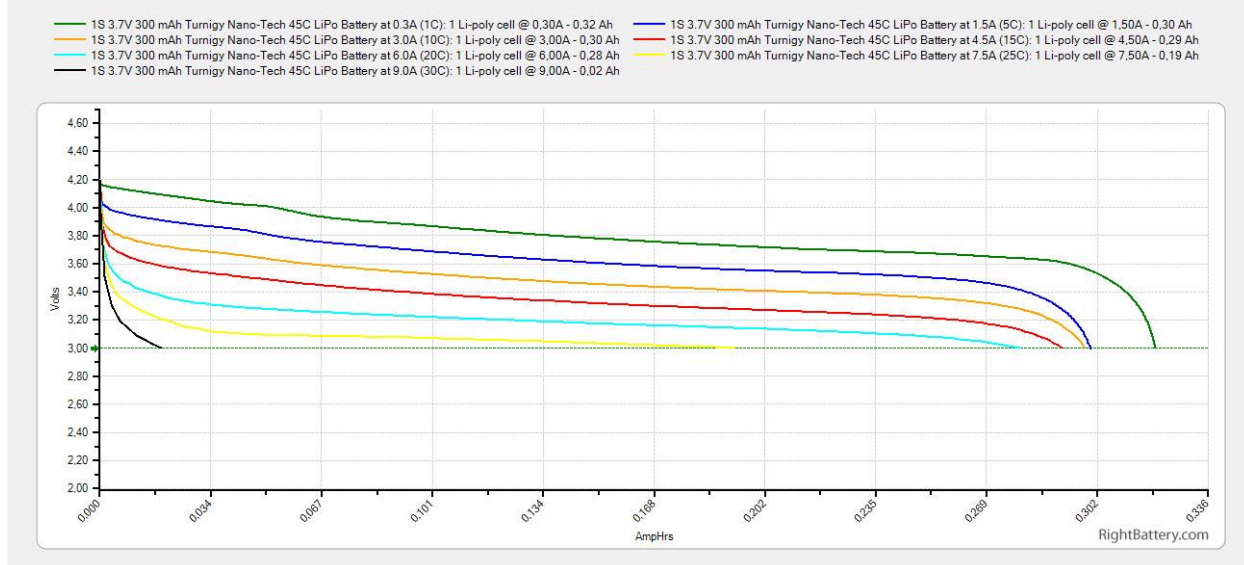


Figure 5.15: Turnigy Nano-Tech LiPo battery discharge tests at various discharge rates [71]

Series combination of two batteries would result in a maximum system voltage of 50.4 Volts, providing both LiPo batteries contained six cells or less. Though this voltage can easily be regulated down to more standard levels (5.5V, 5V, 3.3V....), there is a conversion penalty which usually manifests in the form of hot voltage regulators requiring hefty heat dissipating sinks. To maximize flight time, our design employs four six-celled LiPo batteries, which would result in a combined maximum voltage of 104.8 volts if connected in series. This voltage exceeds the absolute maximum rating of many regulators within our mass specification. Even the switch mode regulators capable of down converting such high voltages would need to be accompanied by sizable heatsinks, further cutting into our 8kg design parameter. The parallel connection of our 4 LiPo batteries clearly became less of a choice and more of a necessity.

Regardless, there is a significant benefit to parallel connection, an *artificial* increase in capacity. When each cell is connected in parallel, the rate of discharge per cell is reduced. Figure 5.15 above shows different discharge curves (different rates) for our Turnigy Nano-tech batteries. Observe that the cell represented by the green uppermost curve is discharged the slowest at 1C, and achieves the highest amp-hour output. Indeed, discharge rate vs capacity has been heavily researched in [67] and elsewhere, supporting the above data. To be clear, the battery capacity is a fixed quantity regardless of discharge rate, which is why the increase is intentionally labeled as *artificial*. The appearance of increased capacity is simply a result of the cells decreased internal impedance when discharging at slower rates, allowing us to safely access more of the cells fixed amp-hour capacity. Additionally, each 6-celled LiPo block has additive current characteristics when wired in parallel, meaning our power supply can safely deliver a steady 500 amps, far exceeding any foreseeable future needs for any added components.

-Electronics

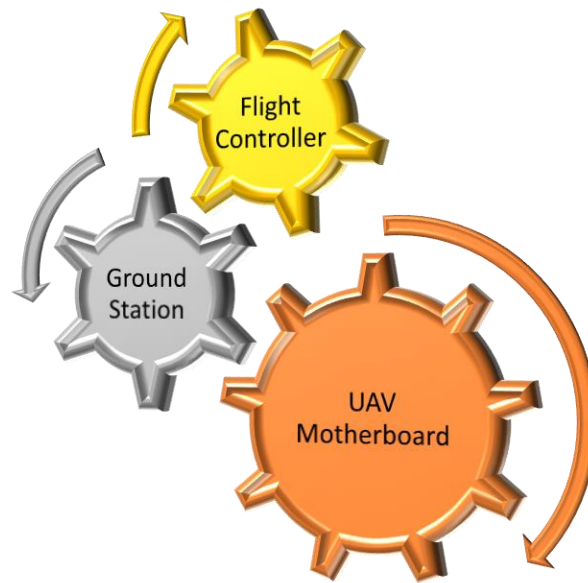


Figure 5.16: Depiction of Design Method

Figure 5.16 is a graphical depiction of the prototyping methodology adopted throughout the UAV design conducted in this work. The onset of this work began with the goal of creating a custom designed UAV entirely from scratch, with the belief that this would create the best testing platform. However, the acquisition of both greater knowledge and humility transitioned the final design methodology to a more hybrid one. The system is designed such that control of the UAV can switch hands, from a 3rd party flight controller, or a custom-built motherboard, or a ground station. The UAVs motherboard will have the highest permissions and will delegate control. The drawbacks of this methodology are increased cost, increased complexity, and the addition of an ownership management scheme. However, this design provides the advantages of increased safety via redundant systems, parallel data comparison capabilities from each system, and the use of a tried and tested platform while simultaneously testing custom features unique to our design.

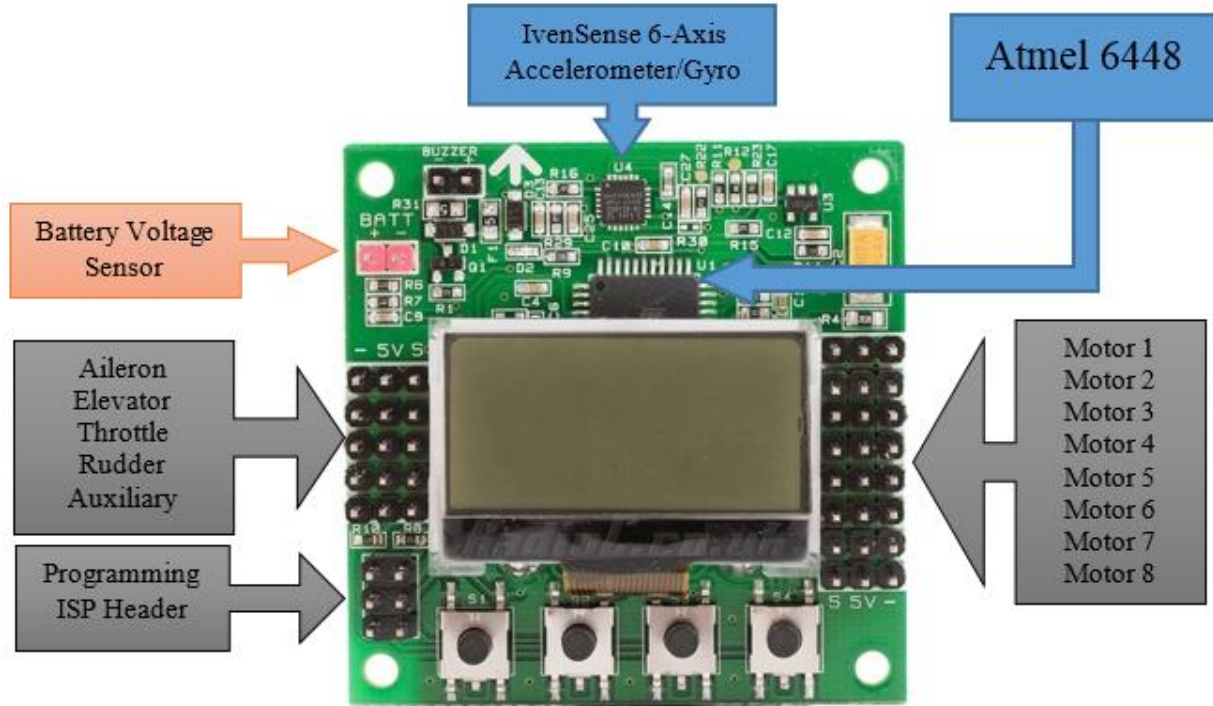


Figure 5.17: KK 2.1 Flight Controller

Powered by a common Atmel 6448 microprocessor, the KK 2.1 flight controller was selected to optimize for cost. Additional features such as an onboard battery voltage sensor and an in-system programming (ISP) header were a bonus. Product reviews reported precision auto-leveling and high resolution yawing angles provided by the IvenSense 6-Axis accelerometer and gyroscope module. This, in combination with the device being capable of managing our X8 octa-quad layout, made it sufficient. Of concern, was the lack of differential control, which raised the question of settling time duration. How responsive would the system be? With only proportional and integral control offered, percent overshoot and settling time might both prove to be high. It's suspected that derivative control was omitted due to the cost involved in removing noise sensitivity in the process signal. The unorthodox weight of our UAV also made setting the proportional and integral gain constants, K_P and K_I , a challenging endeavor.



Figure 5.18: Adafruit Inc. GPS Breakout Board

Our selected flight controller would be enough to simply get our UAV airborne, however, navigation would require location data provided by a global positioning system (GPS). Adafruit Inc.'s GPS (MTK3339) was selected for its user-friendly breakout board. Being such a critical feature, proper operation could not be risked by faulty soldering of a difficult surface mount component, thus a preinstalled package had much appeal. Features of this GPS include a 10 Hz update rate, position accuracy down to 3 meter (universal), 0.1 meters per second velocity accuracy, searching of 66 and tracking of up to 22 satellites including GLONASS (the Russian ones ☺). A backup coin cell battery found below the device allows for faster startups and low powered data logging. The universal asynchronous receiver/transmitter (UART) communication lines on this GPS connect directly to the motherboards central microcontroller (MCU), discussed below. The most important feature of this GPS model is the packet command sets it receives (PMTK commands), allowing the MCU to dynamically dictate the input frequency, and to specify what kind of data is desired (position, date time, velocity). The importance of this feature was made clear when troubleshooting input buffer overflow problems within the main MCU.

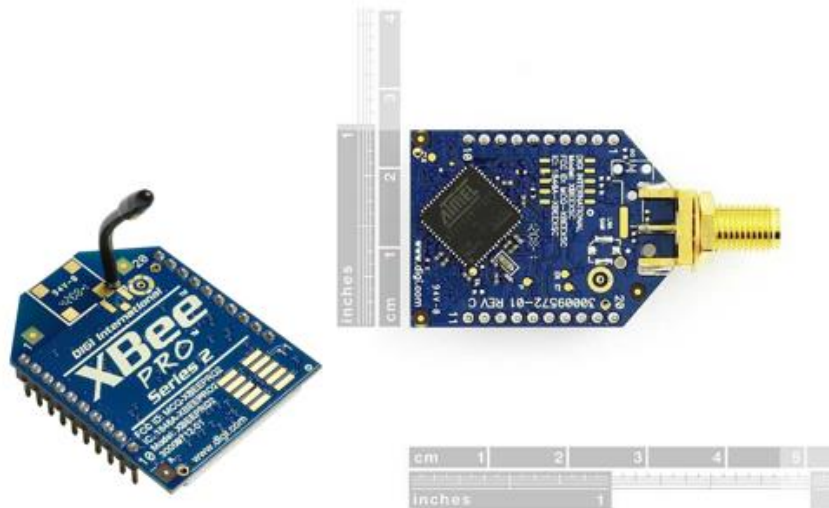


Figure 5.19: Digi International XBee-Pro 2.4GHz modules

V1 uses the XBee-Pro 2.5Ghz modules to establish a communication link between the ground station and the UAV. Specifically, the ground station and the motherboards central MCU both sent and received, location, manual attitude commands, and other custom commands through wireless communication. This models was chosen as a balance between cost and power, landing at 63mW (+18dBm) for roughly \$50. At this transmitting power, outdoor communication just under two miles could be achieved, per the product specifications. As discussed further, this range was never fully test or verified. The software provided by Digi International which accompanied these modules (XCTU) was useful in selecting unique channels when interference became a concern. Similar to the GPS, the serial data interface UART option, along with a through-hole compatible breakout board increased the modules appeal. Additionally, the famed robustness of XBee modules was further strengthened throughout this project. The initial

purchased units were still fully functional at the time of the completion of this work. As the reader continues onto chapter 6 they will hopefully gain an understanding as to why this is truly amazing.

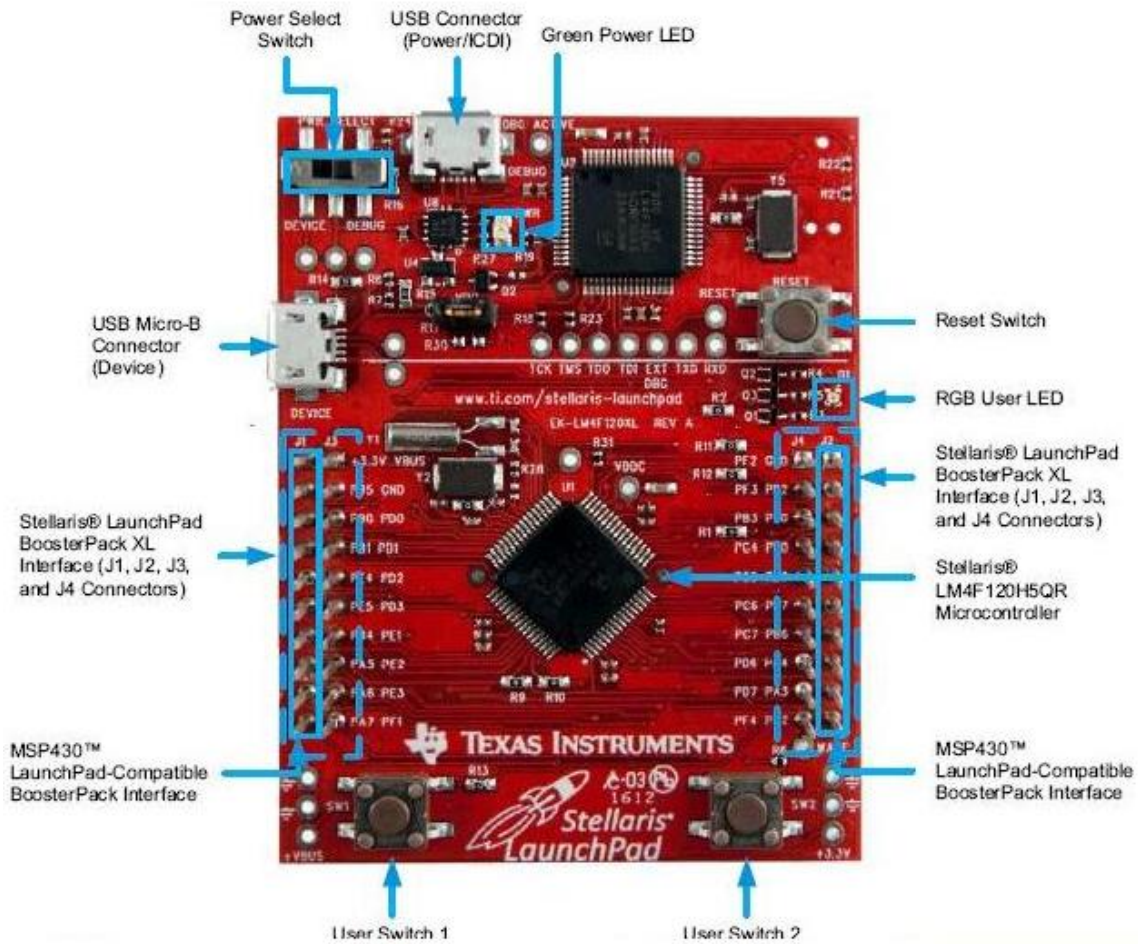


Figure 5.20: Texas Instruments Stellaris Launchpad

Texas Instruments LM4F120H5QR MCU is part of a broader family of 32 and 64-bit processors based on the reduced instruction set computer (RISC) architecture developed by Advanced RISC Machines (ARM), and acted as the UAVs central MCU. The ARM architecture is presently the most widely used instruction set architecture with tens of billion manufactured as of 2016. The modified Harvard architecture of AVR MCU's, though more readily compatible for UAV development (as seen by the KK 2.1), lacked the enhanced power-saving design and hardware visualization support found within the ARM architecture. Programming of the MCU occurred within the IAR embedded workbench development environment. This workbench was excellent for code generation, organization, troubleshooting, and in system programming. Atop the aforementioned reasons the TI- LM4F120H5QR was selected is the availability of low-priced TI-Stellaris Launchpad development boards, displayed in Figure 5.20 above, which conveniently

house the central MCU. The development board includes multiple switches, many pre-soldered multi-purpose pins, and a programmable RGB LED. In addition, the Stellaris in-circuit debug interface included in the top section of development board, also powered by a separate TI-LM4F120H5QR, proved to be priceless.

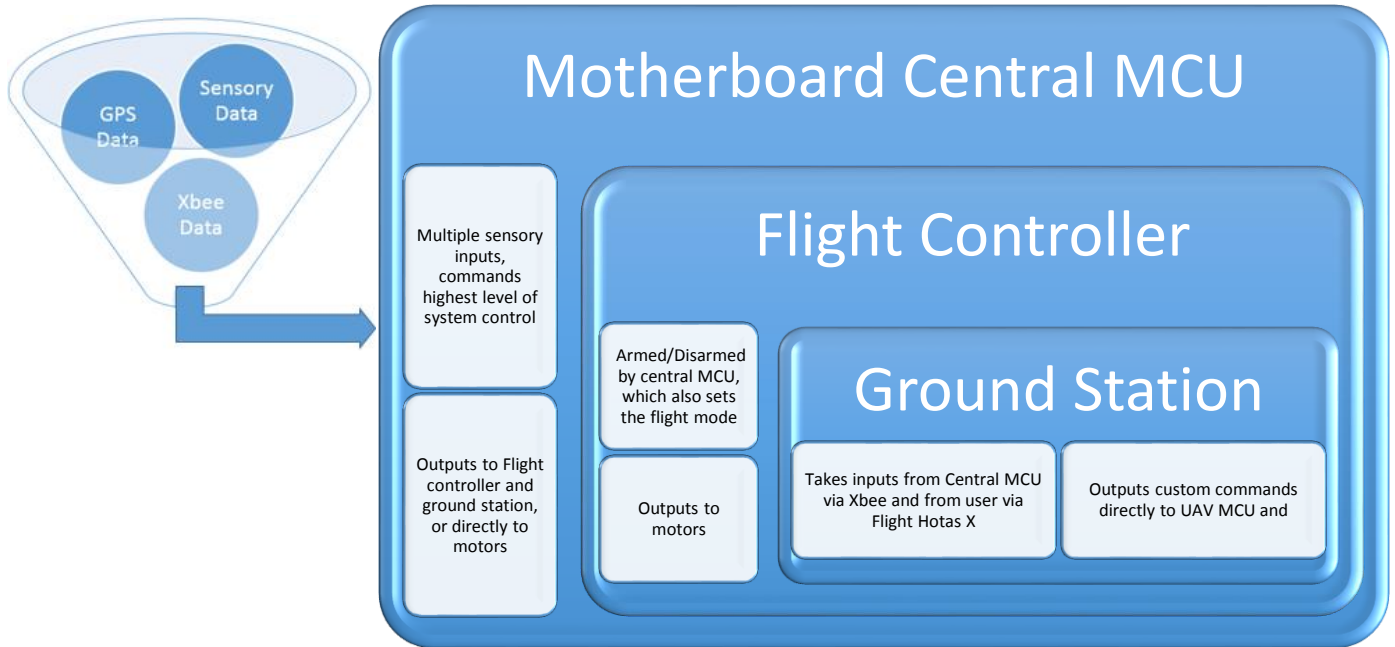


Figure 5.21: Visualization of UAV ownership protocol

Top level system control transpires within the motherboards central MCU, this required a strict ownership protocol to be programmed into the embedded system. Although the KK 2.1 acquires linear and angular acceleration data from its onboard IvenSense chip, the flight controller provides no means of real time communication towards extracting such data. Thus, the TI-Boost XL expansion pack was added to the overall design, and is attached to the Stellaris Launchpad development kit to compensate for the KK 2.1's communication shortcomings. The central MCU's UAV attitude data was derived from the Boost XL Senshub's 9 axis motion sensor (MPU9150), however the two-wire serial interface (I^2C) employed allowed data from the Senshub's various sensors including, pressure (BMP160), humidity (SHT21), temperature (TMP006), and light (ISL29023) sensing modules seen in Figure 5.22 below. Many of these peripheral sensors may not have an immediate application to this work, but were certainly be considered in applications for future work on this platform.

By now the reader may have recognized the immense redundancy purposely built into our design. Attitude control, for example, can be directed by the ground station, central MCU, or the flight controller. Also, spatial orientation in the reference frame is acquired from both the flight controller and the Senshub, while being displayed within the ground station interface. Even the UAVs temperature is acquired four different ways, Twice within the KK 2.1 and the Senshub, twice on Stellaris Launchpad's internal and external sensors. The intention was to leverage the cost of powering these redundant modules for gains in UAV security and overall reliability. This is most exemplified by the redundant analog to digital converters which read the voltage levels

of the power supply. The central MCU was programmed such that a low voltage alert from either internal or external (KK 2.1) battery capacity indications would result in an alert to the ground station at a marginally critical capacity level, and a force land at a more critical level. In general, V1 was designed to require both the KK 2.1 and the central MSU to constantly be in desirable states for the UAV to remain unalarmed, otherwise the use of user alerts, and/or autonomously programmed safety directives would take place.

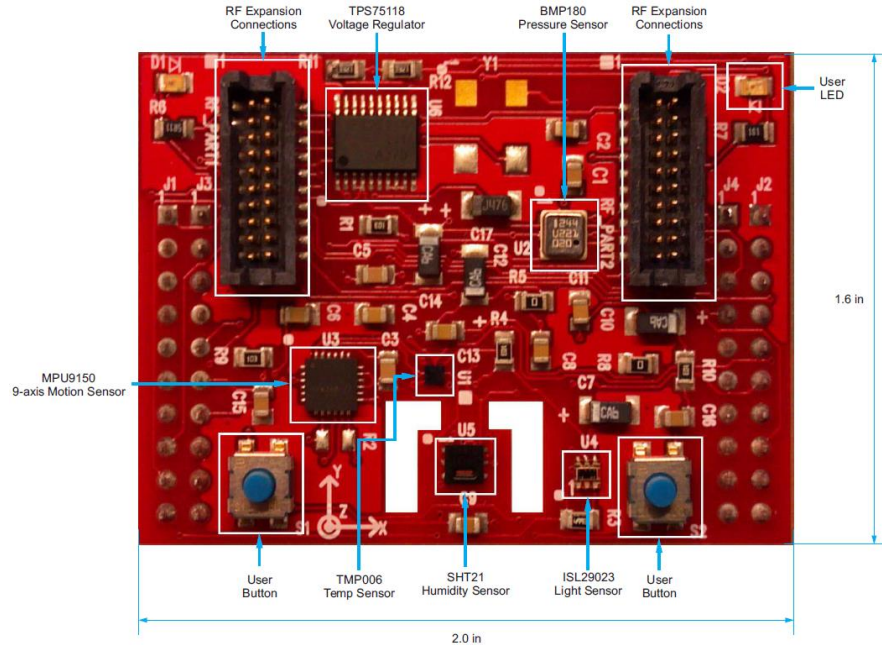


Figure 5.22: Texas Instruments Boost XL SensHub for Stellaris Launchpad

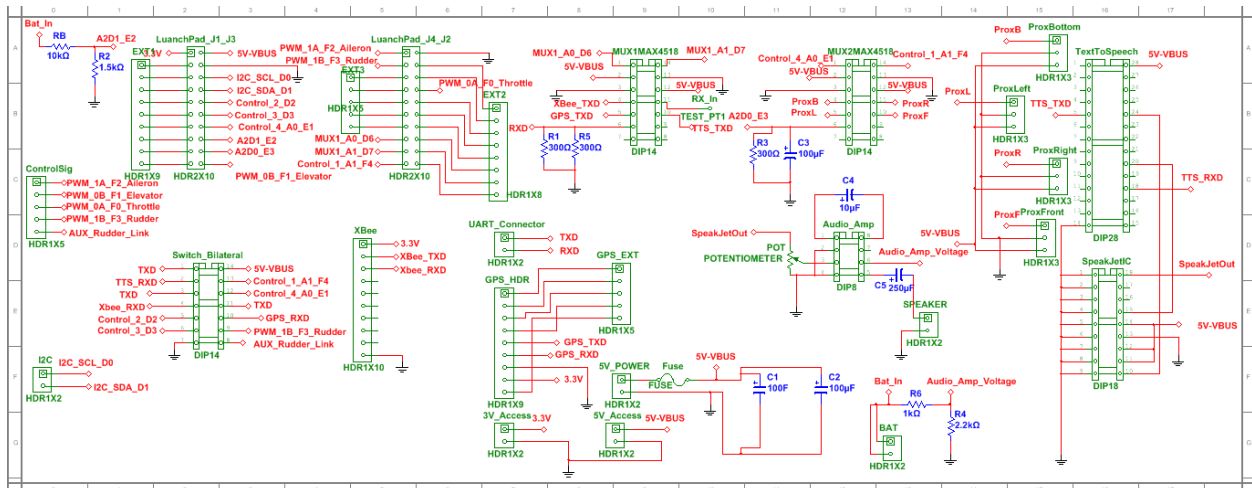


Figure 6.23: Motherboard Circuit design via National instruments Multisim & Ultiboard Suits

The schematic and printed circuit board (PCB) for the motherboard (Figures 5.24) is the result of an effort to join all aforementioned electronics onto a single platform. Both were designed using National Instruments circuit design suite (Multisim & Ultiboard 12.0). The schematic's basic design drew influence from components with standardized footprints. The most difficult component being the Launchpad itself, since this footprint was a TI custom one, and proved difficult to replicate exactly. PCB dimension were limited by the available space within the UAV's internal cavity, in addition to the absolute requirements of both the flight controller and Senshub to be positioned in the center of the UAV in order to achieve stable flight. Some components not yet discussed yet included in the final schematic are the Speakjet text to speech IC®, and the bilateral switch. The Speakjet IC was originally intended to serve as an alert mechanism while in the field, but quickly proved ineffective under the noise generated by fast turning propellers. The bilateral switch is discussed in detail later. Notable is the exclusion of a fuse, initially intended to be part of the design. This resulted from the assessment that a current overage event should NOT be handled by total system shutdown when avoidable, which would certainly result in a disastrous crash if the UAV is mid-flight. Instead, thorough design rules and real time voltage monitoring (internal to TI's Launchpad) was employed to programmatically react to instantaneous spikes in current. The fuse was shorted with a wire and the practice of excluding fuses from our design continued onto version 2 (V2) as well.

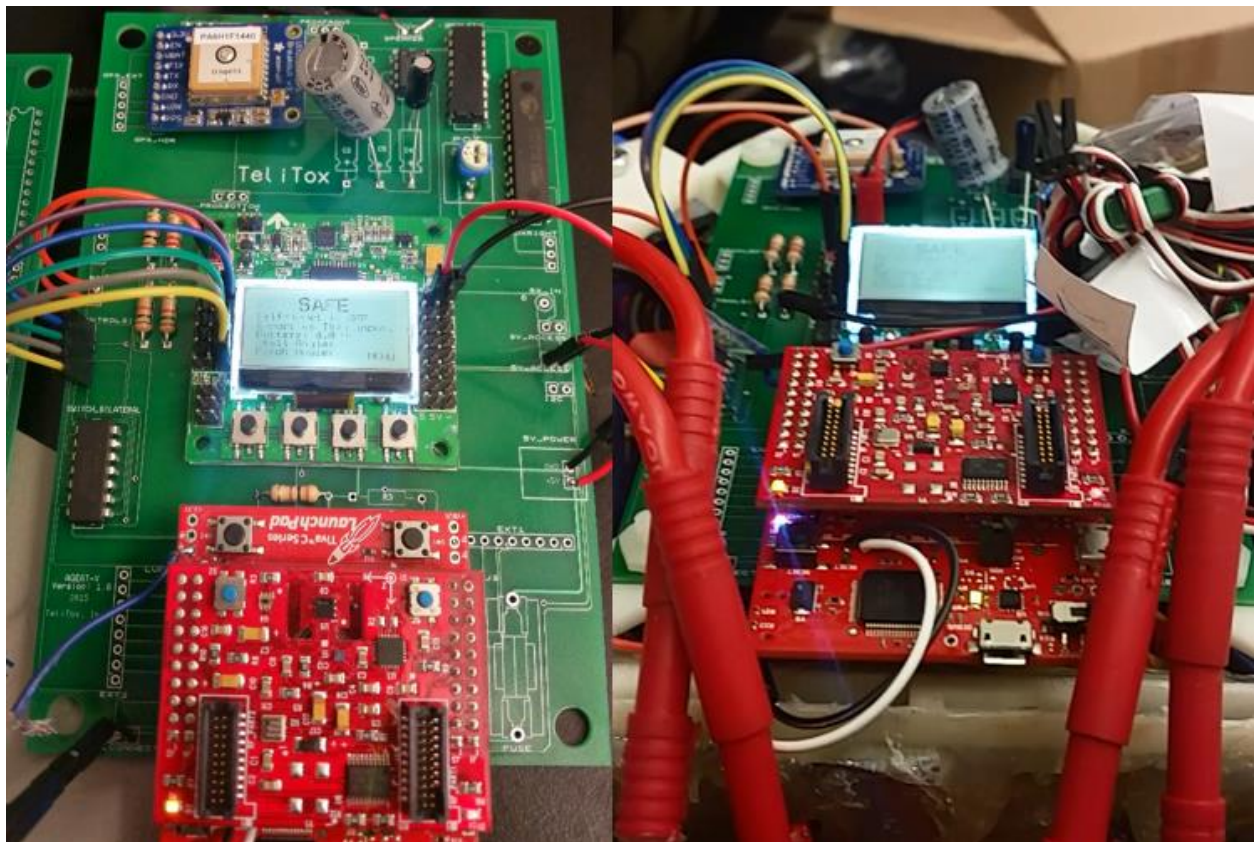


Figure 5.24: V1, fully populated Motherboard

-Ground Station

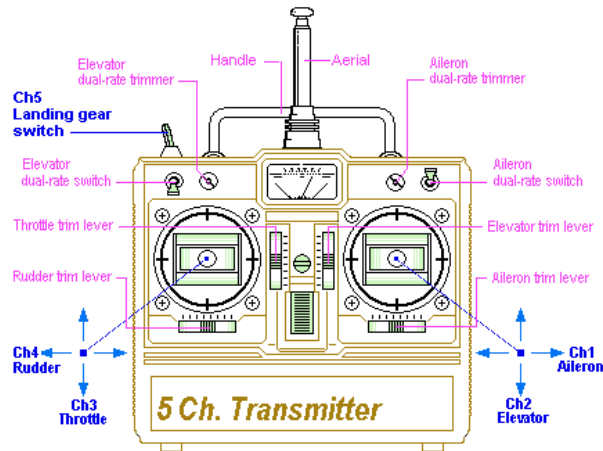


Figure 5.25: Typical 5 Channel UAV Transmitter

Five channel transmitters similar to the one depicted in figure 5.25 above are a staple for quadrotor UAVs. Many are used in some reviewed previous work as well as in the RC hobbyist community. Their design allows for easy mechanical control of four throttle, aileron, elevator, and rudder channels, with a fifth channel reserved for toggling a custom option (mode select, landing gear...). Unfortunately, these off the shelf brand transmitters would not suffice to achieve our desired objectives. The most problematic aspect being the strict limitation of communication channels imposed by available models. Considering the number of customized commands and the amount data (for analysis) required to be transferred between UAV and ground station, the typical five channels store-bought transmitter was practically useless. Additionally, pairing an off-the-shelf transmitter to our unorthodox customized UAV would prove very challenging and overall disadvantageous. However, designing a fully functional transmitter from scratch is an equally problematic project in its own, well beyond the scope of this work. An intermediate approach utilizing both purchasable components and a customizable communication scheme was required.

T.Flight Hotas X

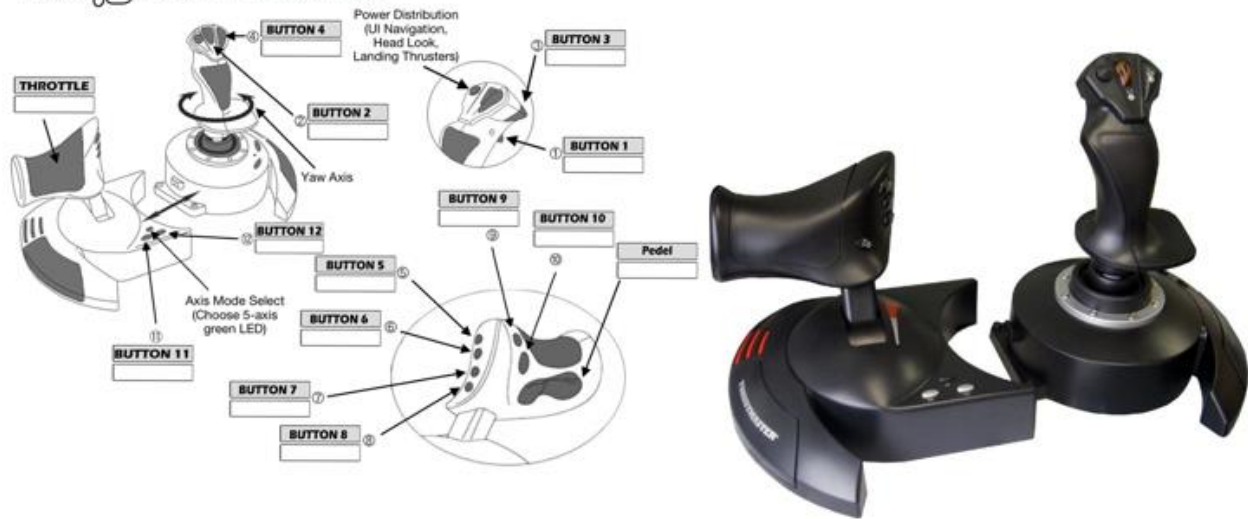


Figure 5.26: Thrustmaster Flight Hotas X Joystick

Having already purchased the XBee Pro 2.4Ghz communication modules as a communication medium between the ground station and the UAVs central MCU, it seemed only natural to port attitude commands through these modules as well. The challenge here was the topic of USB communication (COM) port ownership. The ground station was designed with NI LabVIEW 2013 (Student Edition), an international platform for quick prototyping and system testing. When one end of the XBee link is connected to the computer acting as our ground station, it's made accessible via a single USB COM port, accessed solely by LabVIEW's runtime environment while the ground station is running. Meaning any attitude commands sent via the XBee link must also be sent via LabVIEW. The Flight Hotas X joystick was purchased for its multiple inputs and LabVIEW compatibility. As seen in Figure 5.26 in stark contrast from Figure 5.25, the Flight Hotas X has far more input options and is more open for customization. The interpretation of many inputs on the flight Hotas X changed numerous times during this work, most especially when transitioning to V2.

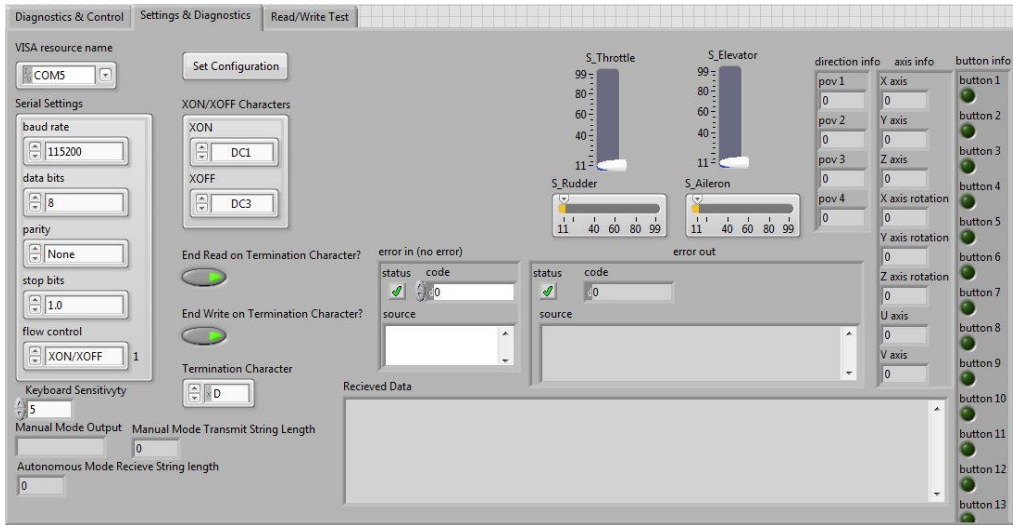


Figure 5.27: Ground Station settings page



Figure 5.28: Ground Station Diagnostics and Control Page

-3D Modeling and Printing

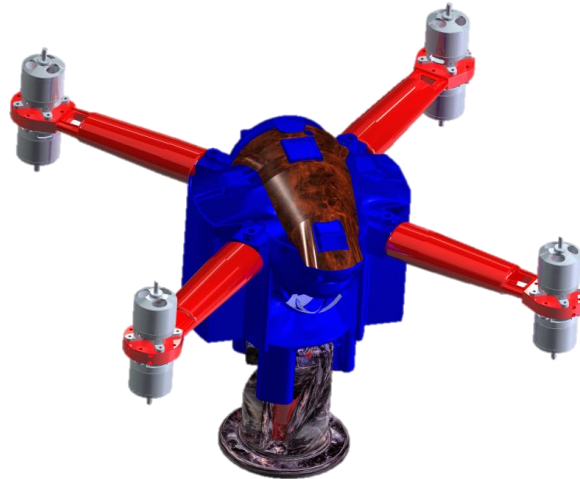


Figure 5.29: UAV Prototype V1

PTC Creo Parametric 2.0 was the sole 3D CAD software employed for modeling of V1 and V2 prototypes. Though on the verge of being out of the scope of this project it was determined acquiring 3D modeling skills would be too paramount a task to set aside, regardless of the steep learning curve. This choice, made at the inception of this work, has proved beneficial beyond any doubt, and will continue to aid in future work. The original physical design was geared towards meeting three basic criteria:

- Attaining a structurally sound Octa-Quad UAV structure
- Housing of all electronics safely from the outside environment
- An evenly distributed center of mass, and external dissipation of heat from ESC's

Supplementary features of the design include a bottom container rotational mating arm, ground supports, and a rear slide-on slide-off toggle. All criteria were attained with varying levels of accuracy. However, the On-Off toggling switch feature encountered challenges (See chapter 7).

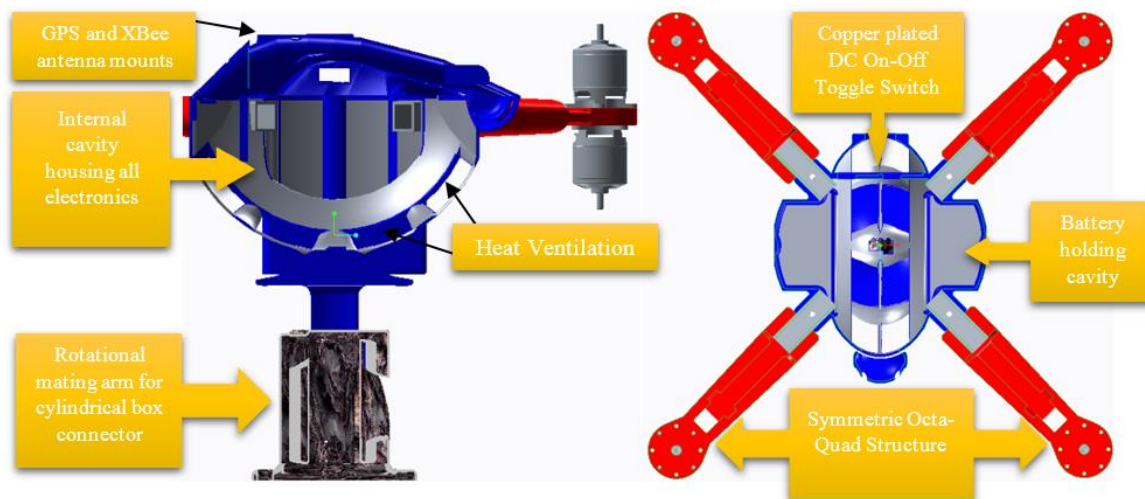


Figure 5.30: Cross sectional side and top views of UAV prototype V1



Figure 5.31: Stratasys® Dimensions 1200es (left) and Fortus 250mc (Right)

Once the 3D modeling is completed and tested, 3D printing can begin. Fuse deposition modeling technology (FDM), thermal practice parts via file pre-processing, part production and support removal. Dimensions 1200es and Fortus 250mc high resolution 3D printers were used to manufacture the majority of parts printed for this work. Stratasys' Insight preprocessing software was used for developing build parameters that determine the look, strength, and precision of parts post 3D modeling. The printing process involves thermoplastic filament being fed into an extrusion header in a liquefied state, and depositing it in a precise tool path to create the shape of each layer of the desired object, one layer at a time. These specific dual extrusion systems utilize both acrylonitrile butadiene styrene (ABS plus) for the build material and soluble support material to build parts from the bottom up. The dark brown soluble support structures in figure 5.32 below are used to uphold overhangs, and are eventually dissolved away in a chemical bath which is neutral to the ABS plus modeling material, leaving only the desired part. This method allowed for printing of more advanced parts, with a consistently clean finish.



Figure 5.32: Left: Freshly printed part | Right: Heated chemical bath to remove soluble support structures

V1 of our UAV prototype is seen in figure 5.33. The final weight, just under 10kg, was 2kg higher than our objective, but was not disqualifying as it simply cuts into the payload capacity. This increase in mass was due to excessive thickness in UAV body, intended to improve its structural integrity. Some nonprinted components such as copper plates, screws, nuts, bolts, fabric, and hot glue also contributed to higher than expected mass. The arm end to end length was 685.8 mm across, with a height of 412mm (without antennas).



Figure 5.33: UAV Prototype V1 in the field and on display

5.3 Version 2

Results from tests flights of V1 gave awareness to many issues elaborated on in Chapter 6. V2 of our UAV design came about due to the inability to further modify V1 post testing. What has remained constant in both versions are the motor-propeller system, design methodology, and the weight. V1 was a success in most aspects, making the initial singular enhancement goal for V2 focused at improving structural integrity of the very critically defective motor arms. However, as the new design took root, additional opportunities for enhancement became emergent. Though certainly more expensive, the result became a vastly superior UAV, drawing from both experiences gained while developing V1, as well as the addition of several powerful and advanced components.

-Electronics

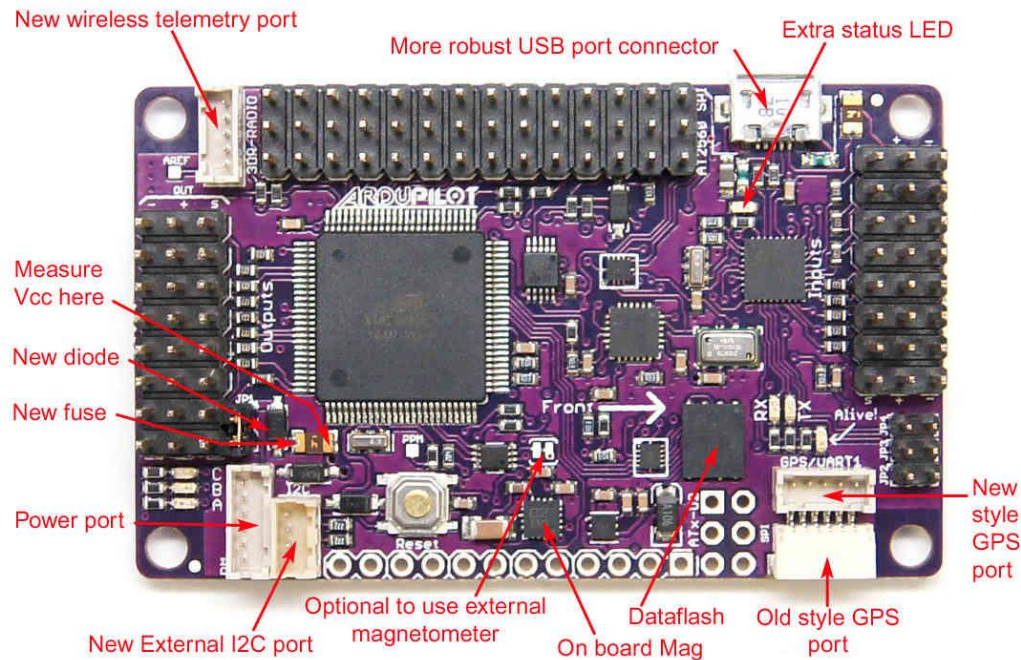


Figure 5.34: ArduPilotMega 2.8 Flight Controller [68]

In designing V2, the KK 2.1 flight controller truly illustrated the definition of “getting what you pay for” and was immediately thrown out with the bathwater. ArduPilot’s ArduPilotMega (APM) 2.X series flight controllers are a complete open-source autopilot solution for multi-rotors vehicles, offering enhanced remote control flight in numerous intelligent flight modes and execution of autonomous missions. APM 2.X is no doubt on the cutting edge of aerial robotics, benefiting from a larger family of ArduPilot software platforms such as Mission Planner. As seen in Figure 5.34 APM adds two-way radio telemetry, external GPS, and data flash logging options not found in the KK 2.1. APM’s open source nature and excellent online documentation has simplified the process of integrating with the central MCU. Mission Planner would also prove to effectively work in parallel with the custom LabVIEW ground station created during V2. Addition diagnostic tools found in Mission Planner would prove very useful in troubleshooting test flights. Most notable was the real-time logging feature Mission Planner provided. The custom LabVIEW ground station’s data was sampled at a lower rate (2-4 Hz), and received only kinematic and GPS data from the central MCU. Mission Planner allowed for greater sampling frequency (~10 Hz) of a wider range of variables. Signal strength was one variable in particular that remained blind to us during test flights of V1, now made available through a received signal strength indicator (RSSI) variable tracked in mission planner. In truth, each and every in-lab or in-field UAV test conducted while using the APM 2.6 automatically logs over 50 variables, storing them on the local PC for later review, a simply priceless feature. Though not initially intended, the adoption of an APM platform was easily one of wisest decision made in developing V2.

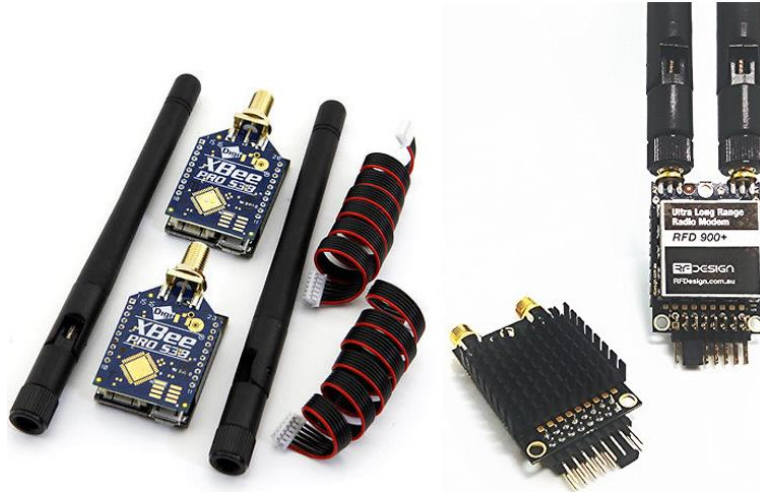


Figure 5.35: Left: XBee PRO 900HP S3B RPSMA 250mW, Right: 3DR's RFD 900+MHz 1MW Ultra Long Range Radio

Upon properly timing the transmission and reception data between the central MCU and LabVIEW ground station, the 2.4Ghz XBee pro modules functioned perfectly in V1. However, adoption of the APM platform, now capable of performing long range missions, as well as a minor upgrade from 5 Amp-Hour LiPo batteries to 6 Amp-Hour ones, gave rise to the desire to be able to communicate along further distances. Additionally, the APM flight controller would need its own telemetry communication channel. The XBee PRO 900HP and RFD 900+ modules were eventually selected, as their price and range were found to be appropriate. The PRO 900HP has a range of 14 km when transmitting at 10 Kbps and replaced the 2.4Ghz XBee modules for communication between the ground station and central MCU. Mission planner to APM telemetry is conducted through the RFD 900+ modules, which have a range over > 40km at the same bit rate, however consuming four times the power as the PRO 900HP modules. The longer-range channel was placed between mission planner and the APM for two reasons. The first is very practical in that the user will never need to manually operate UAV at a distance further than 9 miles, indeed the UAV would appear to be little more than a barely visible spec in the distance. Secondly, return to launch and other failsafe features managed by Mission Planner could (and have) benefit from a 40km range, especially in the event of a flyaway.



Figure 5.36: ESC's used in V2

A drop from 100 to 40-Amp ESC's was made possible by the efficiency of the T-Motors lead to a far lighter cheaper, and even smaller replacement for the Hobbyking Red Brick ESC's. These ESC's weigh in at 22.7g, and were dimensioned so small (60x17x7.2 mm) they could fit inside a 22mm tube. Additionally, the signal frequency was the desired standardized at 50Hz- 60Hz.

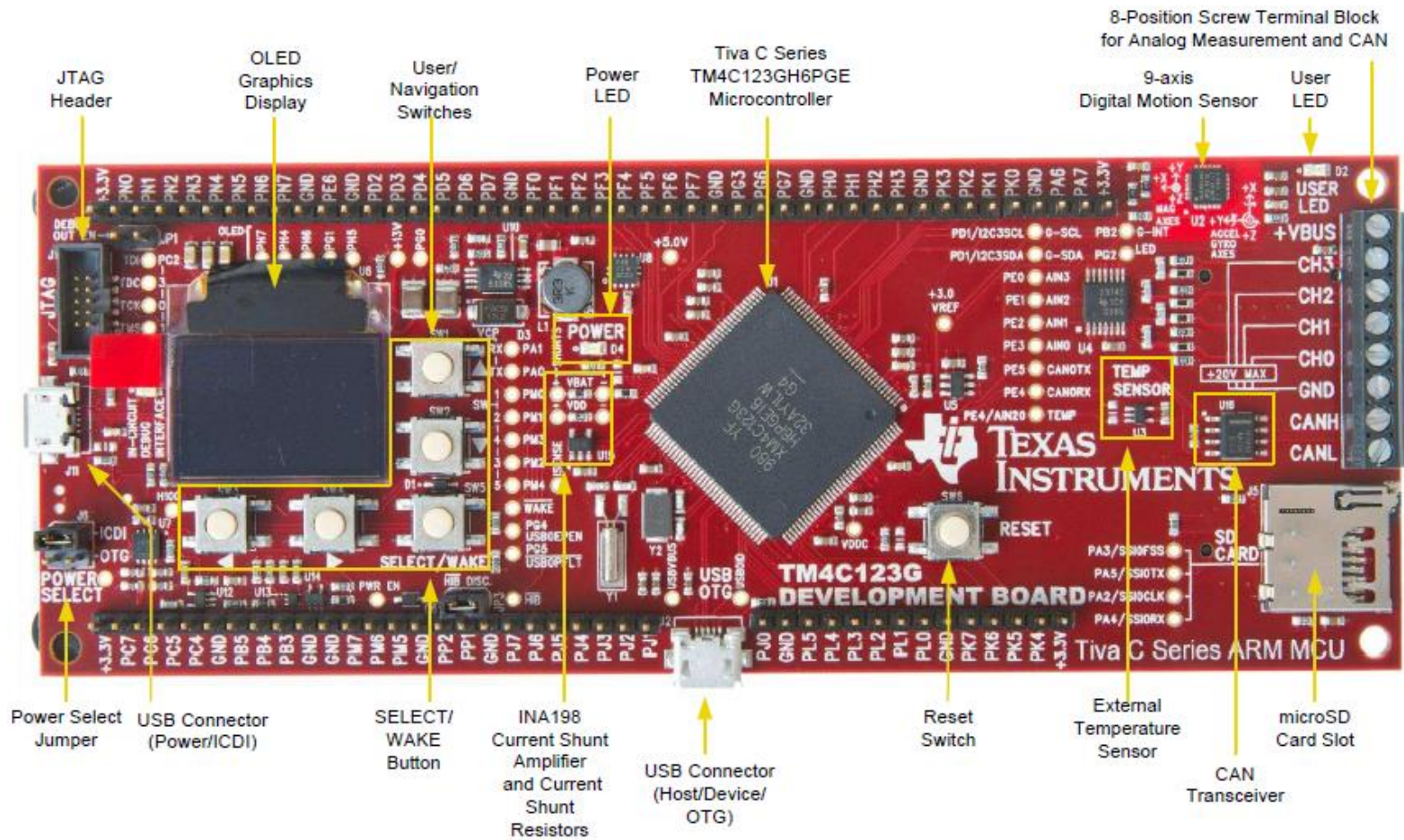


Figure 5.37: Texas instruments DK-TM4C123G

Paralleling the transition from the KK 2.1 to the APM platform in terms of both cost and capability, was the transition from the TI's Stellaris Launchpad to the DK-TM4123G development board. Not only does the DK-TM4123G combine elements of the Launchpad and Boost XL Senshub onto a single board, but also includes: An improved 9-axis motion sensor, 4 analog inputs (0-20V), a microSD card, improved internal and external temperature sensors, user navigation buttons, a 96 x64 color OLED display, precision 3.0 V reference, a coin cell backup battery for hibernation, over double the number of programmable pinouts, a detailed function library, and most notably the Tiva™ TM4C123GH6PM microcontroller with a 32-bit ARM Cortex-M4F Core Processor. The loss of the

SensHub's pressure and humidity sensors was offset by peripheral components included in the V2's full schematic found in the appendix. Virtually every feature of this new central MCU was exploited in the new design at some capacity.

The TM4C123GH6PM's 12 general-purpose timer modules (GPTM) would each be used in PWM mode to control the 8 Electronic speed controllers, in addition to the throttle, aileron, rudder, and elevator control inputs of the APM. Multiplexing schemes would be employed to allow for flight mode selection and various servo motor controls (for landing gear and other items). The significance of this new capability should not be underestimated, as it meant that this new powerful central MCU can now act as a flight controller on its own, a feat unattainable by the Launchpad. Thus, the APM flight controller (still controlled by the central MCU) could be used to assist flight, or in comparing and contrasting the performance of our custom PID control on the exact same system.

Features such as the OLED display, though not critical, allowed for greater ease in both development and troubleshooting. Multiple analog to digital converters allow for more than just checking the battery voltage. As stated earlier, our design strictly excludes the use of fuses, and relies on system processes to track irregularities. The central MCU now monitors the voltage levels of the communication module, and APM flight controller to ensure proper operation. Additionally, among the many failsafe precautions already provided by the APM flight controller, a bilateral failsafe also exists between the central MCU and the APM flight controller. For the UAV to function, the APM requires a normally high IO signal from the central MCU to remain low, if this pin should go high it will trigger something similar to a battery failsafe on the APM, forcing the APM to take control of the motors and land. Similarly, if the central MCU reads a low voltage from the APM in a state where it has given APM control of the UAV, it will immediately reclaim control. Essentially, the APM and central MCU would have to fail simultaneously in order for the UAV to be completely lost, a possible but less likely occurrence, thus improving overall safety.

Carbon Fiber Frame



Figure 5.38: Tarot X4 Frame

The structural problems which plagued the motor mounts of V1 were in dire need of a solution. Following recursive model designs, the ABS plus material used in printing custom parts was deemed too weak, requiring thickened and thus heavier layers to remain structurally sound during flight. The modulus of elasticity (Young's Modulus) for ABS plastic is on the order of $1.4 \times 10^9 \text{ N/m}^2$ to $3.1 \times 10^9 \text{ N/m}^2$ (GPa), making it several times more susceptible to motor generated micro vibrations than other metals ($\sim 207 \text{ MPa}$). In deliberation, we experience a dichotomy between being able to customize the design to meet our specific objectives, and creating a UAV with sound structural integrity. The solution: A hybrid design utilizing the Tarot X4 carbon fiber frame as a skeleton for which we may attach customize printed parts onto.

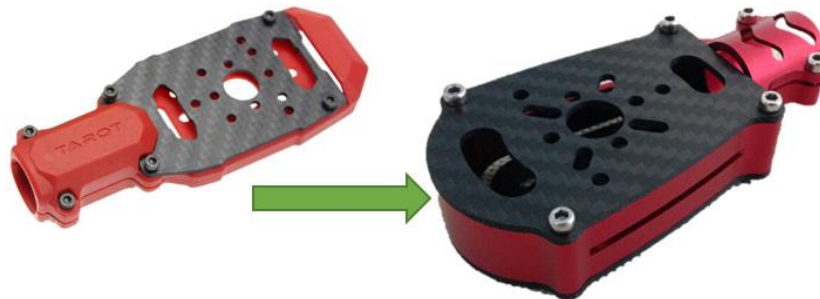


Figure 5.39: Left: plastic Tarot motor mounts | Right: Generic aluminum motor mount

Tarot's frames are widely known in the field of profession photography, as they provide rigid frames capable of carrying the relatively heavy payloads of high end cameras. The carbon fiber material used in each frame has the distinct characteristic of being strong yet light weight. Though made for lifting heavier payloads, these frames were certainly not designed to support a over 8kg, as is evident by the single sided plastic motor mount. These motors mounts were proven to break under loads as heavy as 10kg-12kg and were immediately replaced with dual

sided aluminum ones. Though quite expensive (~\$450 in total), features such as retractable arms and landing gear were a welcome addition.

-Modular 3D Design

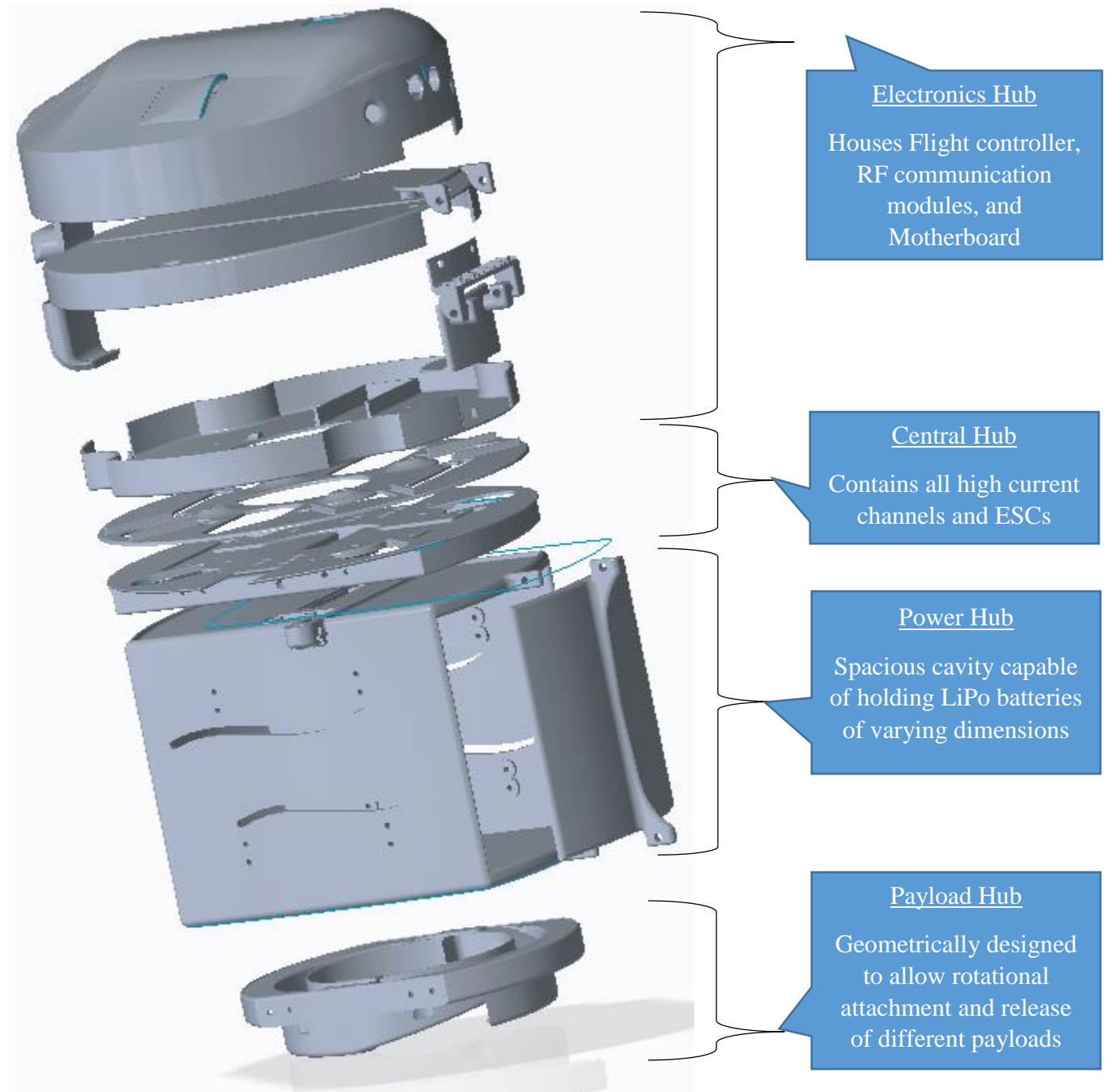


Figure 5.40: V2 modules separated by function

V1's design was centered around a singular core part as depicted in Figure 5.40 above, which was necessitated by the need for rigidity. In that phase, the idea of connecting multiple parts

together was viewed to likely only weaken the UAVs overall rigidity and add unwanted vibrations. With the adoption of the Tarot X4 skeletal frame this concern could be largely disregarded, making way for more modular design. Developing V2 in sections as depicted in Figure 5.40 above streamlined the design process, and made completing any repairs a timely and less costly affair.

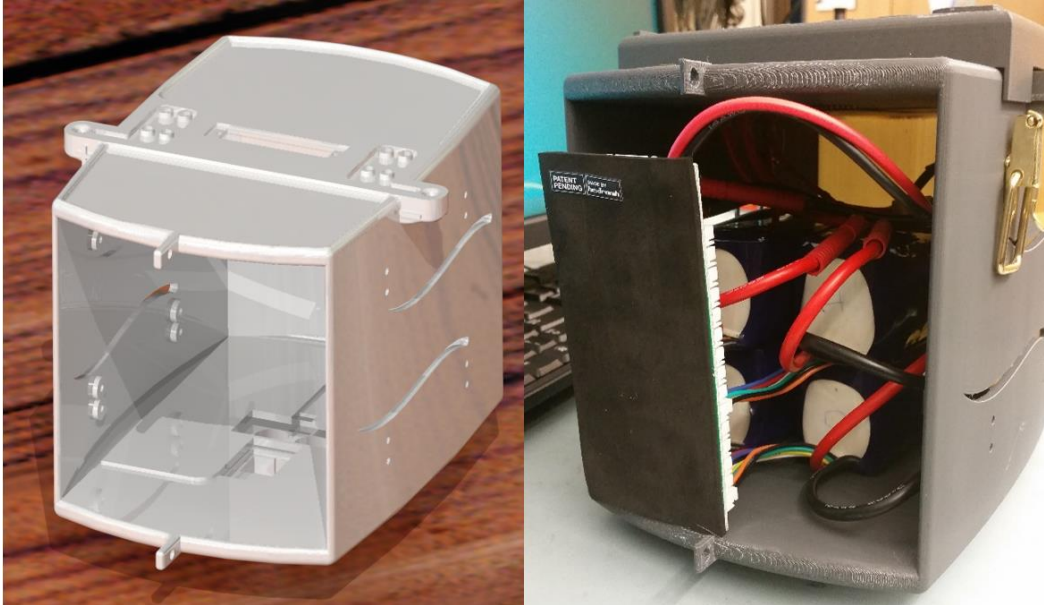


Figure 5.41: Power Hub Simulation (left) and photograph (right)

Working somewhat from the bottom up, the power hub was the first section to be designed. The goal here was simple, maximize for space. UAV flight time being directly proportional to the combined maximum Amp-Hour capacity of the carried LiPo batteries, which in turn is also directly proportional to the amount of space available in the power hub cavity. As seen in Figure 5.41, with dimensions of $200 \times 150 \times 140 \text{ mm}^3$ there is plenty of overhead space available for larger batteries to be used in the future, as intended. The power hub has secondary purposes which include the housing of proxy/optical flow sensors, RGB LEDs, and an expandable multiple purpose DB-50 connector. Also inherent in the design is external access to anode and cathode of the LiPo cells connected in parallel. This is an initial attempt to enable the UAV to receive power to a separate device, or to possibly even deliver power to that device.

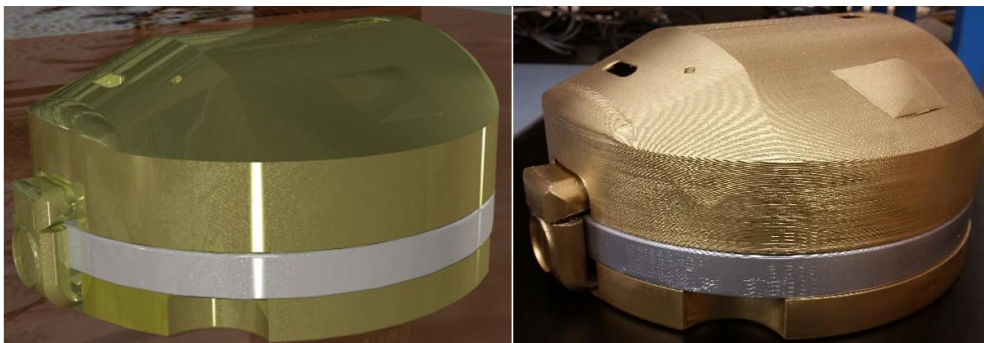


Figure 5.42: Electronics Hub Simulation (left) and photograph (right)

Some immediate necessities derived from difficulties in V1 include improving mass distribution, distancing the UAV from high current wires (for magnetic field), and creating a spacious region for the motherboard. Housing the electronic speed controls in the central hub well underneath the electronics hub resolved the first two goals, while creating a tripple layered electronics hub fulfilled the third. Accessing the motherboard in V1 was also a painstaking task, requiring virtually the entire UAV to be disabled. V2 saw that specific problem remedied by use of a hynge and lock mechanism, greatly improving developmental and troubleshooting speeds.

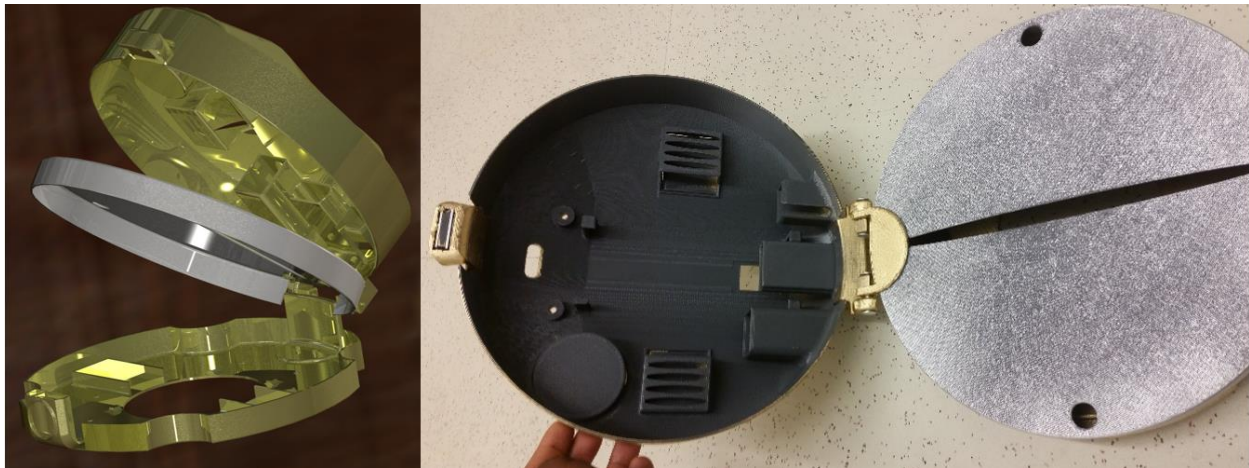


Figure 5.43: Interior of Electronics Hub Simulation (left) and photograph (right)

Instead of a PCB, two small breadboards were placed atop the middle layer of the electronics hub, acting as motherboard for various components and as a bride between compnents placed in the opppermost and lowermost levels of the electronics hub. The desire to push this component to the top layer, furthest from electric fiends in the central hub, was offset by the decreased rigidity of the top layer. Thus the APM flight controler is centrally suspended on the lowest layer of the electrincs hub. The topmost layer was repleat with cavities and extrusions specific to, GPS, communication modules, and the DK-TM4123G development board geometries.



Figure 5.44: UAV Prototype V2 in lab

V2 of our UAV prototype is seen in figure 5.44 above. Despite the use of a carbon fiber frame additional features made it slightly heavier than V1 at just over 10kg. The end to end arm length is 980mm across, with a height of 609mm. Though considerably more complicated, this upgrade was significantly more durable and technological more capable than V1, exceeding initial design criteria. Figure 5.45 below shows the general layout of a field test. The UAV has been moved closer for the sake of photography and would usually safely be several more meters away from everyone at the site. From this distance the aforementioned RF trigger (resembling a car key seen next to the ground station) would safely bring the central MCU out of hibernation and power the device on.



Figure 5.45: General setup for conducting test flights

5.4 Payload Deposit and Acquisition

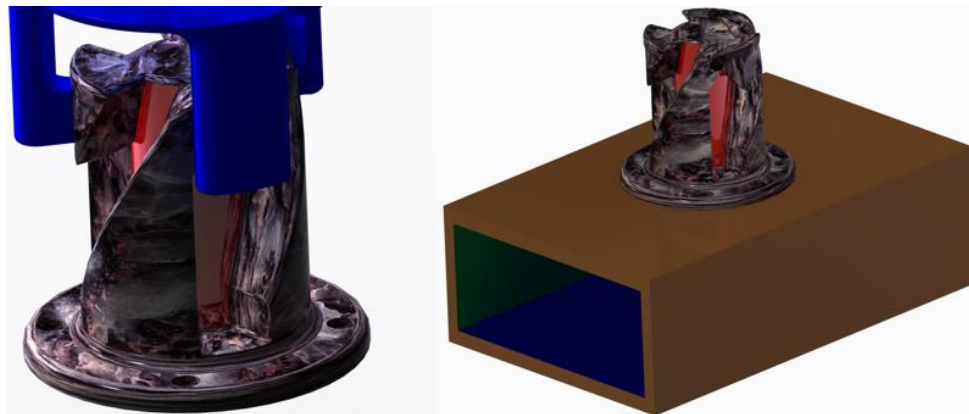


Figure 5.46: V1 payload connectors 3D model

In developing a system for payload deposition and acquisition, the primary design objective was to achieve delivery without the need for an external power sources. Though there we serval (patented) techniques for UAV acquisition and deposition of payloads, all of them were either externally powered or the required the aid of some sort of vision system. A vision system would indeed ease the difficulty, yet the added complexity involved created a yearning for a simpler method. One early morning in January of 2015, after consuming a delicious bottle of Snapple’s all natural apple juice, an idea presented itself. Note that of all possible kinematic motions the UAV can perform, the one performed with the best precision is a yawing action. So why not attach the cap of a bottle of Snapple juice to the bottom of our UAV, fill the bottle with whatever payload we desire (juice or otherwise), and have the UAV twist the cap on to lift the entire bottle away, or twist the cap off to deposit it at any destination? This was the muse for what turned into the payload connector design for V1 seen in Figure 4.46 above.

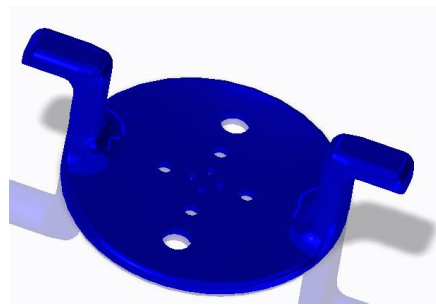


Figure 5.47: V2 Payload connector 3D Model

However, instead of a bottle cap, our UAV would twist itself onto and off of a rectangular lockable payload holding prism. Of course, when using our hands to twist on or twist off a bottle cap, we use one had to keep the bottle steady and the other to revolve the cap (or vice versa). Likewise, a mating platform would be necessary which would lock the rectangular prism in place. The platform would simply need to contain a cavity wide enough to allow the rectangular prism sink into it, yet thin enough to prevent 360 degrees of free rotation about an axis normal to the earth.

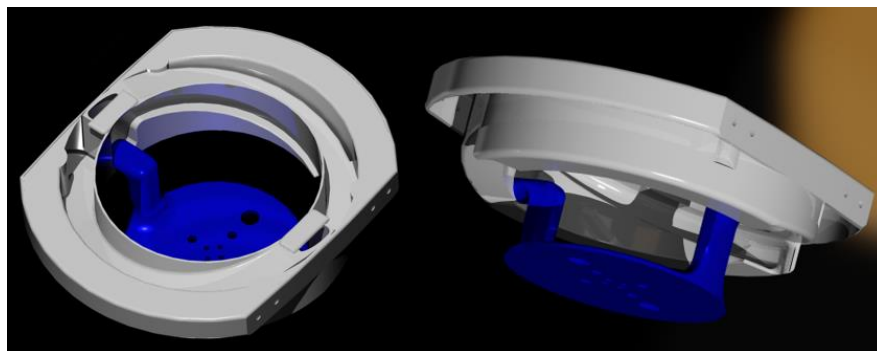


Figure 5.48: 3D model of V2 payload connector within the Payload Hub

In V2, the creation of the power hub provided an avenue for our UAV to power external devices, such as servo motors and scissor lifts. This attribute helped in loosening the strict design criteria of the payload connector set for V1. Though the root concept of twisting the payload on and off

the UAV still remained, the roles were reversed with the twisting action now meant to occur on the ground while the UAV remained stationary. This method has the advantage of being less susceptible to interference (wind), as well as allowing for a more compact payload connector design as seen in figure 5.47 above.

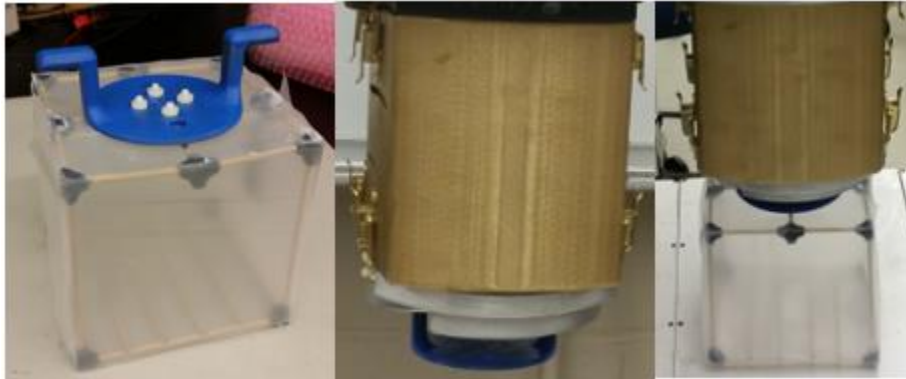


Figure 5.49: Images of the field testing payload compartment connection scheme

5.5 Docking Station

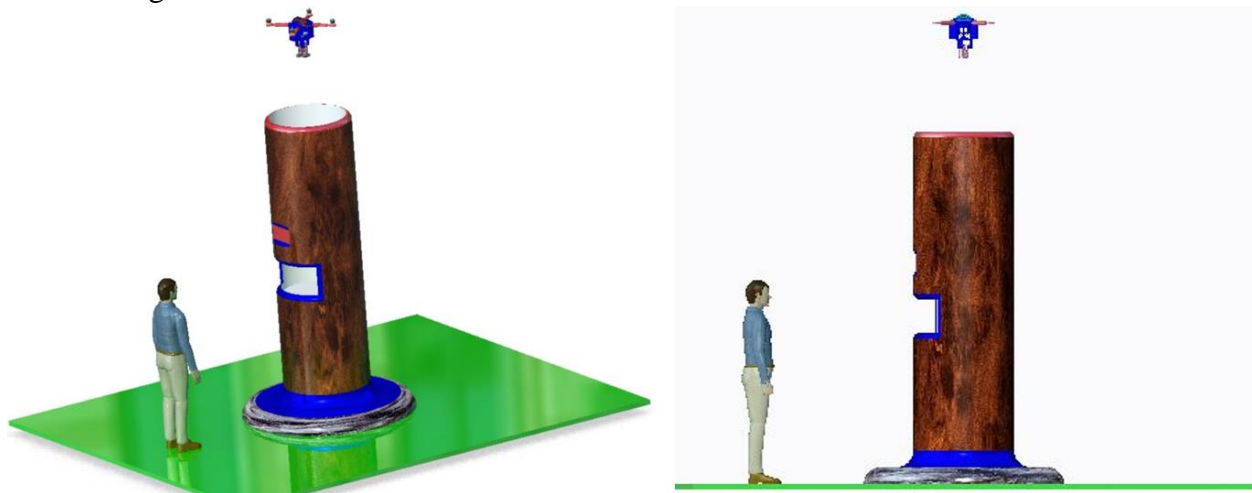


Figure 5.50: Docking Station 3D Model

Time, safety concerns, and financial restrictions arrested the majority of prototyping for the docking station to the virtual realm. Models seen in the Figure 5.59 depict only the beginning of what is certain to be an expansive area of research. Intended to soar 3 meters or more above ground, docking stations can be designed to provide a relief from the ground effects that make landing a risky affair. This is achieved by structuring the docking station with air ducts that redirect thrust forces away from, as oppose to reflecting them towards, the UAV. If V2's payload connection scheme is employed, a rotating platform atop a scissor lift within the docking station can be used to both deposit and acquire packages. End user safety is further enhanced by recognizing that the UAV should never closer than 10 feet to the ground, maintaining a safe vertical distance from the end user. For additional safety, users may be advised to maintain a safe

distance from the docking station during UAV takeoff and landing. To truly grasp the effect of using docking stations, consider a scenario in which a small city of <100,000 residents covering a radius of ~ 5-7 miles is littered with docking stations at every retailer and residential community and public destination. In this scenario, anyone can send or receive goods, making customer returns a possibility. Since every docking station would have a fixed location, UAVs would similarly only land at fixed predetermined locations that can be reviewed ahead of time to ensure security. Lastly, any combination of the docking station being capable of recharging the UAV, or the UAV supplying power to an off-grid docking station (or both), leads to truly limitless possibilities.

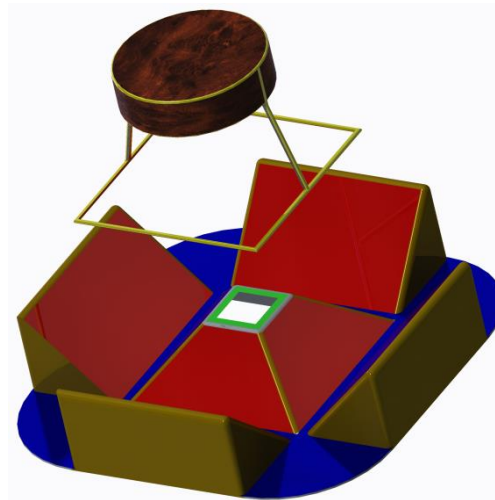


Figure 5.51: Assisted landing concept simulation

An issue surrounding the use of docking stations is the positional accuracy of the UAV while landing. The best GPS will still only provide >3 meters of resolution, so directing the UAV to land at the docking stations specific longitude and latitude will not guarantee a safe landing. Again, we strive for a simple solution powered entirely by the UAV. Figure 5.51 depicts a specific platform design, and a UAV-like object. This is a Creo Mechanism® simulation used to study the auto centering of a UAV. In this simulation, the red surfaces of the platform are given coefficients of kinetic and static friction (μ_k and μ_s) low enough to induce high slippage. Thus, when the UAV is not centered and touches any of the red surfaces while landing, the counter force effectively tilts the UAV, making it no longer normal to the earth. This, in combination with the UAVs flight controller's self-balancing tendencies, leads the UAV to self-center about the platform while landing. Though not enough to compensation for the 3-meter possible overshoot, if used in combination with other tools system (likely a vision system) capable of positioning the UAV within 250-500mm of accuracy, this simulated model will close the gap to achieve precision landing every time.

CHAPTER 6: CHALLENGES, RESULTS, AND ANALYSIS

6.1 Key Challenges

-V1 center of mass



Figure 6.1: Congested cavity for V2

Although many elements of V1's design worked well, a definitive failure was the miscalculation of space required to house all electronics. The 8 ESC's were originally intended to have their heat sinks facing downward towards the external perimeter of the UAV to better dissipate heat, however this was unsuccessful. The rectangular structure of each ESC simply did not join properly with the curvature of the UAV's bottom, despite attempts to accommodate their structure while designing in Creo Parametric. The image to the left shows the resulting disorganized cluster required for there to be any room to attach PCB above. Though completely functional, the randomly distributed heavy ESCs caused a noticeable shift in the UAV's center of mass, which was now biased in the forward direction (front nose). Subsequent test flights would no doubt suffer from this design flaw. Even though the flight controller's self-balancing PI control should make up for the imbalance, an immediate response occurs only in theoretically ideal conditions. The reality is that each test flight

take-off involved a noticeable forward dip down before the KK 2.1's integral errors were large enough to begin compensating. The solution for this problem and many others came in the new design for V2 which made sure to provide ample space for UAV electronics, placed evenly so as to make the center of mass as close to the UAV's geometric center as possible.

-V1 Power Switch

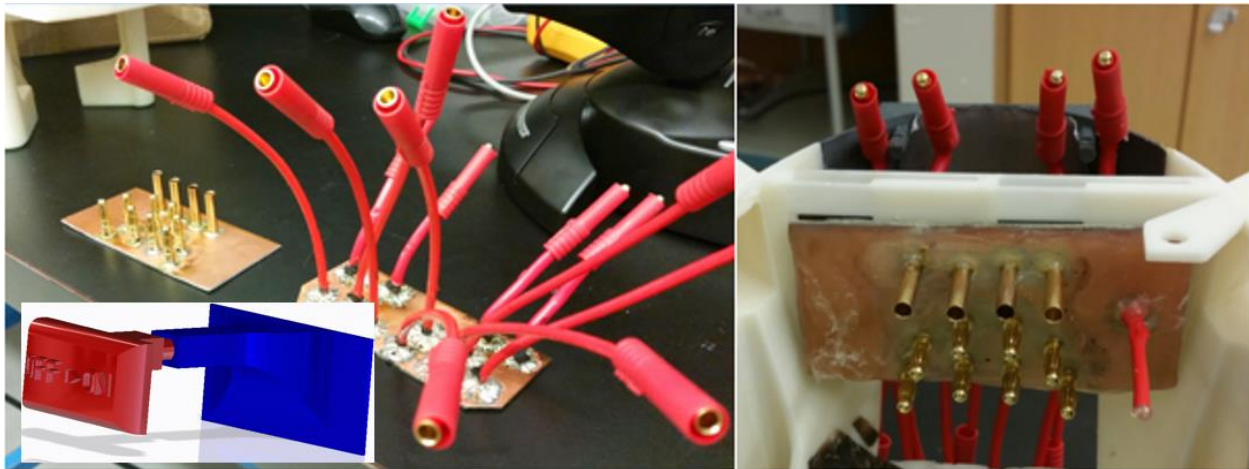


Figure 6.2: Attempt at generating a high current manual switch

While still considering motors that would consume current in the range of 500-800 Amps, the reality of needing a means to connect and disconnect the power supply from UAV electronics

arose. Many switches were available which were rated for such high currents, however each of them would impose a heavy weight tax on our design and often simply wouldn't fit inside the UAV. Eventually, the structure shown in the far-right side of Figure 6.2 was added to the 3D model, and was intended to be a large manual switch. The copper plates each had a thickness of roughly 2.5 mm, so it was estimated that an overlapping layer of 160 square mm might provide enough of a conductive plane to supply the desired current. The doom of this design was in underestimating the amount of friction within the mechanism that held the copper plates in place. This made it tremendously difficult to slide one plate over the other. Until V2, test flights were performed with the power supplying being connected by manually plugging in multiple bullet connectors of 10-gauge wire.

-V1 Motor Mount

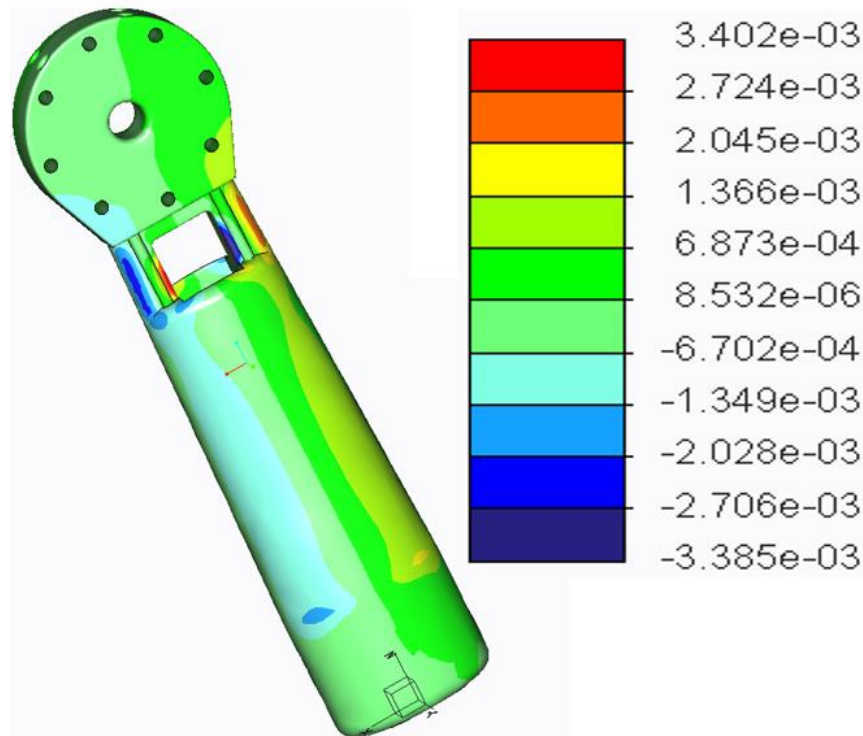


Figure 6.3: Creo 2.0 Simulation showing dynamic displacement (in mm) attributable to load created by motor force on the first version. Maximum displacement was 0.97844 mm

V1 prompted the design of a new motor arm after each test flight, because the motor mount section never failed to break off. Figure 6.3 uses color coding to show the regions of the initial motor arm design that bended the most when motor forces are applied. Not surprisingly, the dark red and dark blue regions on opposing sides indicate twisting in the thinnest section. Subsequent designs worked to better reinforce this region (See appendix), but to no avail. No matter the design, the tip of the motor arm would always need to flatten out in order to mount the dual motors, and this tended to always generate a region exposed to strain under certain forces. Interestingly, the motor arms would always remain intact while the UAV was in flight, but

immediately ruptured after every crash, implying large impulse forces acted on the heavy motors and propellers. As previously mentioned, the ABS Plus plastic was deemed inefficient for handling the required load. Carbon fiber motor arms and aluminum motor mounts implemented in V2 would finally resolve this issue.

-RF Communication

This work introduced a variety of communication problems. SPI and I2C communication protocols proved robust, however, in V1 the singular UART lines of the Stallaris Launchpad made communication with both the XBee RF modules and the Adafruit GPS impossible without additional circuitry. To resolve this issue, the MAX 4518 analog multiplexer was employed. This allowed for transmitted and received lines to be individually selected. The only drawback to this was that the timing algorithm coded into the central MCU was not able to precisely time the GPS receive line's activation, resulting in frequent data loss effectively slowing the update frequency.

V2 saw communication problems of a different nature. Now using two sets of RF modules, operating within the same band, care was taken at the onset to program each onto separate channels. Issues arose mainly while working in the lab, as power levels were often so high, signals would collide or reflect, increasing the error rate. The core communication issue in V2 was in multiplexing the APM's receive line between Missions planner, and the central MCU. This was desired because it would allow the central MCU to send MAV-Commands directly to the APM, exercising even more control over specific functions (such as setting missions). While testing, concerns rose about how to determine an appropriate interval of time to switch received data from Mission Planner to the central MCU without aliasing or losing data. A solution to this problem is still in progress and may involve polling other areas of the APM (voltage levels) that could indicate non-communication periods.

-Power efficiency

A slightly dangerous aspect of V1 was the failed On-Off toggle switch design. This meant that the UAV was always fully powered (though unarmed) immediately after the user connected the positive and negative terminals of the battery to the motherboard. Note that in V2 the motherboard components and ESC's draw a combined total of 700mA even while the UAV is disarmed. Also, since the power supply had to be installed in the lab, 5% battery capacity would typically be lost in commuting from the lab to the testing site. Subsequent elements of our optimized system design required a UAV to remain idle for several days without losing battery capacity.

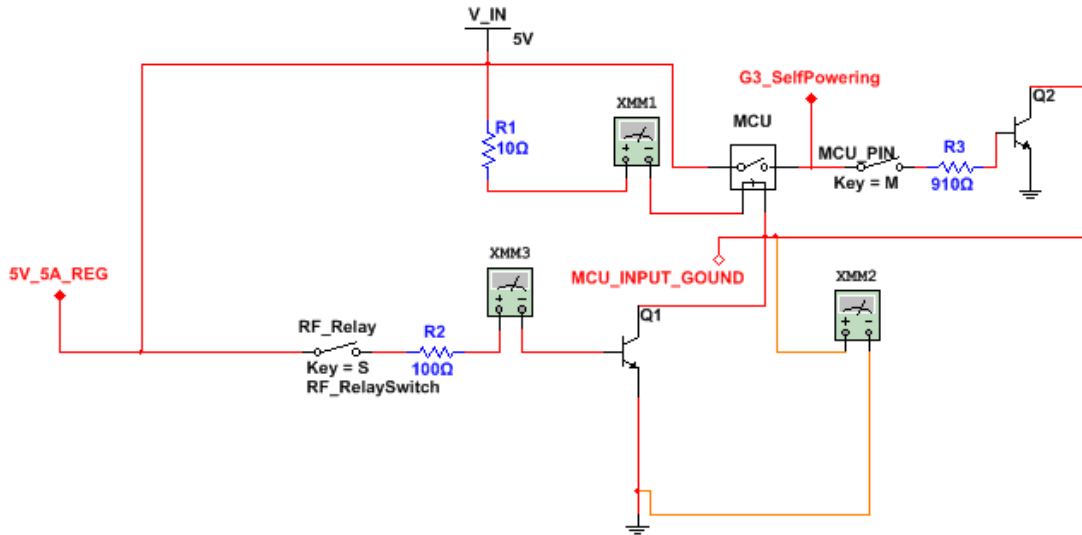


Figure 6.4: MCU powering circuitry

Figure 6.4 shows a portion of the circuitry used to remotely power V2 of our UAV design. Drawing from a suggestion provided by a friend and former colleague Ryan Jensen over some Chinese food, this design allows the motherboard to be semi-powered until the user remotely triggers an RF relay connected to R2 (our modification). The true genius of this design (Ryan's) is found in the G3 pin of the central MCU which acts as a virtual switch allowing the entire system to turn itself off! Not in a virtual sense, but to truly take advantage of the threshold voltages within the bipolar junction transistor (Q2) to physically disconnect it from power until the user activates the RF relay again. Power efficiency is finally maximized by giving the central MCU the ability to toggle power to each major component. With these improvements, we were able to drop idle current from 700mA to <100mA. Assuming a 20Amp-Hour capacity and 30% degradation, this increases docking station idle time from 20 hours to 140 (5.8 days).

6.2 Version 1 Results and Analysis

-Field test day 1

This test was unsuccessful for three reasons. First, the quadcopter design had appeared to not have equivalent center of mass and geometric center. During takeoff, the front blades tilted towards the earth immediately breaking the two front wings. Secondly, the top and bottom set blades were spinning in the wrong direction (an assembly error), causing the UAV to spin uncontrollably. Lastly, the motor arms had a very apparent weakness, breaking in the same location for multiple arms. To fix the balance issues supports were added in the regions marked by red ovals in Figure 6.5. The orientation of the wings was also corrected, along with a new motor arm design.



Figure 6.5: VI Test flight 1

-Field test day 2



Figure 6.6: Sequential images of test flight 2

This second test flight failed due to a combination of improper balance and inadequate proportional gain in the PI controller. As seen in the time-lapse reel of images above, the quadcopter was front heavy, and nosedived upon takeoff. To resolve this issue greater care was taken in placing the ESC's (which caused the misbalance), and weights were added to counter the forward biased center of mass.

-Field test day 3



Figure 6.7: Sequential images of test flight 3

Semi successful, this was the final day of field testing for V1. Though the UAV crashed again, unlike previous attempts, it managed to gain significant altitude. Helping matters was the table which elevated the UAV 1 meter above ground at takeoff, reducing ground effects. Also, the operator raised the throttle very quickly compared to previous attempts, in hopes that this would help the UAV respond quicker to any initial imbalance. Causes for the eventual crash are not as apparent as previous attempts. Care was taken to ensure the best balance, and proper placement of propellers. A most likely cause is improper gain settings for the KK 2.1's proportional and integral controllers. Though the proportional gain was increased (50%) from the default to increase the UAV's responsiveness, there was no means of gauging the effect prior to test flying the UAV. The challenges behind the iterative PID tuning theory highlighted in Chapter 4 came to fruition during practice. Every available guide and even the "auto-leveling" function of the KK 2.1 required the UAV to be able to sustain flight or withstand crashes as an initial condition, this was a key motive for upgrading.

6.3 Version 2 Results and Analysis

-Field test day 1

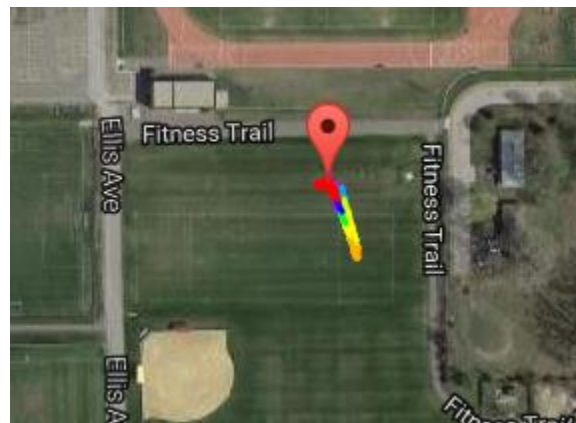


Figure 6.8: Testing ground and flight path of V2

For safety, all field test for V2 were performed on open fields during hours when the pitch was barren. The first field tests for V2 was largely a success, and a long awaited one at that. Among items tested include: manual flight control, autonomous takeoff, autonomous landing, central MSU mode switching, ground station connectivity, and battery level sensing. The string of test flights executed showed an agile UAV, which achieved a velocity of 11 m/s (24.6 miles/hour). An error in the embedded code was revealed when it was noticed that lapses in communication between the ground station and central MCU forced the central MSU to prematurely place the UAV in return to launch mode, creating an awkward oscillation as the UAV would ascend and descend continually for a few seconds. This bug was quickly fixed. The most exciting result from this field test session is shown in Figure 6.9, where we see all the UAV's motions for the first flight achieved at under 65% full power! Meaning there is ample power reserved for carrying a payload. Indeed <45% throttle is required for the UAV to hover.

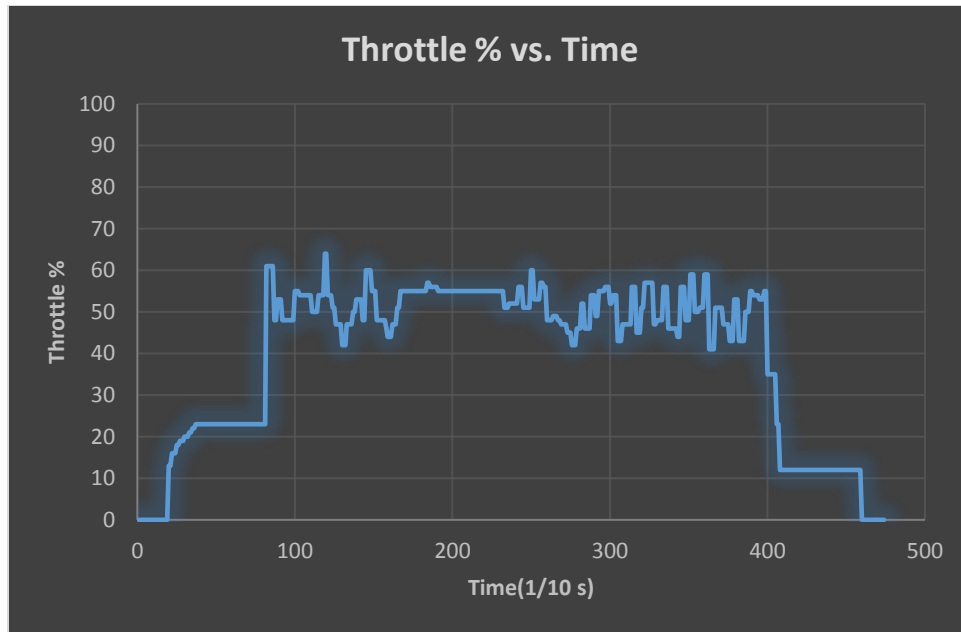


Figure 6.9: V2 first flight, throttle vs. time

*Note: For all V2 charts a combination of varying random processes within the UAVs MCU and random delays in RF communication result in each data point being polled at slightly varying time intervals. Meaning data logging is variant and **not** precisely linear with time. However, this random process is assumed to have a normal Gaussian distribution with constant mean and standard deviation. The data points are each approximately a 10th of a second apart ($\mu = \frac{1}{10}$ seconds), with $\sigma < 50$ milliseconds. Implying that over large time intervals we may treat the time axis as though it were linear.*

The starred region in Figure 6.10 from V2's first field test raises an interesting point. Note that here, the throttle level increase occurs before the spike in ground speed, and is not necessarily maintained during the spike. This makes sense as the only forces acting against horizontal motion are wind and air drag. What this means is that the UAV should be able to achieve high ground speeds by increasing thrust and attaining a certain attitude relative to the ground, but should then be able to maintain that velocity a lowered throttle only needed to counteract wind and drag forces.

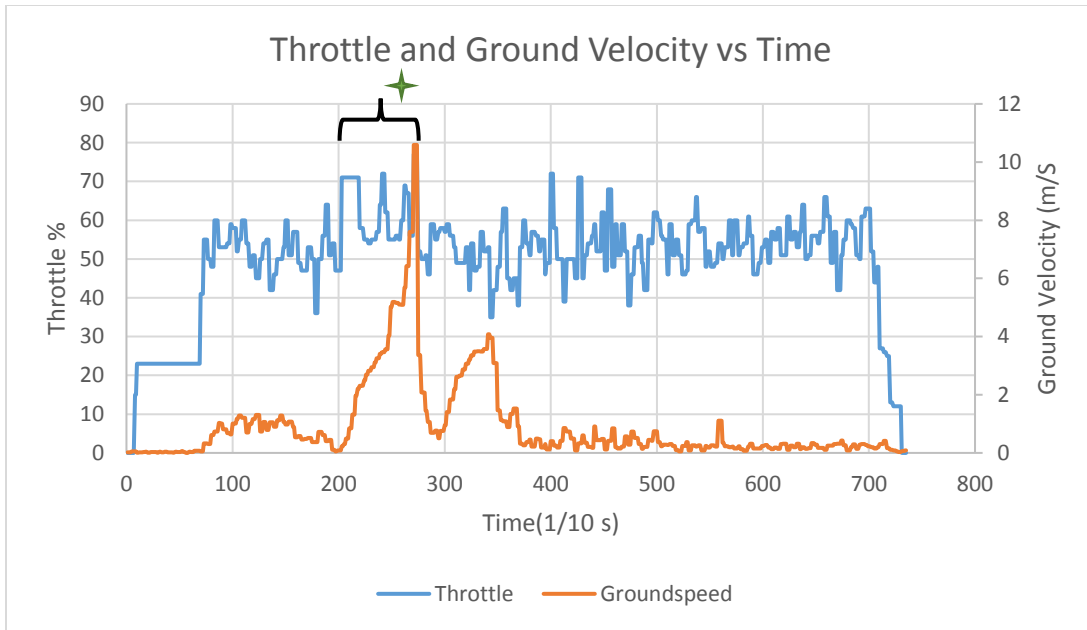


Figure 6.10: V2 Second flight, throttle & ground velocity vs time

-Remaining field tests days (2-6)

All subsequent field tests were geared towards testing flight with different payloads and varying autonomous missions. For safety and legal reasons, the maximum payload, (<8kg/ 17lbs), has to be derived from the remaining available motor thrust (leave 15% throttle for maneuvering). However, the payload hub, payload connector, and payload container were testing inflight and perform appropriately. An initial concern with designing these sections was how well they would hold under more violent motions. To our delight, even test flights involving a crash failed to dislodge the connected payload.

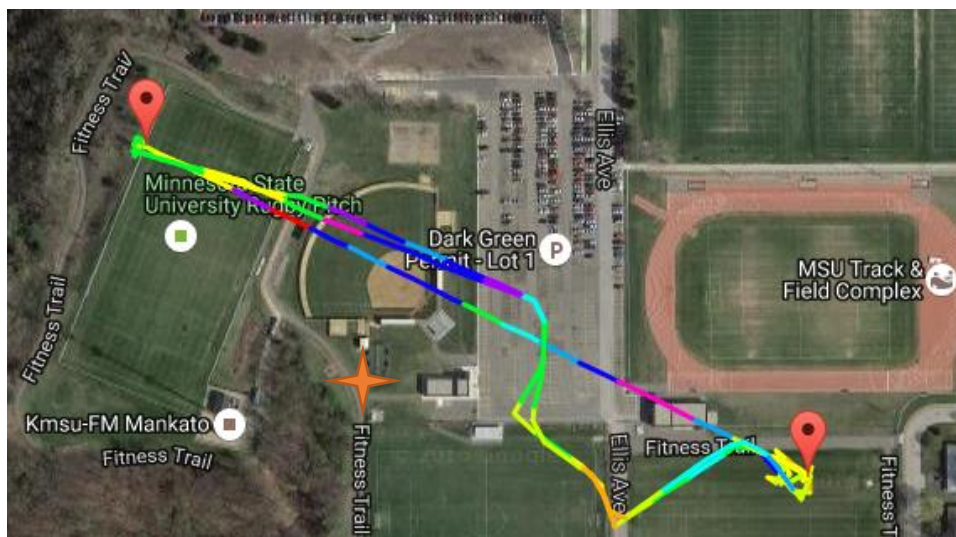


Figure 6.11: V2 Flyaway flight path

V2 field testing generated a single flyaway event early on, caused by a combination of magnets placed within the electronics hub and fling too close to a tower located where the red star is in Figure 6.11 above. As luck would have it, this event generated some of the most useful data acquired in early field testing for V2. The remaining graphs of this chapter are all with reference to this flyaway event.

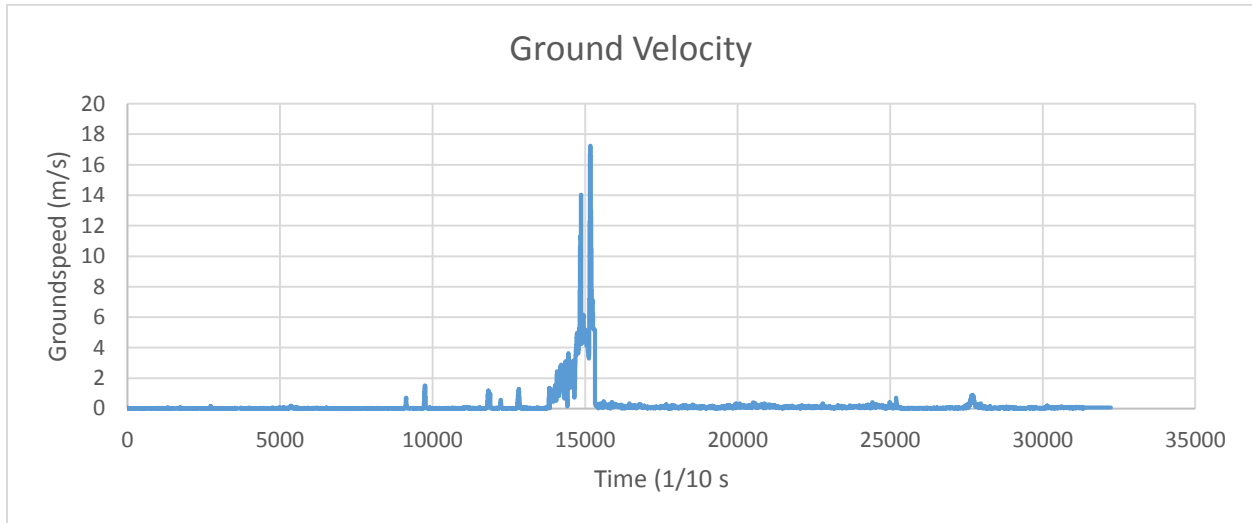


Figure 6.12: V2 Graph of maximum achieved velocity

In all controlled field testing, the UAV was purposely kept within line of sight, and all velocity readings were generally less than 13m/s. The graph above indicates a top speed of 11 m/s (38 miles/hour) during the flyaway event, the fastest velocity achieved yet. Figure 6.13 below shows a sharp climb achieving a vertical velocity of 6 m/s. The sharp spike in vertical velocities implies great acceleration as well. This feat means the UAV can rise to the legal altitude of 400 feet in less than 21 seconds (no payload).

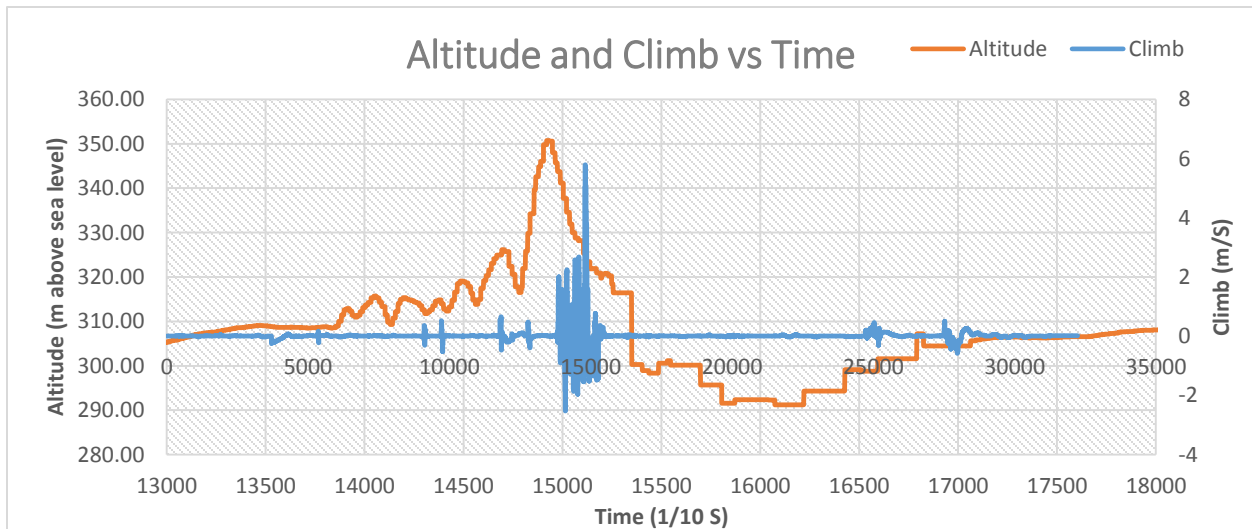


Figure 6.13: V2 Flight 6 Altitude and Climb vs Time

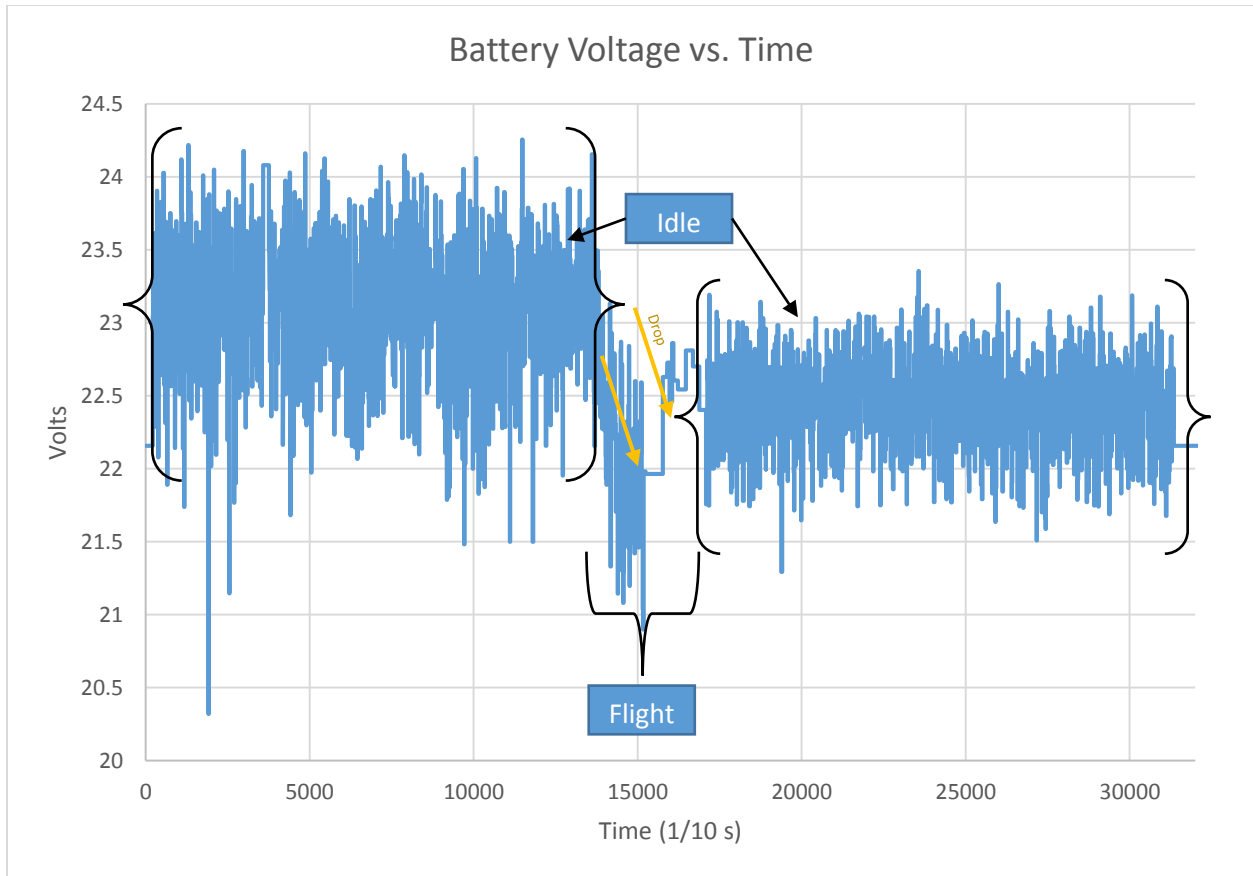


Figure 6.14: V2 battery consumption data

Figure 6.14 serves to verify the tables provided by the T-Motor manufactures, showing current battery capacity dropping represented as a voltage drop. Furthermore, we see the power gating work of the central MCU in action as the idle regions maintain fairly constant voltage while the UAV is grounded. A voltage drop of roughly .6 volts occurs over an ~3-minute flight. In combination with the hovering throttle data obtain from first flight of V2, a 24 Amp-Hour power supply should allow the UAV to hover for a maximum of 24 minutes on its own. Figure 6.15 alludes to the UAVs robustness. Despite heavy magnetic field interferences, the UAV was able to safely land itself (although into trees). Additionally, in Figure 6.16 we see that even as the UAV drifted a quarter mile away from the ground station, RF communication remained. The signal strength was strong at all times, despite the many objects between the UAV and ground station. RSSI only dropped below 100% as the UAV descended below the horizon. As the UAV was completely out of sight long before it landed, this communication link was key to locating it to make repairs and continue further testing.

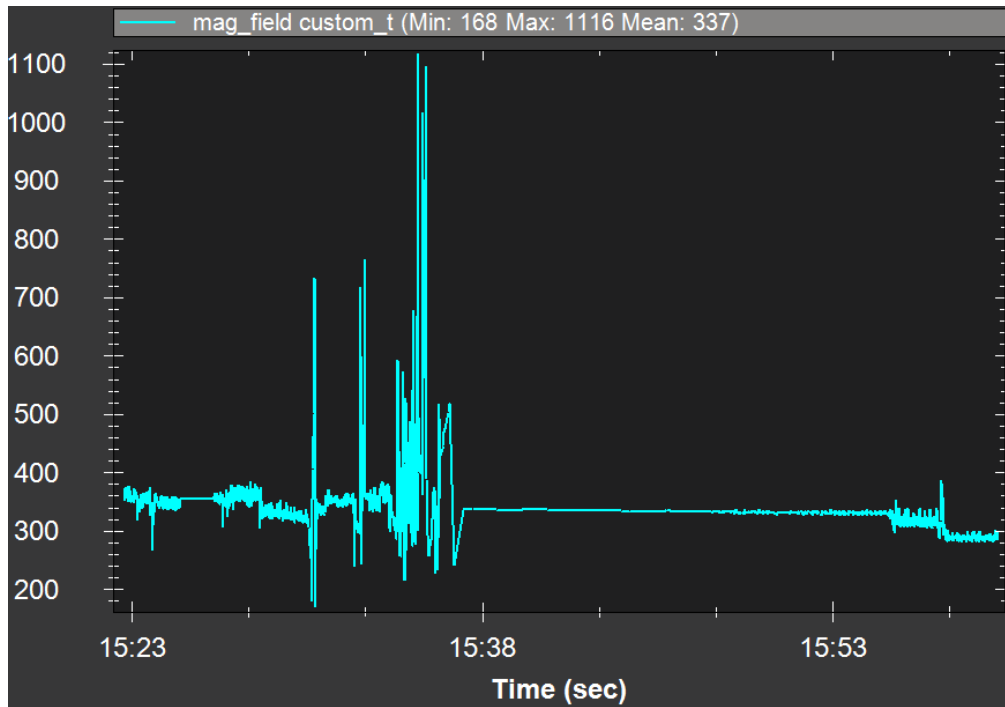


Figure 6.15: V2 Magnet interference (uT) during flyaway

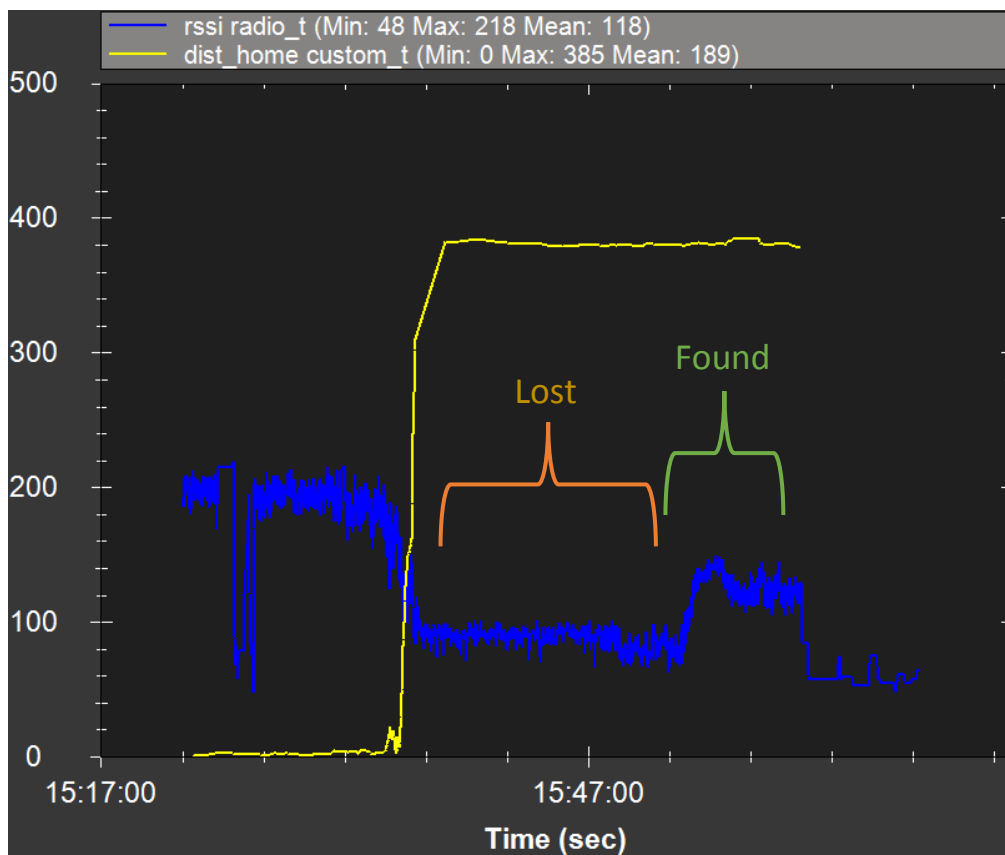


Figure 6.16: V2 Flyaway, distance from ground station (meters) & RSSI vs time

CHAPTER 7: CONCLUSION

7.1 Conclusion

In this thesis, we investigated various options for optimizing delivery via UAV. From a variety of simulations, calculations and field tests, we are able to come to a few conclusions. The development of special light weight yet strong materials such as carbon fiber is integral to improving flight efficiency. Decreasing the mass of the UAV by any means will always see an increase in flight efficiency as they are negatively correlated. The multiple control systems designed in V1 and V2 proved their robustness several times, with lab and field tests showing compensation by one control unit in the event a separate control unit failed. All predicted advantages of an octa-quad design were proven during field testing of V2. This layout not only showed unparalleled stability, but was able to support a 10kg UAV with less than 50% maximum thrust. The velocities achieved in V2, in combination with a versatile payload connector and multiple docking stations, would certainly allow 5-10 mile deliveries of goods <8kg to be achieved within a metropolis faster than the 30-minute benchmark. Strategic placement of docking stations at local retailers and residential communities completes our system design. By doing this, everyday goods can not only be delivered in a safer fashion, but return deliveries would also be optimized.

7.2 Future Work

- Central MCU switching motor failure emergency action
- Addition of Pixycam® vision system to aid in landing procedure
- Addition of Skycat® parachute system
- Continued docking station design and field testing
- Addition of an independent powered standalone failsafe IC
- Replacement of motors with more efficient T-Motor U12 100KV model

CHAPTER 8: BIBLIOGRAPHY

- [1] International Energy Agency, "Market Trends and Medium-Term Prospects," *Energy Efficiency Market Report*, pp. 1-250, 2015.
- [2] L. H. & S. Yirong, "AN APPROACH TOWARDS OVERALL SUPPLY CHAIN," *Elanders Novum*, pp. 1-11, 2002.
- [3] J. Schlinkheider, P. Ramarao, T. Tully, V. Banga and V. Deokar, "Commercial Drones Are Coming Sooner Than," *Insights in Engineering Leadership White Paper*, pp. 2-15, 2014.
- [4] P. Reibisch, "Low-Dimensional Compounds and Composites for Lithium Exchange as well as for Electronic and for Ionic Conductivity Enhancements," pp. 1-30, 2014.
- [5] S. Das, A. Dey, A. Pal and N. Roy, "Applications of Artificial Intelligence in Machine Learning: Review and Prospect," *International Journal of Computer Applications*, vol. 115, pp. 1-11, 2015.
- [6] TEDGlobal, "TED.com," TED, July 2013. [Online]. Available: https://www.ted.com/talks/raffaello_d_andrea_the_astounding_athletic_power_of_quadcopters. [Accessed 2015].
- [7] L. Aerial Power, "Home Page," Aerial Power LTD, 5 9 2016. [Online]. Available: <https://www.aerialpower.com/>. [Accessed 2016].
- [8] A. Clark Estes, "Some Good Things Drones Can (Actually) Do," 03 12 2013. [Online]. Available: <http://gizmodo.com/some-good-things-drones-can-actually-do-1475717696>. [Accessed 2016].
- [9] R. Insight, "Commercial Drones Market To Reach \$4.8 Billion From 2015 To 2021," Radiant Insights, 2015. [Online]. Available: <http://globenewswire.com/news-release/2015/01/12/696475/10115089/en/Commercial-Drones-Market-To-Reach-4-8-Billion-From-2015-To-2021-Radiant-Insights.html>. [Accessed 2015].
- [10] S. Brar, R. Rabbat, V. Raithatha, G. Runcie and A. Yu, "Drones for Deliveries," *Sutardja Center for Entrepreneurship & Technology Technical Report*, pp. 1-21, 2015.
- [11] American Road & Transportation Builders Association, "Frequently Asked Questions," American Road & Transportation Builders Association, 2016. [Online]. Available: <http://www.artba.org/about/faq/>. [Accessed 2016].
- [12] D. Wang, "The Economics of Drone Delivery," 2016. [Online]. Available: <https://www.flexport.com/blog/drone-delivery-economics/>.

- [13] T. Keeny, "How Can Amazon Charge \$1 for Drone Delivery?," ARK INVEST, 5 5 2015. [Online]. Available: <https://ark-invest.com/research/drone-delivery-amazon>.
- [14] Amazon, "United States Patent & Trademark Office Patent Application Full Text and Image Database," Amazon Technologies, 30 4 2015. [Online]. Available: http://appft.uspto.gov/netacgi/nph-Parser?Sect1=PTO1&Sect2=HITOFF&d=PG01&p=1&u=%2Fnethtml%2FPTO%2Fsrc_hnum.html&r=1&f=G&l=50&s1=%2220150120094%22.PGNR.&OS=DN/20150120094&RS=DN/20150120094. [Accessed 2016].
- [15] N. Layne, "Exclusive: Wal-Mart seeks to test drones for home delivery, pickup," Reuters, 2015. [Online]. Available: http://www.reuters.com/article/us-wal-mart-stores-drones-exclusive-idUSKCN0SK2IQ20151026?feedType=RSS&feedName=topNews&utm_source=twitter. [Accessed 2016].
- [16] CNN, "Drone maker says it's 'highly unlikely' White House drone malfunctioned," CNN, 30 1 2015. [Online]. Available: <http://www.cnn.com/2015/01/30/politics/drone-malfunction-creators-says-highly-unlikely/>. [Accessed 2016].
- [17] T. C. Sottek, "Walmart is testing drone delivery," The Verge, 26 10 2015. [Online]. Available: <http://www.theverge.com/2015/10/26/9617600/walmart-drones-amazon-faa-test>. [Accessed 2016].
- [18] Department of Transportation: Federal Aviation Administration, "Operation and Certification of Small Unmanned Aircraft Systems Final Rule," *Federal Register*, vol. 81, no. 124, pp. 1-152, 28 6 2016.
- [19] N. Levy and T. Bishop, "FAA issues final commercial drone rules, restricting flights in setback for Amazon's delivery ambitions," GeekWire, 21 June 2016. [Online]. Available: <http://www.geekwire.com/2016/faa-issues-final-commercial-drone-rules-restricting-flights-setback-amazons-delivery-ambitions/>.
- [20] S. N. Ghazbi, Y. Aghli, M. Alimonhamadi and A. A. Akbari, "Quadrotors unmanned aerial Vehicles: A Review," *INTERNATIONAL JOURNAL ON SMART SENSING AND INTELLIGENT SYSTEMS*, vol. 9, no. 1, pp. 1-25, 2016.
- [21] Draganflyer Company, [Online]. Available: <http://www.draganfly.com>. [Accessed 01 September 2015].
- [22] I. Kroo, F. Prinze, M. Shantz and P. Kunz, "The Mesicopter: A Miniature Rotorcraft Concept–Phase Ii Interim Report," *Stanford university, Technical report*, 2000.

- [23] N. Nigam, S. Bieniawski, I. Kroo and J. Vian, "Control Of Multiple Uavs For Persistent Surveillance: Algorithm And Flight Test Results," *IEEE Transactions on Control Systems Technology*, vol. 20, p. 12361251, 2012.
- [24] P. Pounds and R. Mahony, "Design of A Four-Rotor Aerial Robot," in *Australasian Conference on Robotics & Automation*, Auckland, New Zealand, 2002.
- [25] R. Naldi, P. Pounds, S. De Marco and L. Marconi, "Output Tracking For Quadrotor-Based Aerial Manipulators," in *American Control Conference (ACC)*, Chicago, IL, 2015.
- [26] J. D. Plessis and P. I. Pounds, "Rotor Flapping for a Triangular Quadrotor," in *Australasian Conference on Robotics and Automation*, University of Melbourne, Melbourne, Australia, 2014.
- [27] E. Altug, J. P. Ostrowski and R. Mahony, "Control Of A Quadrotor Helicopter Using Visual Feedback," in *Proceedings. IEEE International Conference on Robotics and Automation*, 2002.
- [28] M. Tarhan and E. Altug, "EKF Based Attitude Estimation and Stabilization of a Quadrotor UAV Using Vanishing Points in Catadioptric Images," *Journal of Intelligent & Robotic Systems*, vol. 62, p. 587607, 2011.
- [29] B. Erginer and E. Altug, "Design And Implementation Of A Hybrid Fuzzy Logic Controller For A Quadrotor VTOL Vehicle," *International Journal of Control, Automation and Systems*, vol. 10, pp. 61-70, 2012.
- [30] P. Castillo, A. Dzul and R. Lozano, ""Real-Time Stabilization And Tracking Of A Four-Rotor Mini Rotorcraft," *IEEE Transactions on Control Systems Technology*, vol. 12, pp. 510-516, 2004.
- [31] R. Sanz, P. Garcia, P. Castillo and P. Albertos, "Time-Delay Compensation Using Inertial Measurement Sensors For Quadrotor Control Systems," in *17th International Conference on Information Fusion (FUSION)*, Salamanca, 2014.
- [32] J. Carino, H. Abaunza and P. Castillo, "Quadrotor Quaternion Control," in *International Conference on Unmanned Aircraft Systems (ICUAS)*, Denver, CO, 2015.
- [33] L. R. Garcia Carrillo, I. Fontoni, E. Rondon and A. Dzul, "Three-Dimensional Position And Velocity Regulation Of A Quad-Rotorcraft Using Optical Flow," *IEEE Transactions on Aerospace and Electronic Systems*, vol. 51, pp. 358-371, 2015.
- [34] M. Bisgaard, "Modelling And Fault-Tolerant Control Of An Autonomous Wheeled Robot," 2004.
- [35] G. Hoffmann, D. Rajnarayan, S. L. Waslander, D. Dostal, J. Jung Soon and C. J. Tomlin, "The Stanford Testbed Of Autonomous Rotorcraft For Multi Agent Control

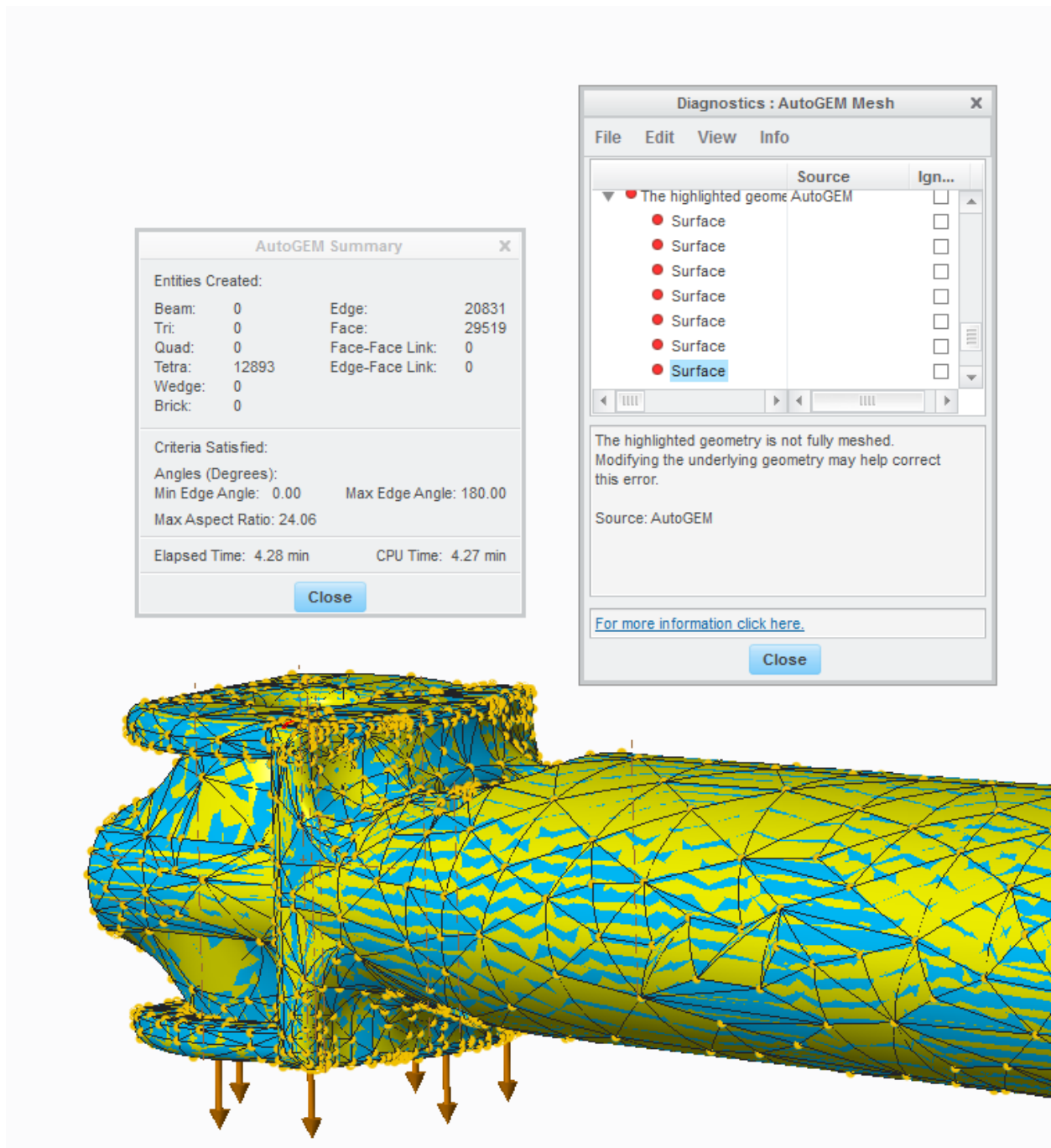
- (STARMAC)," in *23rd Digital Avionics Systems Conference (DASC'04)*, Salt Lake City, USA, 2004.
- [36] J. H. Gillula, G. M. Hoffmann, H. Huang, M. P. Vitus and C. Tomlin, "Applications Of Hybrid Reachability Analysis To Robotic Aerial Vehicles," *International Journal of Robotics Research*, pp. 335-354, 2011.
- [37] S. Bouabdallah, P. Murrieri and R. Siegwart, "Design And Control Of An Indoor Micro Quadrotor," in *International Conference on Robotics and Automation (ICRA'04)*, New Orleans, USA, April 26- May 01, 2004.
- [38] M. D. Hua, G. Ducard and S. Bouabdallah, "A Robust Attitude Controller And Its Application To Quadrotor Helicopters," in *18th IFAC World Congress, International Federation of Automatic Control*, 2011.
- [39] E. Brian Nice, "Design of a Four Rotor Hovering Vehicle," *Masters Thesis: Faculty of the Graduate School Cornell University*, 2004.
- [40] K. Rudin, M. D. Hua, G. Ducard and S. Bouabdallah, "A Robust Attitude Controller And Its Application To Quadrotor Helicopters," in *Proceedings of the 18th IFAC World Congress*, Università Cattolica del Sacro Cuore, Milano, Italy, 2011.
- [41] F. B. ÇAmlica, "Demonstration Of A Stabilized Hovering Platform For Undergraduate Laboratory," Masters Thesis, School of natural and applied science, Middle east Technical University, 2004.
- [42] W. Kong Wai and M. S. B. Abidin, "Design and Control of a Quad-Rotor Flying Robot For Aerial Surveillance," in *4th Student Conference on Research and Development, SCORED*, Selangor, 2006.
- [43] M. Kemper, "Impact Of Center Of Gravity In Quadrotor Helicopter Controller Design," in *4th IFAC Symposium on Mechatronic Systems*, Ruprecht-Karls-University, Germany, 2006.
- [44] E. Kemper, "Quad-Rotor Flight Path Energy Optimization," Masters Thesis, Northern Arizona University, 2004.
- [45] T. Puls, M. Kemper, R. Kuke and A. Hein, "GPS-Based Position Control And Waypoint Navigation System For Quadrocopters," in *IEEE/RSJ International Conference on Intelligent Robots and Systems*, St. Louis, MO, 2009.
- [46] I. Whidborne and A. K. Cooke, "Optimal Trajectory Planning And LQR Control For A Quadrotor UAV," in *International Conference Control*, Glasgow, Scotland, 2006.

- [47] I. Cowling, O. Yakimenko, J. Whidborne and A. Cooke, "Direct Method Based Control System for an Autonomous Quadrotor," 2010.
- [48] T. Glenn, V. Mario, H. Jonathan and F. Eric, "Estimation and Control of a Quadrotor Vehicle Using Monocular Vision and Moiré Patterns," in *AIAA Guidance, Navigation, and Control Conference and Exhibit*, ed: American Institute of Aeronautics and Astronautics, Keysteone, Colorado, 2006.
- [49] B. Michini, T. Walsh, A. A. Agha-Mohammadi and J. P. How, "Bayesian Nonparametric Reward Learning From Demonstration," *IEEE Transactions on Robotics*, vol. 31, no. 2, pp. 369-386, 2015.
- [50] M. Cutler and J. P. How, "Analysis and Control of a Variable-Pitch Quadrotor for Agile Flight," *Journal of Dynamic Systems, Measurement, and Control*, vol. 137, pp. 101002-101003, 2015.
- [51] M. Wierema, "Design, implementation and flight test of indoor navigation and control system for a quadrotor UAV," 21-30 2006.
- [52] B. C. N. Carlos, J. Cook, J. Forest, S. Johnson, E. Massie and C. Rogers, "Technical Report Of IARC Team Quadrotor," Virginia Tech University, 2008-2009.
- [53] J. Conroy, G. Gremillion, B. Ranganathan and J. S. Humbert, "Erratum To: Implementation Of Wide-Field Integration Of Optic Flow For Autonomous Quadrotor Navigation," *Autonomous Robots*, vol. 27, pp. 199-200, 2009.
- [54] J. Keshavan, G. Gremillion, H. Alvarez-Escobar and J. S. Humbert, "Autonomous Vision-Based Navigation of a Quadrotor in Corridor-Like Environments," *International Journal of Micro Air Vehicles*, vol. 7, pp. 111-124, 2015.
- [55] F. J. Harandi and A. M. S. V. Khorani, "Modeling, Simulation and Implementation of a Quadrotor," in *RoboCup Iran Open 2010 Symposium*, Tehran Iran, April 07- April 09, 2010.
- [56] S. D. Hanford, L. N. Long and J. F. Horn, "A Small Semi-Autonomous Rotary-Wing Unmanned Air Vehicle (UAV)," *AIAA SciTech, AIAA infotech at aerospace*, vol. 7077, 2005.
- [57] Silverlit company, [Online]. Available: <http://www.silverlit-flyingclub.com/xufo.htm>. [Accessed 08 February 2015].
- [58] Microdrones Company, [Online]. Available: <http://www.microdrones.com>. [Accessed 5 October 2016].

- [59] P. Mckerrow, "Modelling the draganflyer four-rotor helicopter," *Proceedings of the 2004 IEEE International Conference on Robotics & Automation*, 2004.
- [60] G. M. Hoffmann, H. Huang, S. L. Waslander and C. J. Tomlin, "Quadrotor helicopter flight dynamics and control theory and experiment," 2007.
- [61] P. Pounds, R. Mahony and P. Corke, "Modelling and control of a," *Proceedings of the Australasian Conference on Robotics and Automation*, pp. 1-30, 2006.
- [62] J. Mulder, "Flight dynamics - Lecture Notes," Technical Report, TU Delft, 2006.
- [63] R. Prouty, *Helicopter Performance, Stability and Control*, Reprint with additions, iriginal edition 1986 ed., Krieger Publishing, 2002.
- [64] D. Hartman, K. Landis, M. Mehrer, S. Moreno, J. Kim and D. B. C. Chang, "Quadcopter Dynamic Modeling and Simulation (Quad-Sim) v1.00," GitHub Inc., 2014.
- [65] F. G. Martins, "Tuning PID Controllers using the ITAE Criterion*," *Int. J Engng*, vol. 21, no. 5, pp. 867-873, 2005.
- [66] S. Thus, P. Boon, N. Diepeveen, A. Helderweirt, B. Kuiper, E. Moerland, R. Scherders and R. Van Stavern, "The Insight - Design Synthesis," *Technical Report, TU Delft*, 2007.
- [67] G. Ning, S. B. Haran and N. B. Popov, "Study on the Effects of Discharge Rates on the Capacity Fade of Lithium-ion Battery," University of South Carolina, Columbia, SC.
- [68] ArduPilot Development Team, "ArduPilot Autopilot Suite," 1 August 2016. [Online]. Available: <http://ardupilot.org/copter/index.html>.
- [69] G. Fay, "Derivation of the aerodynamic forces for the mesicopter simulation.," *EPFL*, 2001.
- [70] Y. Cao, "Learning PID Tuning III: Performance Index Optimization," *MATLAB Central*, 2008.
- [71] Toglefritz, "The Physics of Quadcopter Flight," Black Tie Aerial, 29 4 2014. [Online]. Available: <http://blacktieaerial.com/the-physics-of-quadcopter-flight/>. [Accessed 2016].
- [72] Ascending Technologies Company, [Online]. Available: <http://www.asctec.de/uav-applications/research/products/asctec-hummingbird/>. [Accessed 08 February 2015].
- [73] N. Carlos, B. Cole, J. Cook, J. Forest, S. Johnson, E. Massie and C. Rogers, "IARC Team Quadrotor," Virginia Tech, Blacksburg, Virginia, 2010.
- [74] Electropaedia, "Battery Performance Characteristics," [Online]. Available: <http://www.mpoweruk.com/performance.htm>.

[75] rightbattery.com, "Nano-Tech," [Online]. Available: <http://rightbattery.com/tag/nano-tech/>. [Accessed 20 October 2016].

CHAPTER 9: APPENDICES



(V1 2nd motor arm design simulation challenges)

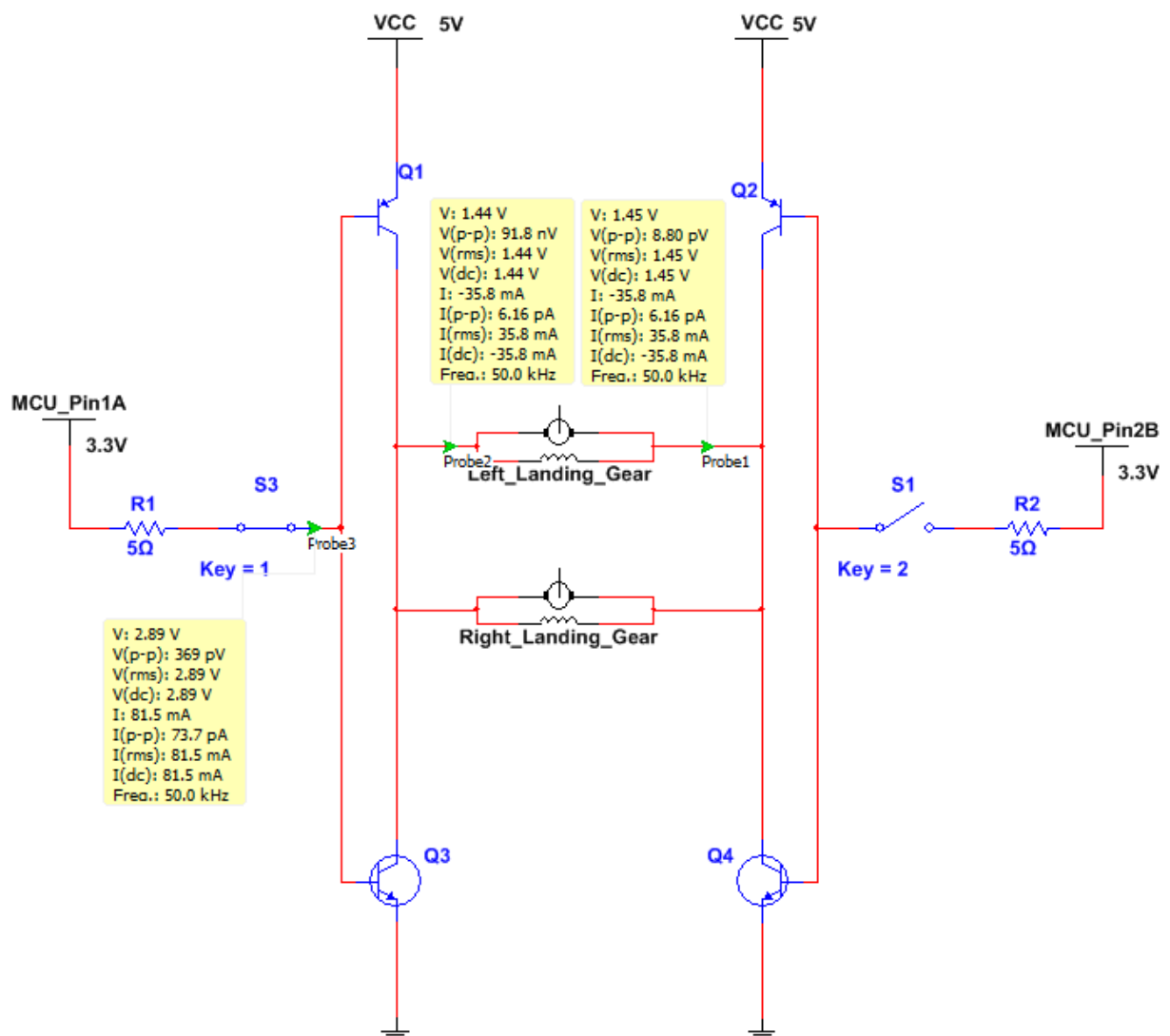
```

function Derivatives(block)
% Name all the states and motor inputs % Load model data selected in parameter block
%which('model')
quad = block.DialogPrm(1).Data;
% P Q R in units of rad/sec
P = block.ContStates.Data(1);
Q = block.ContStates.Data(2);
R = block.ContStates.Data(3);
% Phi The Psi in radians
Phi = block.ContStates.Data(4);
The = block.ContStates.Data(5);
Psi = block.ContStates.Data(6);
% U V W in units of m/s
U = block.ContStates.Data(7);
V = block.ContStates.Data(8);
W = block.ContStates.Data(9);
% X Y Z in units of m
X = block.ContStates.Data(10);
Y = block.ContStates.Data(11);
Z = block.ContStates.Data(12);
% w values in rev/min! NOT radians/s!!!
w1 = block.InputPort(1).Data;
w2 = block.InputPort(2).Data;
w3 = block.InputPort(3).Data;
w4 = block.InputPort(4).Data;
w = [w1; w2; w3; w4];
%-----
Dist_tau = block.InputPort(5).Data(1:3);
Dist_F = block.InputPort(5).Data(4:6);
%-----
% CALCULATE MOMENT AND THRUST FORCES
% Total Moment due to motor speeds
% Moment should be in units of N*m
% The experimental determination of Ct and Cq should be adjusted to
% model using kg instead of ounces or lb
Mb = (quad.dctcq*(w.^2)) + (Dist_tau); % (dctcq*(w.^2)); % Mb = [tau1 tau2 tau3]'
tau_motorGyro = [Q*quad.Jm*2*pi/60*(-w1-w3+w2+w4); P*quad.Jm*2*pi/60*(w1+w3-w2-w4)];
0];
% Note: 2*pi/60 required to convert from RPM to radians/s
Mb = (quad.dctcq*(w.^2))+ tau_motorGyro + (Dist_tau); % Mb = [tau1 tau2 tau3]'
% Thrust due to motor speed
% Force should be in units of Newtons for simplicity in calculating
% the acceleration in the angular velocity state equation
Fb = [0; 0; sum(quad.ct*(w.^2))]; % [0, 0, sum(ct*w.^2)]'
% Obtain dP dQ dR
omb_bi = [P; Q; R];
OMB_bi = [ 0, -R, Q;
          R, 0, -P;
          -Q, P, 0];
b_omdotb_bi = quad.Jbinv*(Mb-OMB_bi*quad.Jb*omb_bi);
H_Phi = [1, tan(The)*sin(Phi), tan(The)*cos(Phi);
         0, cos(Phi), -sin(Phi);
         0, sin(Phi)/cos(The), cos(Phi)/cos(The)];
Phidot = H_Phi*omb_bi;
% Compute Rotation Matrix
% We use a Z-Y-X rotation
Rib = [cos(Psi)*cos(The) cos(Psi)*sin(The)*sin(Phi)-sin(Psi)*cos(Phi)
       cos(Psi)*sin(The)*cos(Phi)+sin(Psi)*sin(Phi)
       sin(Psi)*cos(The) sin(Psi)*sin(The)*sin(Phi)+cos(Psi)*cos(Phi)
       sin(Psi)*sin(The)*cos(Phi)-cos(Psi)*sin(Phi);
       -sin(The) cos(The)*sin(Phi)
       cos(The)*cos(Phi)];
Rbi = Rib';
ge = [0; 0; -quad.g];
gb = Rbi*ge;
Dist_Fb = Rbi*Dist_F;
% Compute Velocity and Position derivatives of body frame
vb = [U;V;W];
b_dv = (1/quad.mass)*Fb+gb+Dist_Fb-OMB_bi*vb; % Acceleration in body frame (FOR
VELOCITY)
i_dp = Rib*vb; % Units OK SI: Velocity of body frame w.r.t inertia frame (FOR
POSITION)
dP = b_omdotb_bi(1);
dQ = b_omdotb_bi(2);
dR = b_omdotb_bi(3);
dPhi = Phidot(1);
dTheta = Phidot(2);
dPsi = Phidot(3);
dU = b_dv(1);
dV = b_dv(2);
dW = b_dv(3);
dX = i_dp(1);
dY = i_dp(2);
dZ = i_dp(3);
% Rough rule to impose a "ground" boundary...could easily be improved...
if ((Z<=0) && (dZ<=0)) % better version then before?
    dZ = 0;
    block.ContStates.Data(12) = 0;
end
f = [dP dQ dR dPhi dTheta dPsi dU dV dW dX dY dZ]';

```

Quadcopter
dynamics
block main
code for
state space
simulation
[64]

H-Bridge Control Motor Circuit



Input A	Input B	Output A	Output B	Motor Direction
0	0	1	1	Stopped (braking)
0	1	1	0	Clockwise
1	0	0	1	Counter-clockwise
1	1	0	0	Stopped (braking)

